Copyright
by
Jane Lillian Pratt
2009

The Dissertation Committee for Jane Lillian Pratt
certifies that this is the approved version of the following dissertation:

Drift Wave Stability and Transport in Tandem Mirrors

Committee:

Wendell Horton, Supervisor

H.L. Berk

Richard Hazeltine

Sonia Paban

Gary Hallock

Drift Wave Stability and Transport in Tandem Mirrors

by

Jane Lillian Pratt, B.S.; M.A.

DISSERTATION
Presented to the Faculty of the Graduate School of
The University of Texas at Austin
in Partial Fulfillment
of the Requirements
for the Degree of

DOCTOR OF PHILOSOPHY

THE UNIVERSITY OF TEXAS AT AUSTIN
May 2009

Dedicated to my parents, Lawrence and Kathleen Pratt, who have unfailingly helped and supported me while I have sought out a life of the mind.

Acknowledgments

I wish to thank primarily my parents, Lawrence and Kathleen Pratt, for helping me every step of the way. I would also like to thank the many friends and teachers that have passed through my life and made it richer during my student career.

Both Wendell Horton and Herb Berk were instrumental in discussing physics with me throughout my graduate years at the University of Texas. Their support and guidance was invaluable. I hope that we collaborate for many more years.

In regards to my study of plasma physics, I can think of no more apt quotation than that of the great jazz-man Fats Waller "It must be jelly, 'cause jam don't shake like that!"

Drift Wave Stability and Transport in Tandem Mirrors

Publication No. ____________________

Jane Lillian Pratt, Ph.D.
The University of Texas at Austin, 2009

Supervisor: Wendell Horton

In recent years experimental advances at the GAMMA-10 facility in Tsukuba, Japan have shown that tandem mirrors should remain an important subject for theoretical study. The absence of toroidal curvature and relatively weak internal plasma parallel currents in a tandem mirror gives the mirror system strongly favorable stability and transport properties compared with toroidal systems. GAMMA-10 experiments (T. Cho *et al* PRL (97), 2006) demonstrate that sheared plasma rotation suppresses turbulent radial losses by controlling radial potential profiles. Achievements of the GAMMA-10 include 2.5 keV ion confining potentials and electron temperatures approaching 1 keV (T. Cho, Private correspondence, Dec 24th, 2006). Total energy confinement times for the GAMMA-10 experiment are significantly larger than corresponding empirical confinement times in toroidal devices. At the temperatures currently achieved in the GAMMA-10, the end loss rate $\tau_{||} \simeq 100$ ms so that radial losses determine the energy confinement time τ_{E}, as intended in tandem mirror reactor designs (R. F. Post, T.K. Fowler, *et al.*, Fusion Science and Technology, (47), 2005). The most current measurements of τ_{E} are on the order of 72 ms. Tandem mirrors exhibit a qualitatively different type of drift wave transport than do toroidal devices, as we have shown by developing confinement time scaling predictions (J. Pratt and W. Horton, Phys. Plasmas (13), 2006. W. Horton, J. Pratt, H.L. Berk, M. Hirata. Proceedings of the Open Magnetic Systems For Plasma Confinement Conference. Tsukuba, Japan, July 17-21, 2006). These predictions use a variety of standard transport models, e.g., Bohm, gyro-Bohm, and electron-temperature gradient models. We analyze electrostatic drift wave eigenmodes for the electrostatic potential and the magnetic perturbation in the GAMMA-10. We use teraFLOPS speed, large scale parallel computers to integrate the orbits in models of the drift wave losses in the GAMMA-10. We extrapolate these results to reactor designs for the kinetically stabilized tandem mirror reactor proposed by Post *et al,* and discuss implications for its stability, transport, and performance.

Table of Contents

Acknowledgments **v**

Abstract **vi**

List of Figures **xi**

List of Tables **xvi**

Chapter 1. Principles of Tandem Mirrors **1**

- 1.1 The Mirror Trap 3
- 1.2 The Problem of End-Losses 5
- 1.3 The Ambipolar Trap 5
  - 1.3.1 Thermal Barriers 7
- 1.4 General Properties of Tandem Mirrors 10
- 1.5 Minimum-B Stability 13
- 1.6 The GAMMA-10 Experiment 14
  - 1.6.1 Particle orbits in the GAMMA-10 18
- 1.7 The Kinetically Stabilized Tandem Mirror 19
- 1.8 Motivation 23

Chapter 2. Confinement Time Scaling Laws **25**

- 2.1 Derivation of Tandem Mirror Radial Energy-Confinement Times 26
  - 2.1.1 Adaption of Toroidal Database Scaling Laws to Tandem Mirror Geometry 30
- 2.2 Summary 32

Chapter 3. Basics of Tandem Mirror Geometry and Stability 35
3.1 The Flux Coordinate Metric and Tandem Mirror Formalism . 36
    3.1.1 The Gradient in Flux-Coordinates 45
3.2 Derivation of Normal and Geodesic Curvatures 46
3.3 Summary 53

Chapter 4. Ideal MHD Eigenmode Theory 54
4.1 Derivation of the Ballooning mode equation 55
4.2 Axisymmetric Ballooning mode equation from Kaiser and Pearlstein 60
4.3 Normal mode equation for the mth Azimuthal Eigenmode . . . 61
4.4 Axisymmetric Ballooning Mode Equation 62
4.5 Kinetic theory models of MHD Modes 65
4.6 Analysis of Eigenmodes in Tandem Mirrors 68
4.7 MHD Stability 69
4.8 Summary 70

Chapter 5. Spectral Gaps in Tandem Mirrors 71
5.1 Tandem mirror formulation of the Spectral Gap Problem . . . 72
5.2 Spectral Gap Results 74
    5.2.1 GAMMA-10 Tandem Mirror predictions 81
5.3 Summary 83

Chapter 6. Trapped Particle Modes 84
6.1 Simple Model of the KSTM 87
    6.1.1 The Kinetic Stabilizer Beam 90
    6.1.2 Pressure in the kinetic stabilizer 92
    6.1.3 Electric potential in the kinetic stabilizer 93
6.2 MHD Stabilization 97
6.3 The Trapped Particle Mode 100
6.4 Existence of a fast growing Trapped Particle Mode 108

Chapter 7. Kinetic Stabilization Discussion and Conclusions 110

Bibliography **113**

Vita **121**

List of Figures

1.1 The z component of the magnetic field along the central axis of a generic tandem mirror in Tesla. In this example, each plug consists of a single mirror trap. Charged particles should be confined in the central cell region at high temperatures and densities in order to facilitate fusion. Charged particles also often populate the plug regions, but outside of the plug peaks the temperature and density of particles is much smaller. . . 2

1.2 The electric potential (in kV) for an ambipolar trap in a generic tandem mirror with axial magnetic field shown in Figure 1.1. 6

1.3 (Above) A loss-cone for a system without ambipolar trapping. Particles with a pitch-angle in the green region are trapped. (Below) A loss-hyperbola in velocity space for a system with ambipolar trapping. The region of trapped particles in velocity space has been expanded considerably from the original loss-cone. 8

1.4 A thermal barrier in a generic tandem mirror in kV. 9

1.5 Stength of the z component of the magnetic field along the axis of a generic mirror field where the magnetic field is increasing. (Top) Unstable magnetic field line shape. (Middle) Neutral magnetic field line shape. (Bottom) Stable magnetic field line shape. 12

1.8 The GAMMA-10 coil setup and corresponding magnetic field [19]. 15

1.6 Magnetic flux surfaces in the GAMMA-10, calculated from data provided by Katanuma [18]. 16

1.7 Profiles of the z component of the magnetic field f on the axis of the GAMMA-10. The right-hand side is shown and the left hand side is symmetric about $z = 0$. Initials mark regions set up by the mirror coil configurations: transition region 1, anchor, transition region 2, and the plug-barrier region. 17

1.9 A representative sample of 128 test particle gyro-orbits in an axisymmetric model of the GAMMA-10. 20

1.10 Magnetic flux surfaces in the KSTM. 22

1.11 Axial magnetic field in the right half of the proposed KSTM reactor. 23

2.1 Global radial energy-confinement times, with a variety of scaling laws for the projected KSTM design. Classical drift wave scaling laws (Bohm, gyro-Bohm, and ETG) are normalized to match the empirical L97 results from NSTX at 3.3 MW of radial power loss. At low power, the ISS04 and H98 laws perform best; at high power, the ETG law matches and then exceeds these laws. 27

2.2 Radial energy-confinement times τ_{E} with dimensionless coefficient calibrated to match the most recent reports of 75 ms in the GAMMA-10 [17]. In 2006, axial confinement times reached 100 ms and radial confinement times reached 72 ms at 380 kW of power in the GAMMA-10[30]. Depicted far below these theoretical confinement models are tokamak and stellarator confinement time scaling laws derived from large experimental databases. Energy-confinement time from the GAMMA-10 reported by Tamano in 1995 are on the order of 10 ms [20]. These older results agree fairly well with the various toroidal databases. . 29

2.3 A comparison of radial energy confinement times τ_E and the axial loss time $\tau_{||}$ for various electron temperatures T_{e} in the GAMMA-10. 34

3.1 Two scalar functions are used to construct a 3 dimensional magnetic field: the axial magnetic field f (above) and the quadrupole magnetic field g (below). These graphs show the right side of the machine. f is symmetric and g can either be symmetric or antisymmetric. Data provided by personal correspondence with Katanuma [18]. 38

3.2 The field line radius and magnetic flux in an axisymmetric tandem mirror. In this case the flux coordinates are simple to visualize. θ and z are identical to the same coordinates in cylindrical space. The third flux coordinate, the flux itself, ψ, is a constant that dictates the relationship between radius and the magnetic field. Because ψ is constant along any field line, by specifying ψ the flux surface is determined, and thus the magnetic field line radius $r(z)$. A scaled version of f is given in the background of the figure for reference. 41

3.3 A perfectly circular field-line surface at $z = 0.5$ m is distorted into an oval shape at $z = 3.8$ m, and then stretched in the opposite direction at $z = 7$ m. 48

3.4 Axial magnetic field in the KSTM, along with normal and geodesic curvatures for this machine. Negative values of κ_ψ are destabilizing regions, and positive regions of κ_ψ contribute to the overall MHD stability. The relationship between curvature and stability will be worked out mathematically in section 4.7. . . 51

3.5 Normal and geodesic curvatures in the GAMMA-10, (above) at $\theta = 0$ and (below) at $\theta = \pi/4$. The geodesic curvature vanishes at $\theta = 0$, but is on the same order as the normal curvature for $\theta = \pi/4$. Data provided by the I. Katanuma and the GAMMA-10 team [18]. 52

4.1 (Above) The eigenmodes that correspond to the three lowest eigenvalues of the Mathieu equation for $q = 1$. (Below) A plot of the odd eigenvalues for various Mathieu equation q values produced by our F90 code (marked by x's), and their formulas given in Abramowitz and Stegun [47] section 20.2.25 (the low q formula denoted by dashed lines) and 20.2.30 (the high q formula denoted by solid lines). 66

4.2 (Above) The lowest eigenmode of eq. (4.36), often called the flute mode for a tandem mirror like the KSTM before a kinetic stabilizer is applied. ω_{A}^2 is the Alfvén frequency. Since ω^2 is negative the system is unstable. In the background a scaled version of f is given for reference. (Below) The second and third lowest eigenmodes of eq. (4.36). These modes are stable because ω^2 is positive and thus these MHD growth rates are zero. 67

5.1 The magnetic field f in two cells of our multiple mirror configuration. Particles are either reflected or transmitted at the peaks of the mirror field at L, $2L$, etc. 74

5.2 Frequency *vs.* wavenumber calculated with a shooting method, for a multiple mirror with an infinite number of cells of varying mirror depth M. The model of magnetic field used in eq. (5.3) is $f = 1 + M \sin z$ at zero plasma pressure, $\beta = 0$. The lines show frequency data from a multiple mirror with an infinite number of cells. The various plotted points show data from a reflection coefficient calculation performed on a modulated mirror with a finite number of mirror cells. 76

5.3 The reflection and transmission coefficients for a model of the LAPD magnetic profile. This model consists of 4 mirror cells defined by a $f = 1 + M \cos z$, where $M = .25$. We find a frequency gap at $\omega/\omega_{\mathrm{A}} = 0.5$ (where the reflection coefficient approaches 1) with a gap width of $\Delta\omega/\omega_{\mathrm{A}} = 0.208 < M$. . . . 77

5.4 The reflection and transmission coefficients for a magnetic field similar to the LAPD, but with twice as many mirror cells. This model consists of 8 mirror cells defined by a $f = 1 + M \cos z$, where $M = .25$. We find a frequency gap of $\Delta\omega = 0.155 \approx M/2$ which approaches the result obtained from an infinite array of equally spaced mirror wells. 78

5.5 Magnitude of frequency *vs.* wavenumber calculated with a shooting method. Here we examine an infinite mirror array described by $f = 1 + M \sin z$ (and setting M to a modest 0.26) while varying β. As the dimensionless plasma pressure β is increased, instability develops. The box draws attention to these growth rate magnitudes. 79

5.6 Spectral gaps calculated from the reflection coefficient for the LAPD fall in the frequency range $M/2 < \omega/\omega_{\mathrm{A}} < 2M$. This is a frequency range that covers the experimental data collected by Zhang, *et al.* (depicted as red points with error bars). . . 80

5.7 The amplitudes of the reflection and transmission coefficients, r and t for the GAMMA-10 magnetic profile in the case of vanishing plasma pressure $\beta = 0$. 82

6.1 A trapped particle mode in a tandem mirror. Electrons are indicated in green; there are electrons trapped in the plug, connecting electrons that sample the plug and kinetic stabilizer regions, and electrons from outside the machine that reflect off of the ambipolar potential in the plug. Ions are indicated in pink. Most ions are trapped in the plug region by the ambipolar potential, those that are not leave the expander immediately. 85

6.2 Model for the magnetic field-line radius r (above) and the axial magnetic field f (below). These particular fields are representative of the shape we are taking, but we consider a wide range of lengths for the expander region, and a wide range of magnitudes for the axial magnetic field. 86

6.3 (Above) Ion density in the expander created by the kinetic stabilizer beam. The red dashed line shows density peak in the limit of small ε, the width of the μ distribution. The green dashed line shows the density profile if the target is moved into the plug region. (Below) The corresponding pressure for $\varepsilon = 0.1$. For this example machine the target is taken at $z_{\mathrm{T}} = 98$ m, $E_0 = 200$ eV and $\varphi_{\mathrm{T}}/E_0 = 0.58$, $T_{\mathrm{e}}/E_0 = 0.64$. Both density and pressure are significantly lower than density and pressures in the plug region. 89

6.4 Electron temperature of a short-mean-free-path electron distribution *vs.* the value of the electric potential at the target φ_{T}. Both quantities are normalized to the energy of the incoming beam E_0. 95

6.5 Potential φ in the case of a Maxwellian electron distribution. For this choice of parameters ($\varepsilon = .1$, $\varphi_{\mathrm{T}}/E_0 = .3$) the potential has two characteristic types of solutions: those that are positive for all B/B_{T} , and those that become negative as B/B_{T} increases. The dashed lines show the limit of each φ as the magnetic field becomes large. 96

6.6 A successful operating regime for an axisymmetric mirror that is MHD stable as a consequence of kinetic stabilizers is indicated by the shaded region. We assume that the target is at or near the beginning of the favorable curvature region, and take into account the paraxial condition, the adiabaticity condition, and MHD stability. The critical energy $E_{0\mathrm{c}}$ and magnetic field at the wall B_{wc} are defined in eqs. (6.23) -(6.24). 99

6.7 The effective potential for Maxwellian electrons in the whole expander region, the range B/B_{T} = 0.1- 20 corresponds to $B_{\mathrm{w}} < B < B_{\mathrm{m}}$. In these graphs $\mu_{\mathrm{m}} = \varphi_{\mathrm{p}}/(B_{\mathrm{m}} - B_{\mathrm{w}})$. 103

6.8 The fraction of electrons in the expander that are trapped (above), and that are both trapped and connect the kinetic stabilizer to the plug region (below) for a Maxwellian electron distribution at constant electron temperature $T_{\mathrm{eks}}/E_0 = 0.072$ *vs.* magnetic field at the target normalized to its maximum value. 106

6.9 The fraction of electrons in the expander that are trapped (above), and that are both trapped and connect the kinetic stabilizer to the plug region (below) for a Maxwellian electron distribution *vs.* ε, the dimensionless parameter that controls the distribution of magnetic moments in the kinetic stabilizer beam. 107

List of Tables

1.1 Machine Parameters 24

2.1 Comparison of Radial and Axial Loss Rates 32
2.2 Summary of Global Scaling laws for Radial Loss Times τ_E (s) 33

6.1 Parameters for marginally MHD-stable KSTM design 105

Chapter 1

Principles of Tandem Mirrors

The tandem mirror magnetic-fusion confinement system is a long cylindrical solenoid terminated by a set of plug cells. If we consider a single test particle moving in such a solenoid, that particle's *radial* motion would be confined as long as no collisions occur to kick it out of the machine. But a particle could escape along the axis of the solenoid, so plugs are added to the ends of a finite solenoid in order to reflect particles that would otherwise escape axially. These plugs consist of one or more mirror fields designed for maximal confinement and stability. Common additions that increase the ability of the plugs to confine particles are ambipolar traps and thermal barriers, which we will discuss in detail in section 1.3. The magnetic field in a generic tandem mirror that possesses a single magnetic mirror in each plug is shown in Figure 1.1. The plug regions are susceptible to instabilities, and there are many design ideas to stabilize unstable modes that may be excited; among these are expander outflow plasmas, non-paraxial end plugs, cusp end plugs, and wall-stabilization techniques [1]. In this work, two of these stabilizing schemes are discussed: the stabilization of the plugs by adding a quadrupole magnetic field in order to create a minimum-B configuration, and the kinetic stabilizer. Outside of the plug region, there is often an expander region that guides the shape of the escaping plasma.

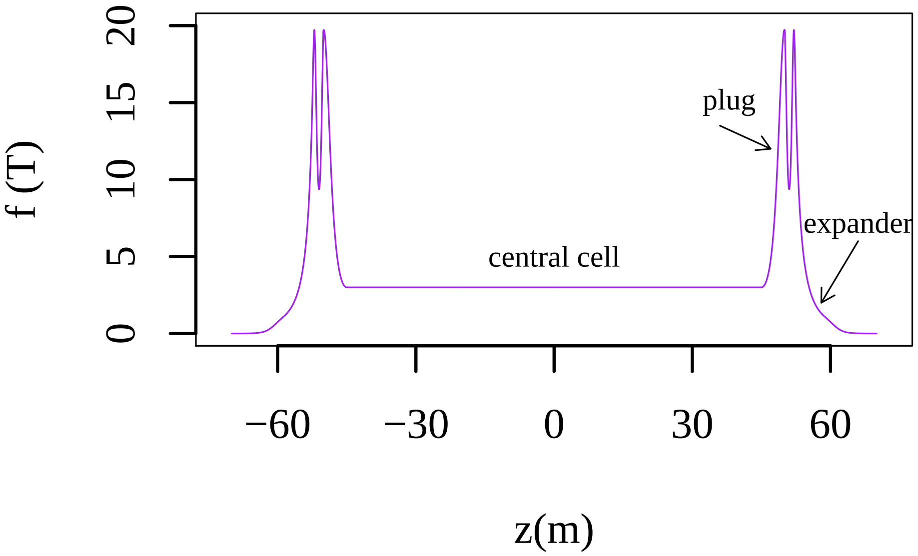

Figure 1.1: The z component of the magnetic field along the central axis of a generic tandem mirror in Tesla. In this example, each plug consists of a single mirror trap. Charged particles should be confined in the central cell region at high temperatures and densities in order to facilitate fusion. Charged particles also often populate the plug regions, but outside of the plug peaks the temperature and density of particles is much smaller.

In the late 1980's, the collaborative effort toward mirror research in the United States, known simply as the "mirror program," was defunded. This program pursued fusion research from a different point of view from the tokamak design, and made the field of research of fusion plasmas considerably richer and more diverse. The mirror program consisted of a large group of theorists as well as a number of tandem mirror machines: TARA at MIT, Phaedrus at the University of Wisconsin, as well as a progression of machines at Lawrence Livermore National Laboratory, the TMX, TMX-U (Tandem Mirror Experiment Upgrade) and the nearly-completed MFTF-B (Mirror Fusion Test Facility). Twenty years later, new technologies, new machine designs, and important break-through results from the GAMMA-10 machine built in Tsukuba, Japan [2] and the Gas Dynamic Trap (GDT) at Novosibirsk have rejuvenated interest in a tandem mirror research effort.

1.1 The Mirror Trap

The plugs of a tandem mirror always possess a mirror trap, or mirror field; a mirror trap is simply the double-peaked field shown in Figure 1.1. As we will work out below, a charged particle will reflect off of a sufficiently high peak in the magnetic field. A mirror field is designed to trap particles by forcing them to bounce between the two peaks. In a tandem mirror, like the one pictured in Figure 1.1, the high magnetic field of the plugs traps many particles in the central cell region; the double-peaked mirror field in each plug also traps particles in the plug region. Some tandem mirrors, like the GAMMA-10 that we will discuss in detail in section 1.6, have several mirror fields for each plug. The idea for a mirror trap was first put forth in the 1950s by G. I. Budker in the USSR and independently by R. F. Post in the USA [3]. Two simple particle properties make confinement of particles in a mirror field possible: the conservation of particle energy U_0, and the adiabatic invariance of the magnetic moment μ:

$$\begin{aligned} U_0 &= \frac{1}{2}mv_\perp^2 + \frac{1}{2}mv_{||}^2 = \text{const} \ , & (1.1) \\ \mu &\equiv \frac{1}{2}mv_\perp^2/B \propto \oint \boldsymbol{p} \cdot d\boldsymbol{q} \ . & (1.2) \end{aligned}$$

Here m is particle mass and $v_\perp$ is the velocity perpendicular to the magnetic field B. Physically, the magnetic moment can be thought of as the magnetic moment of a Larmor orbit. μ can be considered a constant if the Larmor radius is less than the characteristic scale for change of the magnetic field [3]. The trapping of charged particles by a mirror field is well established both mathematically and in the laboratory [4]. We define the pitch-angle of a particle, α, to be the angle between the velocity vector of the particle and the magnetic field so that $v_\perp = |v| \sin\alpha$. Particles will be lost if $\sin\alpha$ is too small. We can calculate the pitch-angle necessary for a particle in the central cell, where $B = B_{\text{min}}$ and $v = v_0$, to be trapped by the mirror field

$$\begin{aligned} U_0 &= \mu B_{\text{min}} + \frac{1}{2}mv_0^2(1 - \sin^2\alpha_{\text{crit}}) \leq \mu B_{\text{max}} \ , & (1.3) \\ \sin\alpha_{\text{crit}} &\geq \sqrt{\frac{B_{\text{min}}}{B_{\text{max}}}} \ . & (1.4) \end{aligned}$$

The important confinement parameter for magnetic mirrors is the mirror ratio as $R_M = \frac{B_{\text{max}}}{B_{\text{min}}}$, which serves as a way to measure the trapping ability of a magnetic trap. $R_M = 7.5$ is the mirror ratio of the GAMMA-10 tandem mirror. If a particle has sufficiently small pitch-angle $\alpha < \alpha_{\text{crit}}$, it can escape the ends of the mirror. For particles confined in a mirror field, the distribution of velocities is characterized by a "loss-cone" defined by R_M. The upper figure in Figure

1.3 demonstrates how this loss-cone appears in velocity space. If a trapped particle collides with other particles it can escape rapidly from the ends of the mirror, or diffuse radially and be lost. When we discuss ambipolar potentials in section 1.3, we must modify eq. (1.4) to include an electric potential.

1.2 The Problem of End-Losses

Particles that stream out of the ends of a the tandem mirror are referred to as end-losses; end-losses have long been acknowledged to be a major challenge of tandem mirror design. A system that used only mirror traps to confine particles axially would always exhibit confinement times that were dominated by end-losses. In the usual low-collisionality fusion regimes, the time that it takes for particles to escape is on the order of the classical Coulomb ion-ion collision time. The GAMMA-10 has demonstrated experimentally that the ends of a tandem mirror can be plugged efficiently so that radial losses are dominant.

1.3 The Ambipolar Trap

Collisions can change the pitch-angle of a particle, and after a collision the pitch-angle of a particle may change so that it will be lost axially or radially if no other trapping mechanism is present. In order to confine particles with a greater range of pitch-angles, the mirror cells arrayed at both ends of the tandem mirror are equipped with a positive electrostatic confinement potential ϕ_{c}, which reflects small pitch-angle ions back toward the central cell.

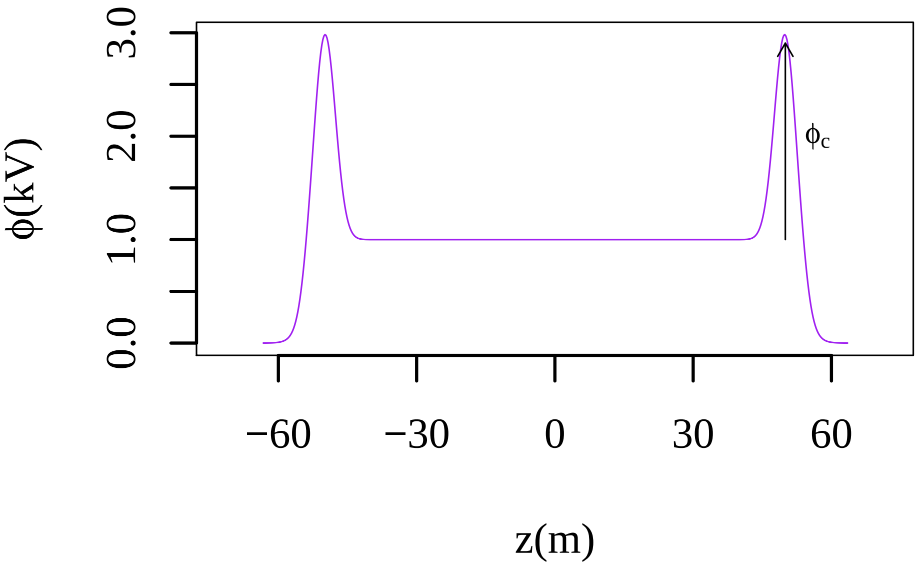

Figure 1.2: The electric potential (in kV) for an ambipolar trap in a generic tandem mirror with axial magnetic field shown in Figure 1.1.

This mechanism is called an ambipolar trap [5]; the name “ambipolar” comes from the fact that an electrostatic potential of the plasma relative to the machine walls builds up to equalize the loss rate of the ions and electrons. A simple ambipolar potential can occur naturally. Initially a plasma is quasi-neutral ($n_i \approx n_e$). Because electrons have higher velocities than ions, they scatter more rapidly. The axial confinement time of a particle is proportional to its scattering time, thus electrons scatter into the loss-cone and begin to escape the mirror. The particles that remain in the mirror establish a net positive charge. The electric potential, ϕ, from the net positive charge constitutes an ambipolar trap that helps to confine the electrons axially. To form a large potential peak, neutral beams are typically injected into the magnetic-mirror region in order to build up a density peak. If the density in the plug, n_p, is greater than the density in the central solenoid, n_c, then an ambipolar potential ϕ_c is formed, where

$$e\phi_c = T_e \ln \frac{n_p}{n_c} \ , \tag{1.5}$$

where T_e is the temperature of electrons. If $e\phi_c >> T_e$ the time of longitudinal confinement of the plasma in the ambipolar trap is many times longer than that of a simple mirror without such an ambipolar trap [6]. The resulting potential is represented in FIG. 1.2. We can modify eq. (1.4) for the case of a simple ambipolar potential:

$$\begin{aligned} U_0 &= e\phi + \mu B_{\min} + \frac{1}{2} m v_0^2 (1 - \sin^2 \alpha_{\text{crit}}) \leq \mu B_{\max} \qquad (1.6) \\ \sin \alpha_{\text{crit}} &\geq \sqrt{\frac{B_{\min}}{B_{\max} - e\phi/\mu}} \ . \qquad (1.7) \end{aligned}$$

This condition on the pitch-angle for a particle to be trapped in a magnetic well with an ambipolar potential, eq. (1.7), modifies the loss-cone to a hyperbole shape, as shown in Figure 1.3.

1.3.1 Thermal Barriers

The main function of the thermal barrier is to provide thermal insulation for the electrons in the end plug, so that they do not contact those in the solenoid. The thermal barrier consists of a depression in the positive potential, that appears to the negatively charged electrons as a potential barrier.

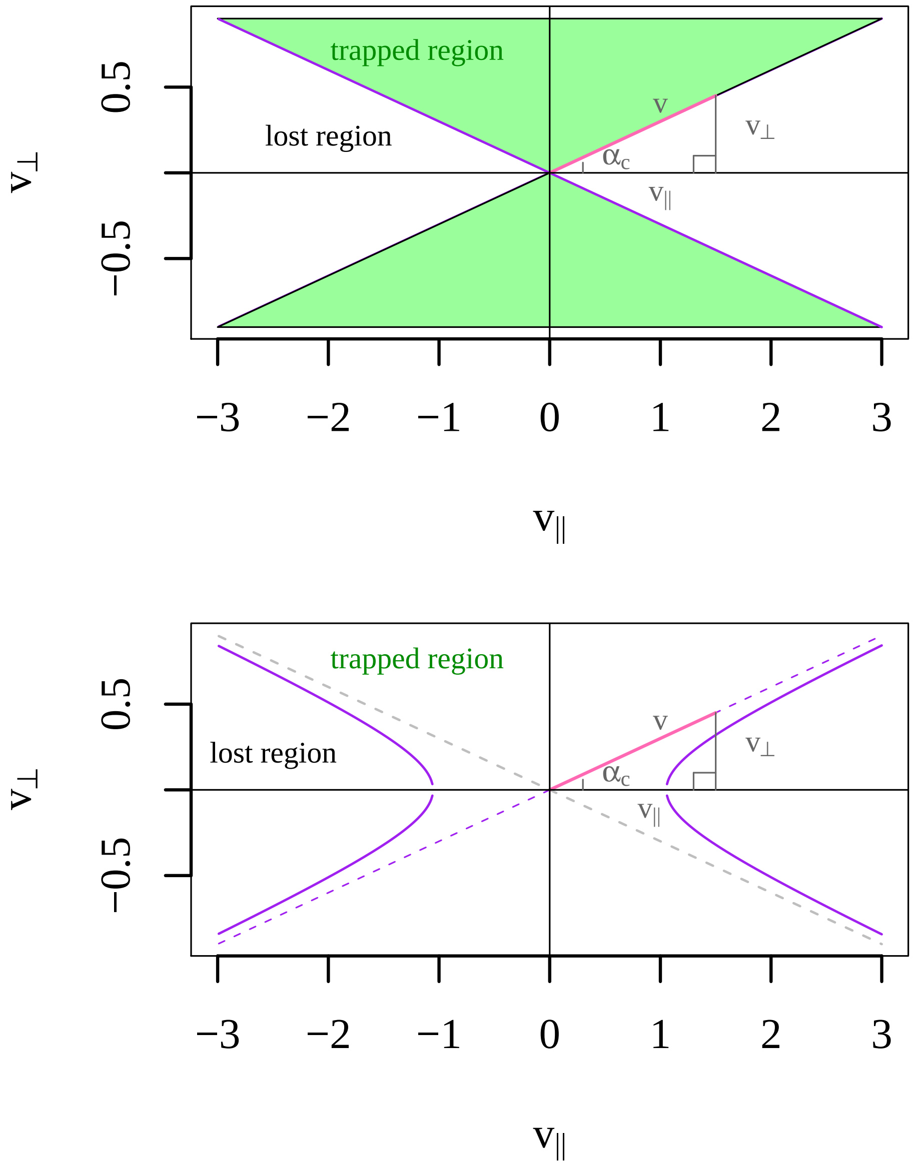

Figure 1.3: (Above) A loss-cone for a system without ambipolar trapping. Particles with a pitch-angle in the green region are trapped. (Below) A loss-hyperbola in velocity space for a system with ambipolar trapping. The region of trapped particles in velocity space has been expanded considerably from the original loss-cone.

This is represented in Figure 1.4, where the thermal barrier is represented by the potential depression ϕ_b. If the electrons in the plug are heated up with electron-cyclotron resonant heating (ECRH) or some other heating scheme, a thermal barrier allows the electron temperature in the plug to stay much hotter than the electron temperature in the central cell. The potential peak just following ϕ_b can then be generated with a lower plasma density [7]. The thermal-barrier concept improves the performance of tandem-mirror systems by reducing the energy of neutral beams necessary to create a potential ϕ_c.

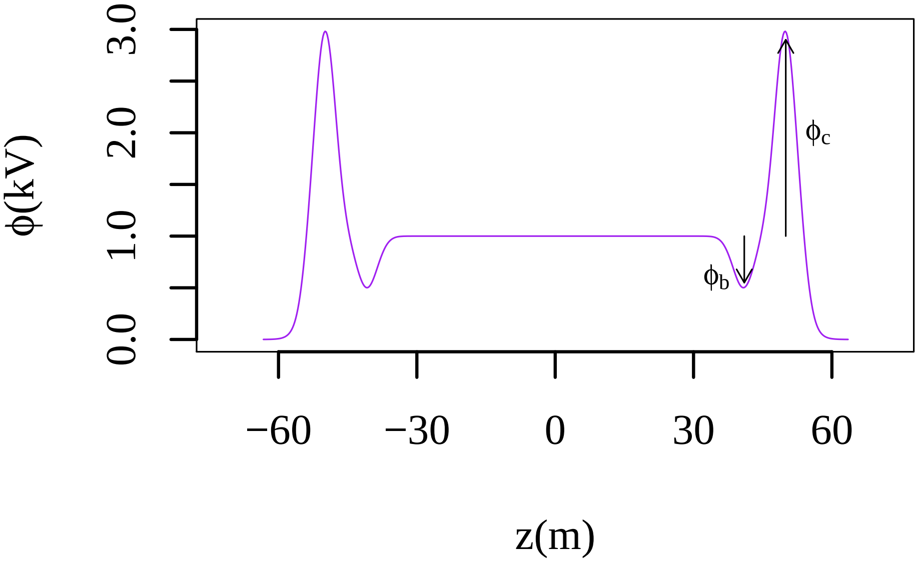

Figure 1.4: A thermal barrier in a generic tandem mirror in kV.

1.4 General Properties of Tandem Mirrors

Tandem mirror designs have a number of unique advantages over comparable-size toroidal machines. Field-lines in tandem mirrors are nearly straight, whereas the system of poloidal and toroidal magnetic fields that occur in toroidal devices leads to a complex web of field-lines that fill the torus. As a result, tokamaks have banana-shaped and potato-shaped gyro-orbits, with sizes that must be controlled by the poloidal magnetic field [8]. Tandem mirror systems have relatively simple particle gyro-orbits that reflect off the mirror fields, and bounce back and forth in the central cell. We visualize these gyro-orbits in section 1.6.1.

Toroidal systems possess cross-field transport dominated by plasma turbulence. This is a result of toroidal magnetic fields; the plasma in toroidal systems is continually accelerating outward, causing large scale magnetohydrodynamic (MHD) instabilities and also micro-scale drift-wave instabilities. Various solutions have been found to stabilize modes that are large and unstable. The plasma β is a dimensionless parameter that quantifies the effect of the magnetic field on a plasma. β is defined as the ratio of the thermal energy density to the magnetic energy density

$$\beta = \frac{p}{B^2/2\mu_0} \tag{1.8}$$

where the plasma pressure $p = nT$ is used. By keeping the plasma pressure low and its radial gradient below both the ideal β limit and the limit for ballooning interchange modes, ballooning instabilities and large radially-extended structures can be avoided [9]. Despite these efforts, micro-scale turbulent instabilities remain a significant problem in tokamaks. Tandem mirrors that are axisymmetric have experimentally demonstrated plasma confinement in near-classical states, *i.e.* the plasma dynamics are not dominated by fluctuations and turbulence levels are extremely low. Because of this property, tandem mirrors are predicted to be able to have order unity β in an equilibrium state. Because anomalous transport due to micro-turbulence is so low in an axisymmetric tandem mirror, a tandem mirror provides an excellent setting for understanding the effects of anomalous cross-field transport. Axisymmetric tandem mirrors are susceptible to several other types of instabilities, magnetohydrodynamic (MHD) instabilities, as well as trapped particle instabilities. It is these instabilities that will be the focus of later chapters.

A tandem mirror is a convenient machine to study fusion plasmas. In open systems the radial boundary of the confined plasma can be far from the material surfaces, avoiding turbulence-producing radial temperature gradients and plasma sheath effects inherent in closed systems. Experimentally it is easier to access the plasma to make exterior measurements, as well as to control the profile of the radial electric field, because the design is not folded on itself. This is accomplished either through direct end-plate control or with the use of localized electron cyclotron heating (ECH) power that increases the intrinsic ambipolar potential. Control of the radial electric field profile is demonstrated in the GAMMA-10 by the ECH heating in the plug barrier plasmas with $P_{ECH}^{\text{plug}} \leq 380$ kW [10].

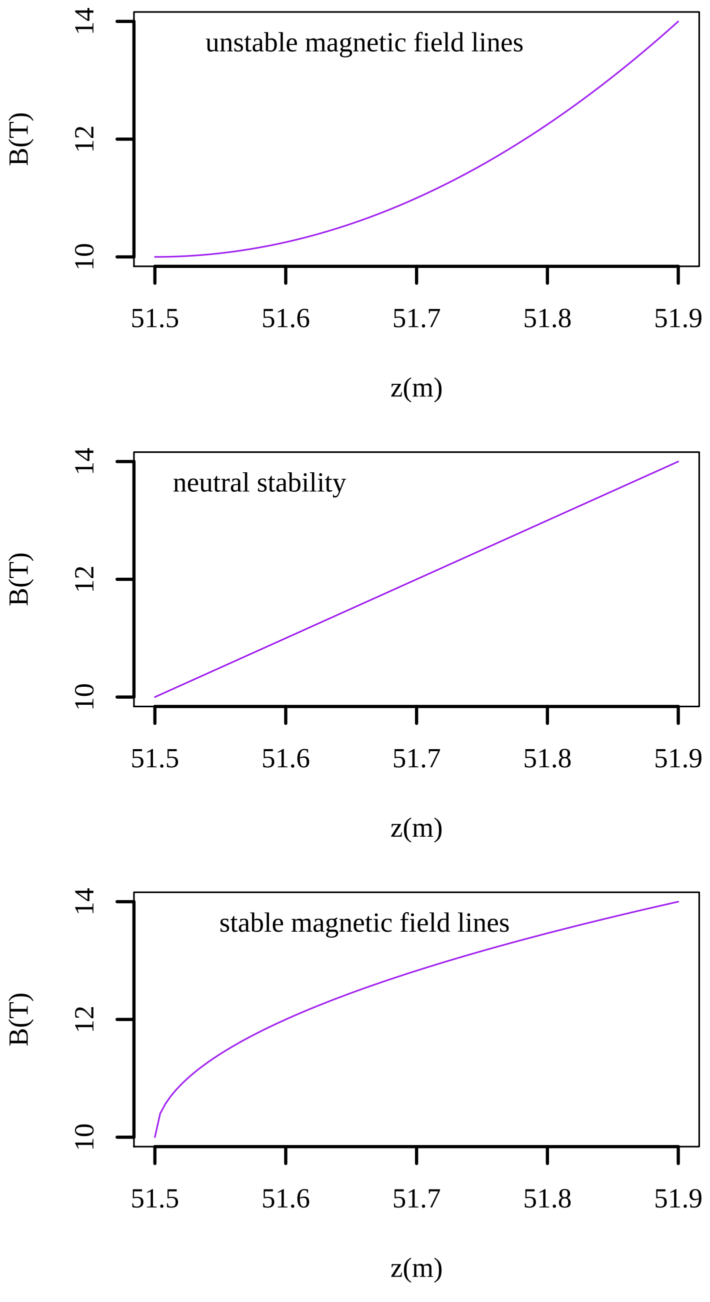

Figure 1.5: Stength of the z component of the magnetic field along the axis of a generic mirror field where the magnetic field is increasing. (Top) Unstable magnetic field line shape. (Middle) Neutral magnetic field line shape. (Bottom) Stable magnetic field line shape.

In a tandem mirror, there is a natural and efficient way to take advantage of the fusion energy which is released from the machine in the form of charged particles; these particles escape the ends of the machine and are aligned well with the axis of the machine. There are a number of designs for direct conversion of this current to energy [11]. There is also great interest in using a tandem mirror as a neutron source [12].

1.5 Minimum-B Stability

In 1961, Ioffe reported that magnetic fields with positive field line curvatures are effective in suppressing MHD instabilities in open systems. Ioffe conducted his experiment by transforming the simple unstable mirror magnetic field line geometry to a stable one by superimposing six linear conductors (later called Ioffe bars) carrying opposing current in adjacent conductors. He found a dramatic increase in plasma confinement when the current in the Ioffe bars reversed the magnetic field line curvature. This stable setup is called a minimum-B mirror, or a magnetic well, because the magnetic field strength increases in all directions. In a minimum-B configuration, there exists a point which is a local minimum of B^2. In the neighborhood of this point, the contours defined by constant B^2 (these curves are magnetic isobars, not flux surfaces) form a set of closed nested surfaces. A surface of larger B^2 envelops those of smaller B^2. B^2 increases both axially and radially; the magnetic pressure is lower inside any given surface than outside it, *i.e*, there is an outwardly increasing field that creates stability [13]. This simple picture of what Ioffe discovered is illustrated in Figure 1.5, with a minimum-B field shown in the lowest panel. This minimum-B configuration provides line-average MHD stability of an entire tandem mirror system by field-line-tying to the central cell. The implication of the famous Ioffe experiment for tandem mirrors is use of non-axisymmetric fields characterized at all azimuthal angles by positive field line curvature at the radial boundary of the plasma to suppress the MHD interchange instability [14].

In this work we discuss two tandem mirror machines: the Japanese GAMMA-10 machine, and the kinetically stabilized tandem mirror machine (KSTM), an innovative design proposed by D.D. Ryutov, R.F. Post, and K. Fowler [15] [16].

1.6 The GAMMA-10 Experiment

The GAMMA-10 is a tandem mirror machine first built in 1980-81 at the University of Tsukuba's Plasma Research Center in Tsukuba, Japan. As it is currently built, the GAMMA-10 employs non-axisymmetric anchor regions before the axisymmetric plugs to achieve MHD stability. Three MHD-stabilizing quadrupole cells sit immediately outside the central cell. On the outside of the quadrupole cells is the plug/barrier cell, which consists of a thermal barrier, an ambipolar trap and a final axisymmetric mirror cell. Because it is not a fully axisymmetric tandem mirror, it must contend with the enhanced radial transport that would be absent in an axisymmetric machine. However, in the last few years, the GAMMA-10 team have experimented with a sheared radial electric field, and had great success in suppressing turbulent fluctuations. The experimental team has achieved high electric potentials in the plugs, and high electron temperatures approaching 1 keV in the central cell [17]. The three dimensional shape of the full GAMMA-10 machine is depicted in Figure 1.6, which shows the magnetic flux surface of the machine.

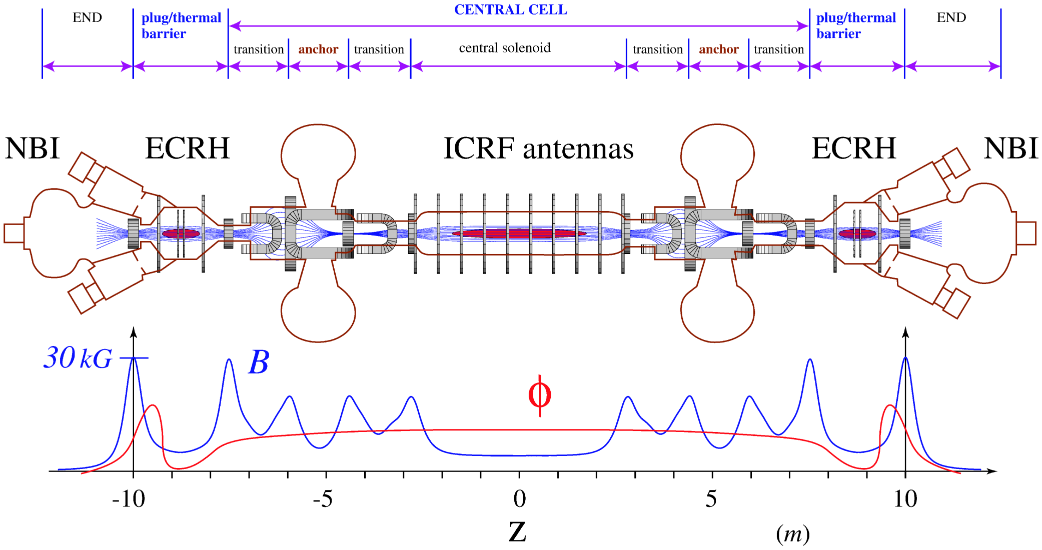

Figure 1.8: The GAMMA-10 coil setup and corresponding magnetic field [19].

Figure 1.7 shows the on-axis magnetic field that describes the geometry of the GAMMA-10, and Figure 1.8 shows a detailed set-up of the coils. Pictured in Figure 1.7 is the analytical model we have constructed to match the data provided by Katanuma [18]. Based upon the average relative variance $(1/N)\sum_1^N (x_i - y_i)^2/\sigma_y^2$, our model matches the variation of the data y_i with 99% accuracy. The GAMMA-10 is axisymmetric except for the anchor

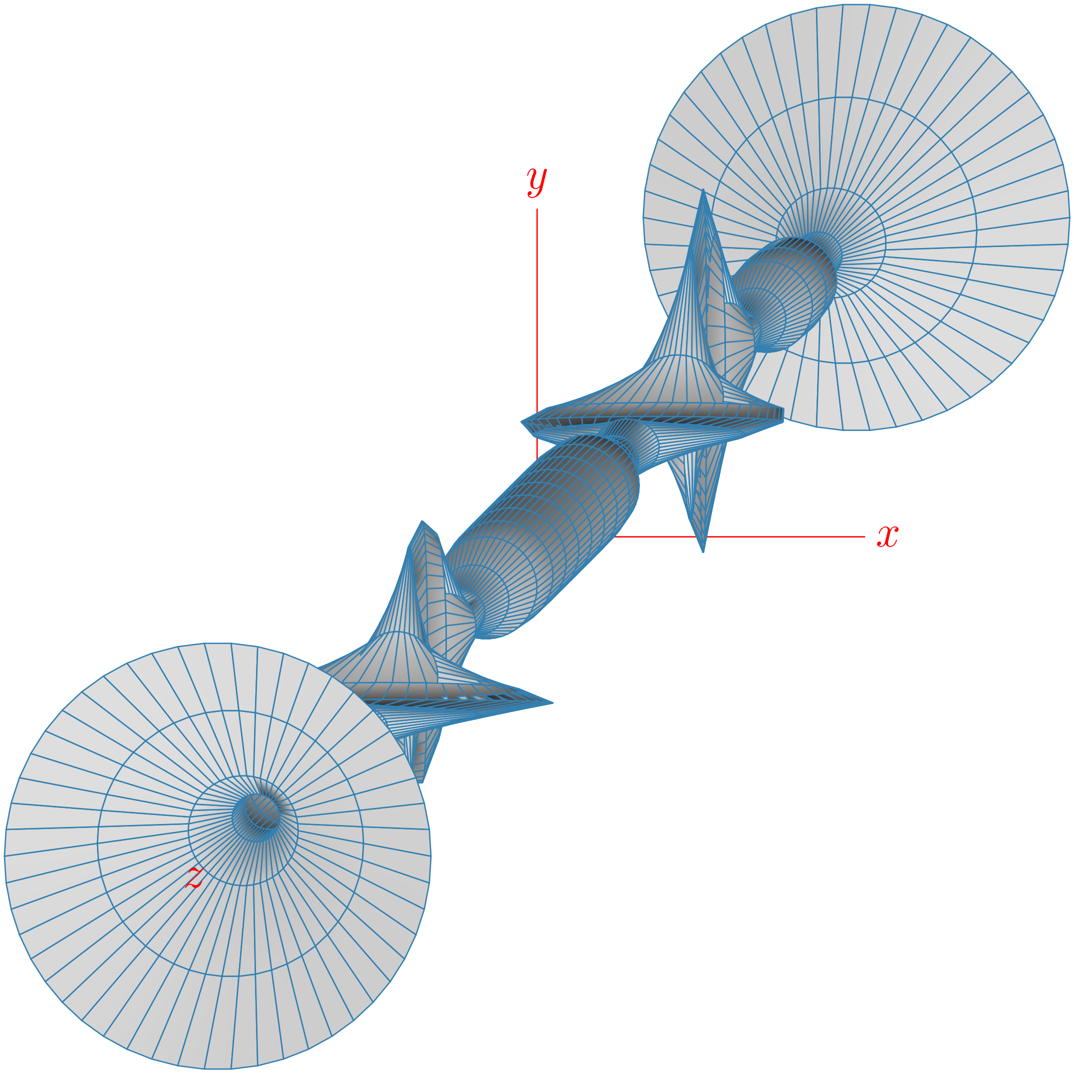

Figure 1.6: Magnetic flux surfaces in the GAMMA-10, calculated from data provided by Katanuma [18].

cell (labeled “A” in Figure 1.7) where a quadrupole magnetic field is applied to insure MHD stability. The GAMMA-10 is a minimum-B system, so sufficient plasma pressure in the minimum-B anchor cells must be built up before heating the bad-curvature central cell region. The plasma pressure is built up

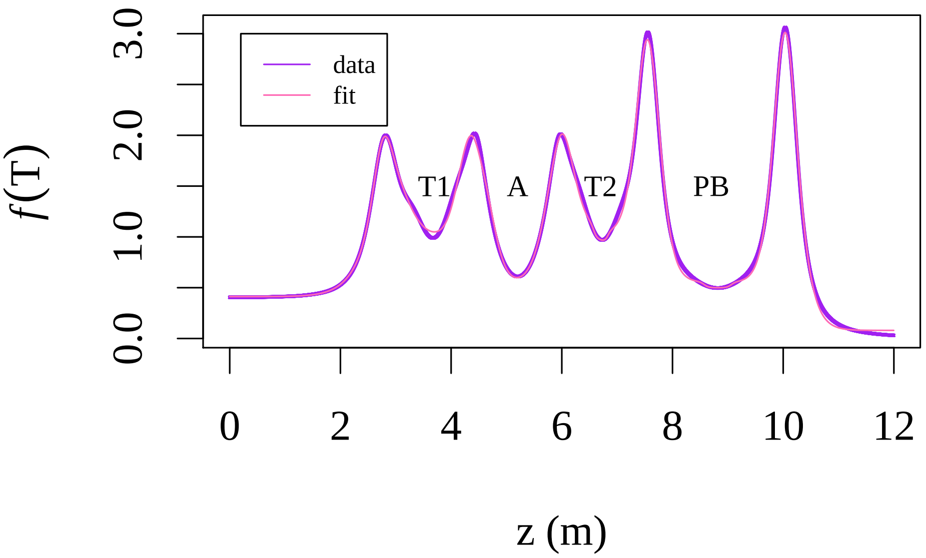

Figure 1.7: Profiles of the z component of the magnetic field f on the axis of the GAMMA-10. The right-hand side is shown and the left hand side is symmetric about $z = 0$. Initials mark regions set up by the mirror coil configurations: transition region 1, anchor, transition region 2, and the plug-barrier region.

with neutral beam injections (NBI). If the central cell pressure increases too rapidly, an MHD crash occurs [20].

In 1988, Ryutov [3] summarized the challenges facing tandem mirror research with non-axisymmetric magnetic fields in terms of two major challenges: increased loss of particles in the radial direction and micro-fluctuations. Non-axisymmetric machine configurations enhance the radial plasma loss; this problem is exacerbated by the ever-more-efficient plugs of tandem mirror machines that increasingly suppress end-losses. Currently the GAMMA-10 team reports that energy losses in the radial direction are greater than losses from the ends of the machine [17]. The results here are a combination of success at plugging the ends of their machine, and the possibility that radial losses have become increasingly difficult to manage. The second major challenge that Ryutov outlined is that increasing plasma density in nonaxisymmetric machines can lead to a loss of confinement due to plasma micro-fluctuations. Tandem mirrors designs often exhibit naturally occurring strong, radially-sheared flow [20]. This radial shear provides a measure of radial confinement in the tandem mirror similar to the set up of an H-mode plasma or internal transport barrier in a tokamak. The radially-sheared electric field also has the property of suppressing turbulent fluctuations in the GAMMA-10 [10]. If this were verified, it could be a successful method of resolving micro-fluctuations in a nonaxisymmetric tandem mirror.

1.6.1 Particle orbits in the GAMMA-10

In contrast to toroidal devices, mirror systems have relatively simple particle gyro-orbits. To visualize the gyro-orbits in a modern functional tandem mirror, the GAMMA-10, we have developed a parallel code to follow independent test particles in a fully axisymmetric version machine. These test particles do not interact with one another and do not modify the magnetic field. Using Lorentz force law $\boldsymbol{F} = q(\boldsymbol{E} + \boldsymbol{v} \times \boldsymbol{B})$ we obtain governing equations

$$\begin{aligned}
\frac{dz}{d\tau} &= v_z/\omega_c \ , &(1.9)\\
\frac{dx}{d\tau} &= v_x/\omega_c \ , &(1.10)\\
\frac{dy}{d\tau} &= v_y/\omega_c \ , &(1.11)\\
\frac{d\boldsymbol{v}}{d\tau} &= (\boldsymbol{E} + \boldsymbol{v} \times \boldsymbol{B})/|B| \ . &(1.12)
\end{aligned}$$

Here time is scaled by the cyclotron frequency $\tau = t\omega_c$. Our simulation integrates orbits for 5 keV protons; results can be seen in Figure 1.9. The graph shows 128 ions, and 11 are lost from the machine in 1.3 ms. These ions are launched from the middle of the central cell with initial velocities sampled from a Gaussian in all three directions, and exhibit a simple circular gyro-orbit. Particles with a positive initial velocity in the z direction are colored red; particles with a negative initial velocity in the z direction are colored blue. Particles bounce between the plugs in an axisymmetric tandem mirror and reflect off of the magnetic field, this can be verified visually. This simulation was performed using a F90 MPI code run on Lonestar (5,200 compute-node Dual-Core Linux Cluster, peak performance speed 55 TFLOPS) at the Texas Advanced Computing Center.

1.7 The Kinetically Stabilized Tandem Mirror

Ryutov established that an MHD-unstable plasma confined between mirrors can be stabilized if there exists a sufficient density of effluent plasma

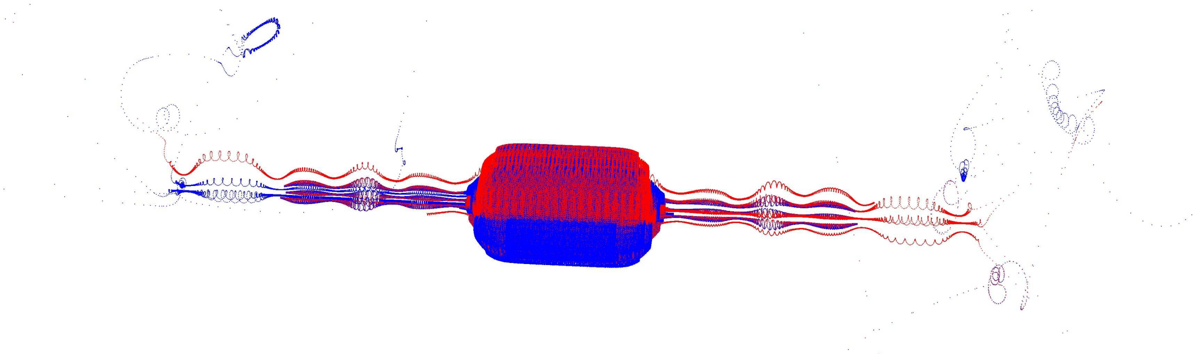

Figure 1.9: A representative sample of 128 test particle gyro-orbits in an axisymmetric model of the GAMMA-10.

on the expanding (positive curvature) field lines outside the mirrors; this technique of stabilization was experimentally confirmed using the axisymmetric Gas Dynamic Trap (GDT) at Novosibirsk [9]. The GDT is a single mirror trap with an extremely high mirror ratio, $R_M = 12 - 100$. The GDT operates in a high-collisionality regime in order to keep the loss-cone full; the presence of highly collisional plasma flowing out of the ends of the machine in the positive-curvature expanding-field region outside the mirrors was effective in stabilizing a high-beta ($\beta = 0.3$) confined plasma against MHD modes [21]. In other words, for the Gas Dynamic Trap, MHD stability is provided by the flow of plasma escaping through the ends of the mirror. This stabilization mechanism works because the field-line curvature outside the mirror well is favorable for stability, and the large density of effluent plasma weights the favorable curvature region heavily enough to stabilize the negative curvature effect of the plug region.

In the typical tandem mirror the ends of the machine are effectively plugged to prevent plasma from flowing out of the machine. The density of the effluent plasma is too low provide stability by the plasma outflow mechanism as in the GDT, and the collisionality of the expander plasma is also low. The kinetic stabilizer solves this problem by using ion beams, injected axially at small pitch angles α, toward the higher magnetic of the plug to a specific point in the expander region; this creates a localized stabilizing plasma by magnetic compression and reflection of the injected ions at a target chosen in the expander cell. The expander cell is shown in Figure 1.11. A kinetic stabilizer was originally proposed by Ryutov [22] and has been further developed by R.F. Post and K. Fowler [23]. Post has demonstrated that the kinetic stabilizer does indeed provide MHD stability to an axisymmetric tandem mirror design.

The proposed Kinetically Stabilized Tandem Mirror (KSTM) reactor is a simple axisymmetric tandem mirror, with ambipolar traps in the plugs but no thermal barrier. A model of the flux surfaces of the KSTM reactor is depicted in Figure 1.10. Table 1.1 gives typical parameters of the GAMMA-10 and KSTM systems.

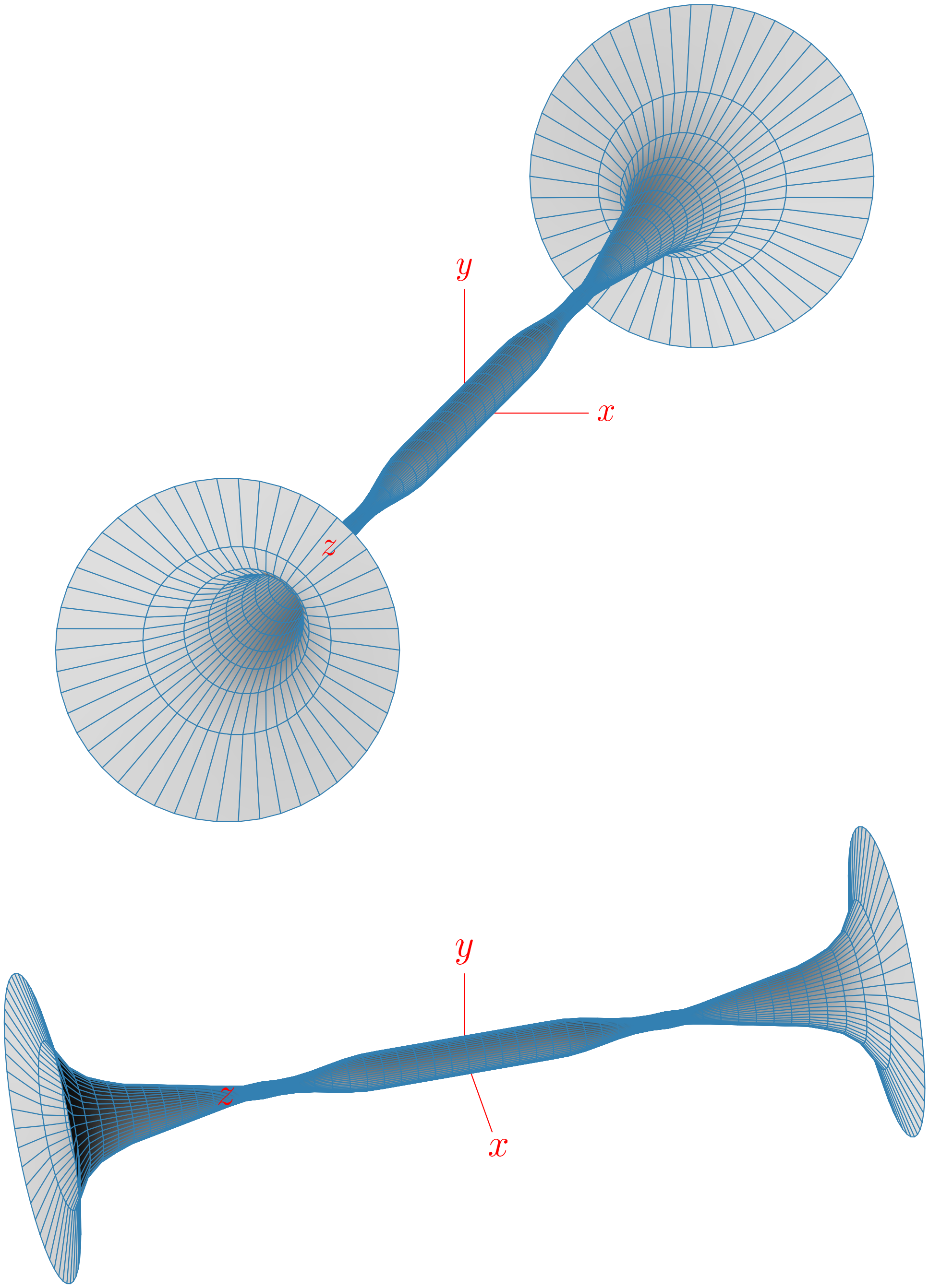

Figure 1.10: Magnetic flux surfaces in the KSTM.

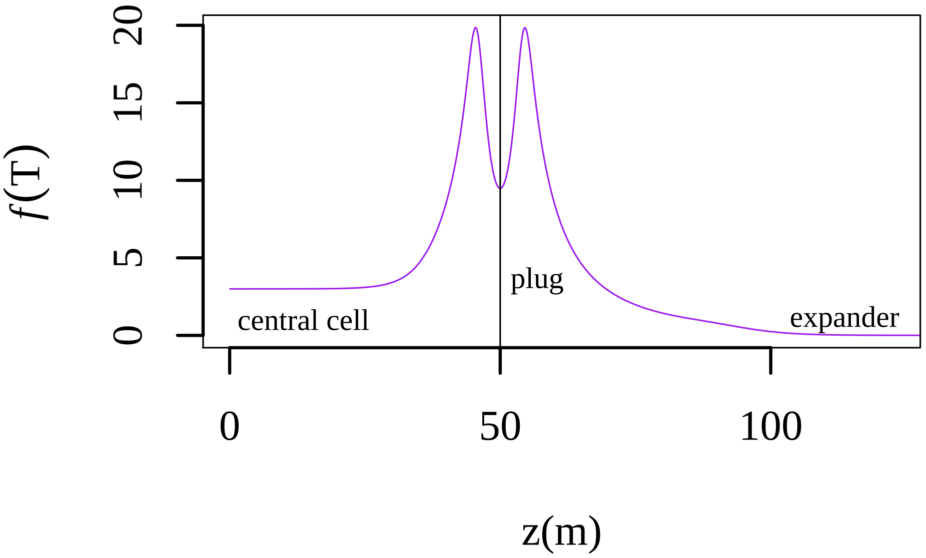

Figure 1.11: Axial magnetic field in the right half of the proposed KSTM reactor.

1.8 Motivation

In the Gas Dynamic Trap, diagnostics show that at a mirror ratio $R_M > 40$ the plasma decay is accompanied by large amplitude unstable flute modes, so called because of the resemblance of the plasma column to a fluted Greek column. For large mirror ratios there is not enough plasma in the regions of favorable curvature beyond the mirrors to stabilize the unfavorable contribution of the central cell. However, for smaller mirror ratios, these flute modes are stabilized [24]. The implication of this result is clear. The better the ends of the machine are plugged, the harder it is to establish MHD stability in

Table 1.1: Machine Parameters

Parameter	G-10 hot ion mode	KSTM reactor
a	.18 m	.3m - 1.5 m
L	6 m	30 m - 100 m
n_{c}	10^{19} m^{-3}	$1-2\cdot 10^{20}$ m^{-3}
$n_{\mathrm{p}}/n_{\mathrm{c}}$	.1	1-7
T_{e}	750 eV	50-60 keV
T_i	6.5 keV (perp) 2.5 keV (par)	15 keV
B_{cc}	.405 T	3 T
B_{plug}	3.06 T	18-20 T
R_{m}	7.6	$6-6.6$
gas type	hydrogen	D-D or D-T
volume	.61 m^3	$30-212$ m^3
surface area	6.78 m^2	$189-283$ m^2
$c_i = \phi_i/T_i$	$2.5/6.5 = 0.38$	7.8
$c_e = \phi_e/T_e$	6.25	$2.3-5$
$\phi_c = \phi_i$	2.5 keV	-
$\phi_b = \phi_e$	0.7 keV	-
$P_{ECH,cc}$	.25 MW	10 MW
$P_{ECH,plug}$	.38 MW	10 MW
$\beta = P_{cc}/(B_{cc}^2/2\mu_0)$	.48	$.3-.58$

a simple mirror trap. As tandem mirror technologies evolve, more and better means of plugging the ends of a tandem mirror are being developed. The need for theoretical study of stabilizing techniques is increasing. Primary concerns for tandem mirror stability are the $m = 1$ MHD modes and the trapped particle mode [25]. In this work we reproduce the MHD stability result of the Kinetically Stabilized Tandem Mirror reported by Post [26], and proceed to examine the stability of a trapped particle mode in the KSTM. We compare our results for the KSTM with the GAMMA-10, the largest tandem mirror in the world today.

Chapter 2

Confinement Time Scaling Laws

The radial energy-confinement time, τ_E, measures how well energetic particles are confined in the radial direction in a tandem mirror. It is defined as the characteristic time in which 1/e of a system's energy is lost to its surroundings. A comparison between the radial energy-confinement time and the axial energy-confinement time $\tau_{||}$ gives a concrete measure of how well the plugs of a machine prevent end-losses relative to the radial losses. This can be used as a measure of the effectiveness of design for modern tandem mirror machines such as the GAMMA-10 and KSTM.

The radial energy-confinement time also provides a concrete basis for comparison with toroidal devices. There are numerous tokamaks and stellarators running in a variety of regimes. Experimentalists have cataloged the results of each of their runs over many years in databases; from these databases, scaling laws for radial energy-confinement times have been calculated. In this chapter we discuss several scaling laws for the tandem mirror geometry derived in Pratt and Horton [27]. With these scaling laws, we predict how the energy-confinement time changes with system parameters in order to give some comparison with equivalently sized tokamaks. Tandem mirrors, especially axisymmetric tandem mirrors, are free from much of the anomalous transport that plagues toroidal devices; thus we expect the scaling laws we derive for tandem mirrors to provide a conservative estimate for machine performance.

2.1 Derivation of Tandem Mirror Radial Energy-Confinement Times

We use the thermal diffusivity as the basis for all of our scaling laws; gyro-Bohm and Bohm theory models are the standard turbulent models for confinement. For high β we use an electron thermal gradient (ETG) theory model. Our ETG model has been verified for $\beta >> m_{\mathrm{e}}/m_{\mathrm{i}}$, [28]. These thermal diffusivities are

$$\chi^{\mathrm{B}} = c^{\mathrm{B}} \frac{T_{\mathrm{e}}}{B} \tag{2.1}$$

$$\chi^{\mathrm{gB}} = c^{\mathrm{gB}} \frac{\rho_{\mathrm{s}}}{L_{Te}} \frac{T_{\mathrm{e}}}{eB} \tag{2.2}$$

$$\chi^{\mathrm{ETG}} = \frac{m_{\mathrm{e}}}{m_{\mathrm{i}}\beta} \chi^{\mathrm{gB}} = c^{\mathrm{ETG}} \frac{m_{\mathrm{e}}}{m_{\mathrm{i}}\beta} \frac{\rho_{\mathrm{s}}}{L_{Te}} \frac{T_{\mathrm{e}}}{eB}\ . \tag{2.3}$$

Here c^{B}, c^{gB}, and c^{ETG} are dimensionless constants. ρ_{s} is the sound radius

$$\rho_{\mathrm{s}} = \sqrt{\frac{T_{\mathrm{i}}(\mathrm{J})}{m_{\mathrm{i}}}} \frac{m_{\mathrm{i}}}{eB} \tag{2.4}$$

The electron temperature is T_{e}; L_{Te} is the characteristic length scale of the electron temperature.

To derive scaling laws for temperature T as a function of the steady state power $P = P_{\mathrm{in}} = P_{\mathrm{loss}} = P_{\mathrm{radial}} + P_{\mathrm{end}}$, we also employ a heat flux

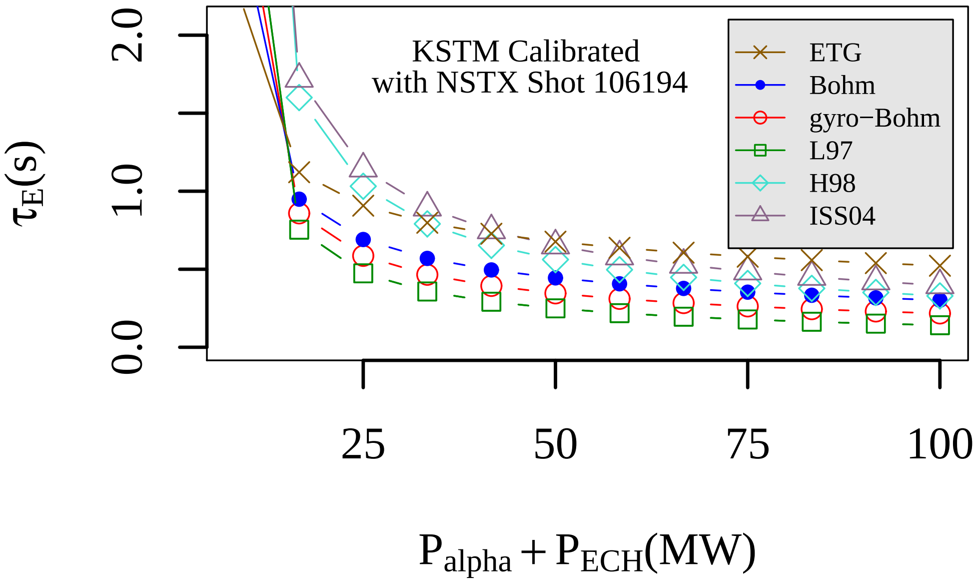

Figure 2.1: Global radial energy-confinement times, with a variety of scaling laws for the projected KSTM design. Classical drift wave scaling laws (Bohm, gyro-Bohm, and ETG) are normalized to match the empirical L97 results from NSTX at 3.3 MW of radial power loss. At low power, the ISS04 and H98 laws perform best; at high power, the ETG law matches and then exceeds these laws.

equation:

$$q = \frac{P_{\text{radial}}}{\text{Area}} = -n_{\text{e}}\chi\frac{dT_{\text{e}}}{dr} \approx n_{\text{e}}\chi T_{\text{e}}/a \ . \tag{2.5}$$

Here Area $= 2\pi a L$ is the surface area of the central cell of radius a and length L. We assume that the end loss is less than the radial loss given by the thermal heat flux; this assumption is accurate for most modern tandem mirror designs and is equivalent to defining a combination of length and mirror ratio necessary for a tandem mirror. We substitute the diffusivity formulas into this equation to obtain three scaling laws:

$$\begin{aligned}
\chi^{\mathrm{gB}} &\sim c^{\mathrm{gB}} a^{-1} B^{-2} T_{\mathrm{e}}^{3/2}, \quad \chi^{\mathrm{B}} \sim c^{\mathrm{B}} B^{-1} T_{\mathrm{e}}, \quad \chi^{\mathrm{ETG}} \sim c^{\mathrm{ETG}} a^{-1} n^{-1} T_{\mathrm{e}}^{1/2} && (2.6)\\
T_{\mathrm{e}}^{\mathrm{gB}} &\sim (\frac{aPB^2}{nL})^{2/5}, \qquad T_{\mathrm{e}}^{\mathrm{B}} \sim \sqrt{\frac{PB}{nL}}, \qquad T_{\mathrm{e}}^{\mathrm{ETG}} \sim (\frac{Pa}{L})^{2/3} . && (2.7)
\end{aligned}$$

Notice that in the diffusivity relations in eqs. (2.1) and (2.2) we have not yet given values for the dimensionless constants. This diffusivity coefficient is set so that the L97 confinement time law is matched by 3.3 MW of heating power. We choose this normalization of constants because this point of confinement is produced in the National Spherical Torus Experiment (NSTX) data [29]. Among our temperature scaling laws, the ETG model yields the most favorable temperature for fusion and the gyro-Bohm model the least favorable.

Stored plasma energy W is defined by the temperature:

$$\begin{aligned}
W &= \frac{3}{2}\int_{\mathrm{Volume}} d^3x \;\; n_{\mathrm{e}}(T_{\mathrm{e}}+T_{\mathrm{i}}) = \frac{3}{2}\, n_{\mathrm{e}}(T_{\mathrm{e}}+T_{\mathrm{i}}) \cdot \mathrm{Volume} && (2.8)\\
&= 1.5\; n(T_{\mathrm{e}}+T_{\mathrm{i}})\; \pi a^2 L \; . && (2.9)
\end{aligned}$$

Here we use the mean value theorem to define the mean temperatures T_{e} and T_{i} in eq. (2.9) for the stored plasma energy W and confinement time τ_E. At this point we define new dimensionless constants $f^{\mathrm{gB}} \sim (c^{\mathrm{gB}})^{-2/5}$, $f^{\mathrm{B}} \sim (c^{\mathrm{B}})^{-1/2}$, and $f^{\mathrm{ETG}} \sim (c^{\mathrm{ETG}})^{-2/3}$. These definitions show the sensitivity of the energy and the radial energy-confinement time to the constants we set. Using our scaling laws for temperature, eq. (2.7), we obtain scaling laws for W:

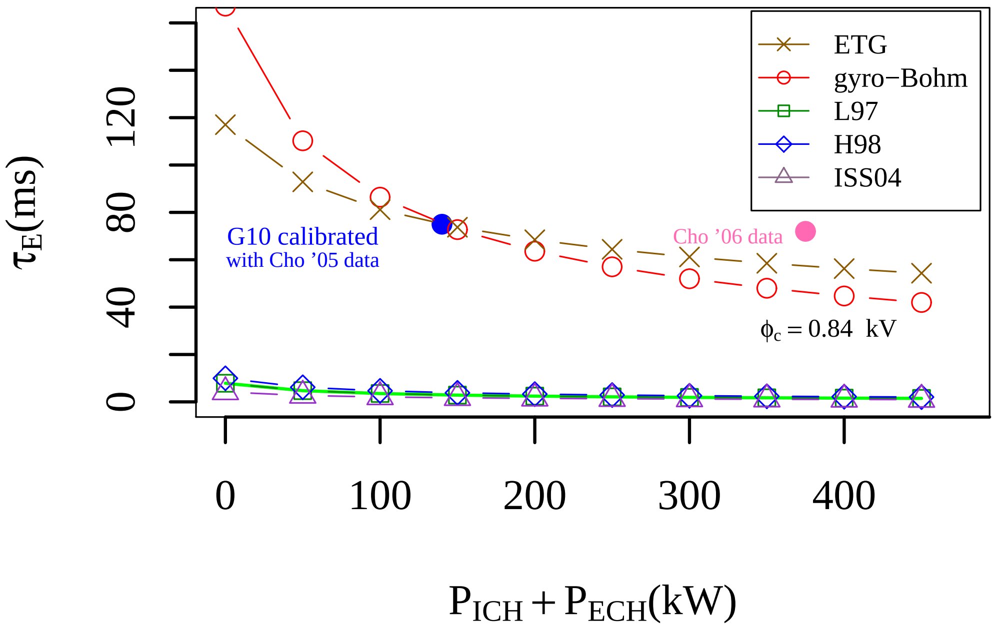

Figure 2.2: Radial energy-confinement times $\tau_{\rm E}$ with dimensionless coefficient calibrated to match the most recent reports of 75 ms in the GAMMA-10 [17]. In 2006, axial confinement times reached 100 ms and radial confinement times reached 72 ms at 380 kW of power in the GAMMA-10[30]. Depicted far below these theoretical confinement models are tokamak and stellarator confinement time scaling laws derived from large experimental databases. Energy-confinement time from the GAMMA-10 reported by Tamano in 1995 are on the order of 10 ms [20]. These older results agree fairly well with the various toroidal databases.

$$W^{\rm B} = f^{\rm B} a^2 L^{.5} n^{.5} B^{.5} P^{.5} \,, \tag{2.10}$$

$$W^{\rm gB} = f^{\rm gB} a^{2.4} L^{.6} n^{.6} B^{.8} P^{.4} \,, \tag{2.11}$$

$$W^{\rm ETG} = f^{\rm ETG} a^{2.66} L^{.33} n P^{.66} \,. \tag{2.12}$$

The total energy confinement time τ_E is defined by the power balance equation,

$$\frac{\partial W}{\partial t} = P - \frac{W}{\tau_E} \ , \tag{2.13}$$

where P is the sum of the alpha particle heating and the radio frequency wave heating powers. At steady state, this gives us expressions for the model global confinement times:

$$\begin{aligned}
\tau_E^{\mathrm{B}} &= f^{\mathrm{B}} a^2 L^{.5} n^{.5} B^{.5} P^{-.5} \ , && (2.14)\\
\tau_E^{\mathrm{gB}} &= f^{\mathrm{gB}} a^{2.4} L^{.6} n^{.6} B^{.8} P^{-.6} \ , && (2.15)\\
\tau_E^{\mathrm{ETG}} &= f^{\mathrm{ETG}} a^{2.66} L^{.33} n P^{-.33} \ . && (2.16)
\end{aligned}$$

2.1.1 Adaption of Toroidal Database Scaling Laws to Tandem Mirror Geometry

For comparison with our Bohm, gyro-Bohm, and ETG energy confinement time scaling laws (eqs. (2.14) - (2.16)), and in order to determine the dimensionless f constants, we adapt several scaling laws from toroidal databases to the tandem mirror geometry. Here we outline our procedure for the tokamak database low-mode scaling law, L97 [31]

$$\tau_E = .023 I_{\mathrm{p}}^{.96} B^{.03} R^{1.89} a^{-.06} \kappa^{.64} n^{.4} P^{-.73} \ . \tag{2.17}$$

For the KSTM we use ellipticity $\kappa = 1$, and the approximation $L = 2\pi R$. Most importantly, we need to approximate the plasma current I_{p} in terms of other parameters, since the KSTM has no parallel plasma current running through it. We make the major assumption that the radial confinement in the KSTM is comparable to the confinement in the same size tokamak with the edge safety factor of $q = 2$. For a tokamak, τ_E depends principally on the poloidal magnetic field B_p, given by the plasma current I_p in eq. (2.17). We eliminate I_p using

$$\mu_0 I_\mathrm{p} = \int B_\mathrm{p} ds = \langle B_\mathrm{p} \rangle \cdot l \tag{2.18}$$

where $l = 2\pi a$ is the length of the integration path around the poloidal cross-section, B_T is the toroidal magnetic field, and we choose the edge safety factor q such that

$$q = \frac{B_\mathrm{T} a}{\langle B_\mathrm{p} \rangle R} = 2\ . \tag{2.19}$$

We calculate the equivalent plasma current I_p, using the fact that $q(a) = 2$ to obtain

$$I_\mathrm{p} = \frac{\pi}{\mu_0} \cdot 10^{-6} \frac{Ba^2}{R} = 2.5 \frac{Ba^2}{R} \tag{2.20}$$

where I_p is 3.5 MA for the equivalent tokamak with $R/a = 4.77/1.5 = 3.2$. The L97 law in eq (2.17) summarizes confinement times from 13 tokamaks and 2000 high-quality documented discharges; our form of this law adapted to the tandem mirror is

$$\tau_{\mathrm{L97}}^{TM} = .01 B^{.99} L^{.93} a^{1.86} n^{.4} P^{-.73}\ . \tag{2.21}$$

Table 2.1: Comparison of Radial and Axial Loss Rates

Variable	GAMMA-10	KSTM
τ_E	10 (ETG) -133 (GB) ms	170 ms
$\tau_{\|\|}$	49 ms	406 s

2.2 Summary

There are four standard empirical scaling laws based on large international databases of interest to us: (*a*) the L-mode tokamak confinement time, τ_E^{L97} [31], (*b*) the H-mode tokamak confinement time, τ_E^{H98} [32], (*c*) the international stellarator database formula from 1995 τ_E^{ISS95}, and (*d*) the most recent stellarator database formula, τ_E^{ISS04} [33]. We adapted these four models to the geometry of a tandem mirror in Pratt and Horton [27]. Tokamak formulae originally involved the plasma current I_{p} but covered a limited range of safety factor $q = aB_{\mathrm{T}}/RB_{\mathrm{p}}$ values. To make the adaption to tandem mirrors, a fixed q value ($q = 2$) was chosen to obtain the tokamak empirical energy confinement as a function of machine circumference $L = 2\pi R$, minor radius a, toroidal magnetic field. The tokamak scaling formulae and stellarator scaling formulae are rendered in a comparable form in Table 2.2.

Axial confinement is determined by ion-ion Coulomb scattering time τ_{ii}, the plug mirror ratio R_{M} and the ambipolar potential, ϕ_{c}. The axial energy-confinement time

$$\tau_{||} = \exp(\phi_{\mathrm{c}}/T_{\mathrm{i}})(A_{\mathrm{p}}\frac{\phi_{\mathrm{c}}}{T_{\mathrm{i}}}\tau_{\mathrm{ii}} + R_{\mathrm{M}}L/v_{\mathrm{th,i}}) \;, \tag{2.22}$$

$$A_{\mathrm{p}} = \frac{\sqrt{\pi}}{4}\frac{R_{\mathrm{M}}}{R_{\mathrm{M}}+1}\ln(2R_{\mathrm{M}}+2) \;, \tag{2.23}$$

Table 2.2: Summary of Global Scaling laws for Radial Loss Times τ_E (s)

$\tau_{\mathrm{L97}} =$	.010	$B^{.99}$	$L^{.93}$	$a^{1.86}$	$n^{.4}$	$P^{-.73}$
$\tau_{\mathrm{H98}} =$	.067	$B^{1.08}$	$L^{.46}$	$a^{2.44}$	$n^{.41}$	$P^{-.69}$
$\tau_{\mathrm{ISS95}} =$	.080	$B^{.83}$	$L^{0.65}$	$a^{2.21}$	$n^{.51}$	$P^{-.59}$
$\tau_{\mathrm{ISS04}} =$	.103	$B^{.89}$	$L^{.6}$	$a^{2.33}$	$n^{.59}$	$P^{-.64}$
$\tau_E^{\mathrm{B}} =$	0.042	$B^{1/2}$	$L^{1/2}$	a^{2}	$n^{1/2}$	$P^{-1/2}$
$\tau_E^{\mathrm{gB}} =$	0.016	$B^{.8}$	$L^{.6}$	$a^{2.4}$	$n^{.6}$	$P^{-.6}$
$\tau_E^{\mathrm{ETG}} =$	.025	$-$	$L^{.33}$	$a^{2.66}$	n^{1}	$P^{-.33}$

is often called the Pastukhov time, because it was first derived by V.P. Pastukhov. Here A_{p} is typically called the Pastukhov parameter. The Pastukhov formula for end-loss time $\tau_{||}$, has been experimentally confirmed by Cho *et al* [17] in the GAMMA-10. The ion-ion collision time is taken to be

$$\tau_{\mathrm{ii}} \quad = \quad 1/\nu_{\mathrm{i}} = \frac{66.82\epsilon_0^2 m_{\mathrm{i}}^{1/2} T_{\mathrm{i}}^{3/2}}{n_{\mathrm{i}} e^4 \ln\Lambda_{\mathrm{i}}} \sim 5.2\mathrm{ms}\ \frac{\mathrm{T_i(keV)}^{3/2}}{\mathrm{n_{19}}\ln\Lambda_{\mathrm{i}}/20}\ . \tag{2.24}$$

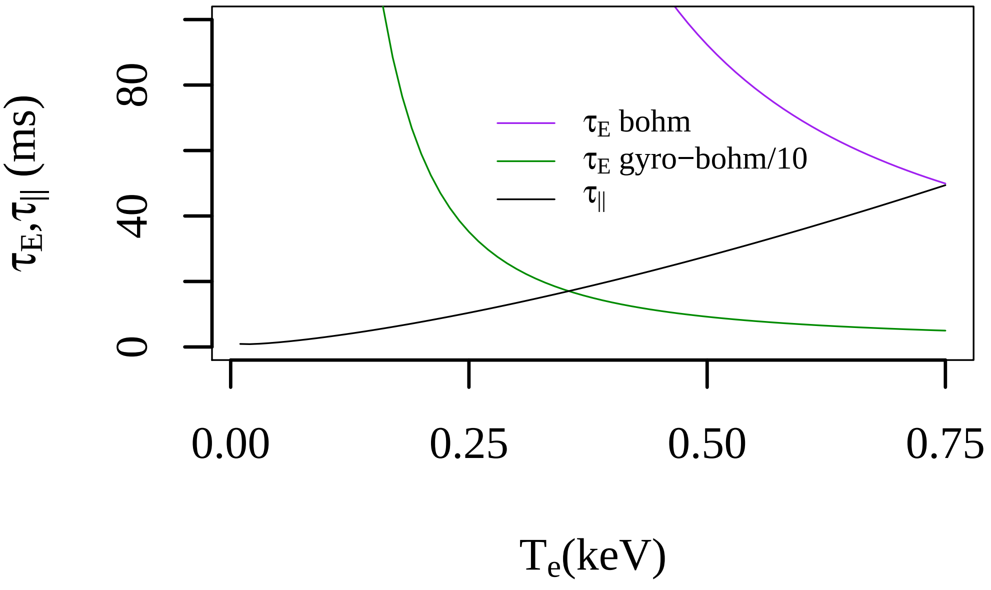

Figure 2.3: A comparison of radial energy confinement times τ_E and the axial loss time $\tau_{||}$ for various electron temperatures T_e in the GAMMA-10.

where T_i is the ion temperature, n_{19} is the densityin the central cell in units of 10^{19} and Λ_i is the Coulomb logarithm. Our calculation for the radial energy-confinement time and the Pastukhov axial confinement time are given in Table 2.1.

For the kinetically stabilized tandem mirror (KSTM) we find that the radial confinement time is significantly less than the axial confinement time; for the GAMMA-10, our predictions of the radial and axial loss times are comparable.

Chapter 3

Basics of Tandem Mirror Geometry and Stability

A tandem mirror is arranged on a cylindrical geometry. It is convenient to work in magnetic flux coordinates when working with tandem mirrors. These coordinates are similar to cylindrical coordinates in the limiting case of a circular solenoid, but more generally, magnetic flux coordinates follow the flux surface of the field when a varying magnetic field, such as a mirror field, is present (shown in Figures 1.6 and 1.10). In this chapter we work out the basics of tandem mirror geometry in magnetic flux coordinates. We explain the general case as well as the limiting case of axisymmetric fields that we employ in later chapters. This general description is necessary for comparison with GAMMA-10 results, providing necessary context for this work. A great deal of early tandem mirror literature is both difficult to obtain and incomplete, and thus a full exploration is warranted here. After this explanation of the mathematical description of tandem mirror geometry, we proceed to derive the curvature of the magnetic field for a tandem mirror, and discuss the implications of this curvature for stability.

3.1 The Flux Coordinate Metric and Tandem Mirror Formalism

In this section we choose a flux coordinate system $(x, y) \rightarrow (\psi, \theta)$ for a nonaxisymmetric geometry. This is general and can be applied to an axisymmetric system in the proper limit. In this derivation we follow the sequence of papers of Newcomb [34], Pearlstein, Kaiser, and Newcomb [35], and Kaiser and Pearlstein [36].

For some mirror systems, including the GAMMA-10 machine and the proposed kinetically stabilized tandem mirror (KSTM) reactor, the paraxial limit (also sometimes called the “long-thin” limit) is a valid approximation. Other machines, particularly the Gas Dynamic Trap (GDT) and the projected designs for a GAMMA-10 machine with cusp end-fields instead of the traditional expander fields, do not satisfy the requirements for the paraxial approximation. In the paraxial limit, the field lines are nearly parallel and nearly straight; curvatures are weak, and perpendicular components are small in comparison to the axial magnetic field. The paraxial limit is expressed through small parameters λ and ν:

$$R = \lambda L \,, \tag{3.1}$$

$$\rho = \nu R \,, \tag{3.2}$$

$$\nu << \lambda << 1 \,, \tag{3.3}$$

where R is a transverse dimension, L is an axial length, and ρ is the gyroradius [37].

It is typical in the tandem mirror literature to define two functions $f(z)$ and $g(z)$ to describe the on-axis magnetic field and the quadrupole magnetic field, respectively. An example of these fields taken from the GAMMA-10 machine is shown in Figure 3.1. When no quadrupole field is applied, *i.e.* $g(z) = 0$, a tandem mirror is called axisymmetric; the magnetic flux surfaces are circular in the $x - y$ plane. As we discussed in section 1.5, quadrupole fields are sometimes added to a tandem mirror design to deform the magnetic field lines in order to achieve a minimum-B configuration, which stabilizes the machine.

The notation of f and g is extremely useful because the full three-dimensional magnetic field can be constructed from a harmonic potential χ that is a function of these two magnetic field components. In the paraxial limit this potential is

$$\chi = \int f dz - \frac{1}{4} f'(x^2 + y^2) + \frac{1}{2} g(x^2 - y^2) , \tag{3.4}$$

$$\boldsymbol{B} = \nabla \chi . \tag{3.5}$$

And for example, for a fatter (*i.e.* not long-thin) mirror plasma that is also axisymmetric one would use:

$$\chi = \int f dz - \frac{1}{4} f' r^2 + \frac{1}{64} f^{(3)} r^4 - \frac{1}{2304} f^{(5)} r^6 \tag{3.6}$$

where $r = \sqrt{x^2 + y^2}$ is the radius. In this formula the superscripts in parentheses indicated a derivative. The fields constructed from both of these potentials satisfy the vacuum condition that $\boldsymbol{\nabla} \times \boldsymbol{B} = 0$. Kotelnikov and Rome show

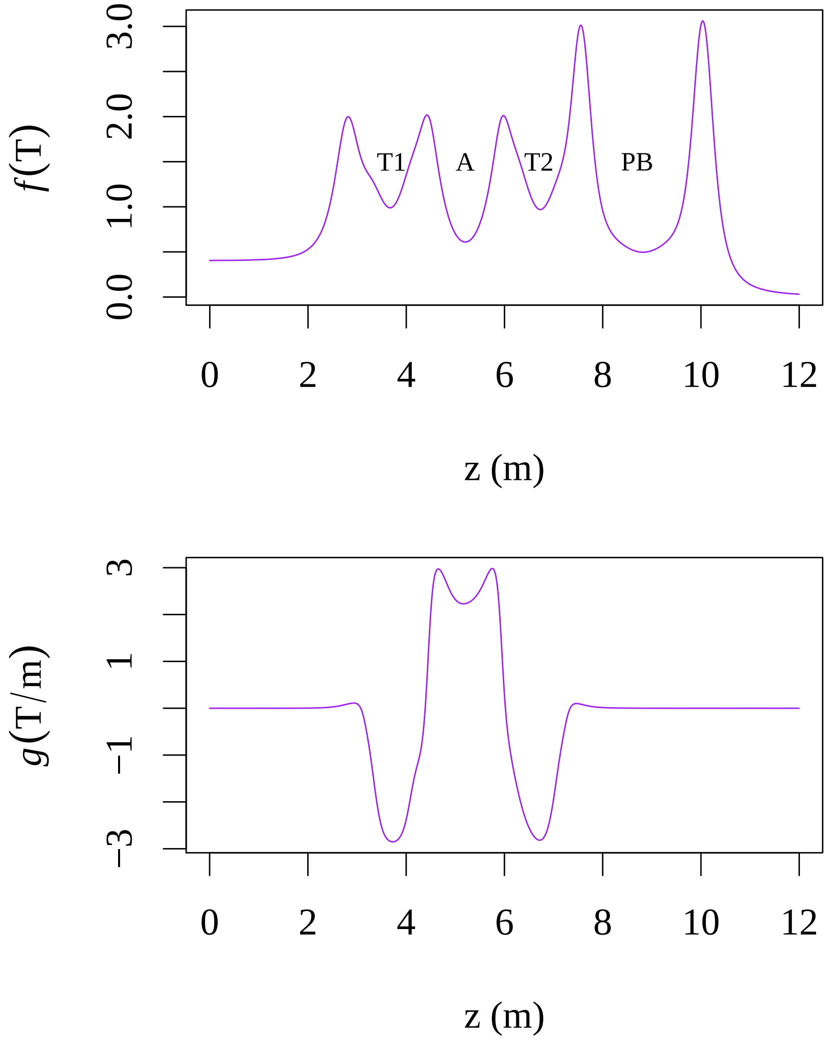

Figure 3.1: Two scalar functions are used to construct a 3 dimensional magnetic field: the axial magnetic field f (above) and the quadrupole magnetic field g (below). These graphs show the right side of the machine. f is symmetric and g can either be symmetric or antisymmetric. Data provided by personal correspondence with Katanuma [18].

how these scalar potentials are constructed in great detail [38]. The scalar potential χ must obey the Laplace equation

$$\frac{1}{r}\frac{\partial}{\partial r}\left(r\frac{\partial\chi}{\partial r}\right)+\frac{1}{r^2}\frac{\partial^2\chi}{\partial\theta^2}+\frac{\partial^2\chi}{\partial z^2}=0\ . \tag{3.7}$$

If we expand χ into a Fourier series in θ

$$\chi(r,\theta,z)=\mathrm{Re}\left[\sum_{m=0}^{\infty}\ \chi_{(m)}(r,z)\mathrm{e}^{\mathrm{i}m\theta}\right]\ . \tag{3.8}$$

Here $\chi_{(m)}$ is a Fourier amplitude, m is the mode number, and we take the real part because the imaginary part has no physical meaning. The axisymmetric part of eq. (3.8) is the $m=0$ term because all other terms in the Fourier series will depend on angle. For any mode number m the functions $\chi_{(m)}(r,z)$ in this Fourier series can be written as a power series in the radius of the plasma, r

$$\chi_{(m)}(r,z)=\sum_{n=0}^{\infty}\frac{(-1)^n m!\ r^{2n+m}}{2^{2n}\ n!\ (m+n)!}\chi^{(2n)}_{(m,0)}(z)\ . \tag{3.9}$$

Writing out the first few terms of eq. (3.9) where $m=0$, it becomes clear that we can associate $\chi^{(2n)}_{(0,0)}$ with the axial magnetic field f, in the following way:

$$\begin{aligned}\chi_{(0)}(r,z) &= \chi^{(0)}_{(0,0)}-\frac{r^2}{4}\chi^{(2)}_{(0,0)}+\frac{r^4}{64}\chi^{(4)}_{(0,0)}+... && (3.10)\\ \chi &= \left(\int_{z_0}^{z}dz\ f\right)-\frac{r^2}{4}f'(z)+\frac{r^4}{64}f'''(z)\ . && (3.11)\end{aligned}$$

A dipole perturbation of the field corresponds to $m=1$. A quadrupole expansion corresponds to $m=2$, sextupole to $m=3$ and octupole to $m=4$.

Octupole fields have been considered for tandem mirrors in the past [39], and octupole and higher distortions of the flux surfaces can be important [40]. However, for nonaxisymmetric mirrors we are most interested in the quadrupole terms, which amount to

$$\chi_{(2)} = \left[\frac{1}{2}g(z) - \frac{r^2}{24}g''(z) + ...\right] r^2 \cos(2\theta) \ . \tag{3.12}$$

Notice the dependence on θ in the quadrupole correction that was not present in the $m = 0$ axisymmetric term.

Analysis of mirrors typically begins by using flux coordinates z, θ, and ψ to describe the magnetic field. The magnetic flux coordinate ψ is a constant on any flux line and defined

$$\begin{aligned} \psi &= \int B(r,\theta,z) r dr d\theta & (3.13) \\ &= \frac{1}{2}r_0^2 f(0) = \frac{1}{2}r(z)^2 f(z) \ . & (3.14) \end{aligned}$$

For a non-axisymmetric tandem mirror, the last equality in eq. (3.14) does not hold because in a non-axisymmetric system the flux radius also depends on angle. The gradients of each of the flux coordinates are orthogonal, and so

$$B = \nabla\psi \times \nabla\theta \ . \tag{3.15}$$

The basis vectors of our coordinate system are $(x, y) \rightarrow (\nabla\psi, \nabla\theta)$. We define the coordinate space dual to our flux coordinate space $(\nabla\psi, \nabla\theta)$ to be $(\boldsymbol{u}, \boldsymbol{v})$

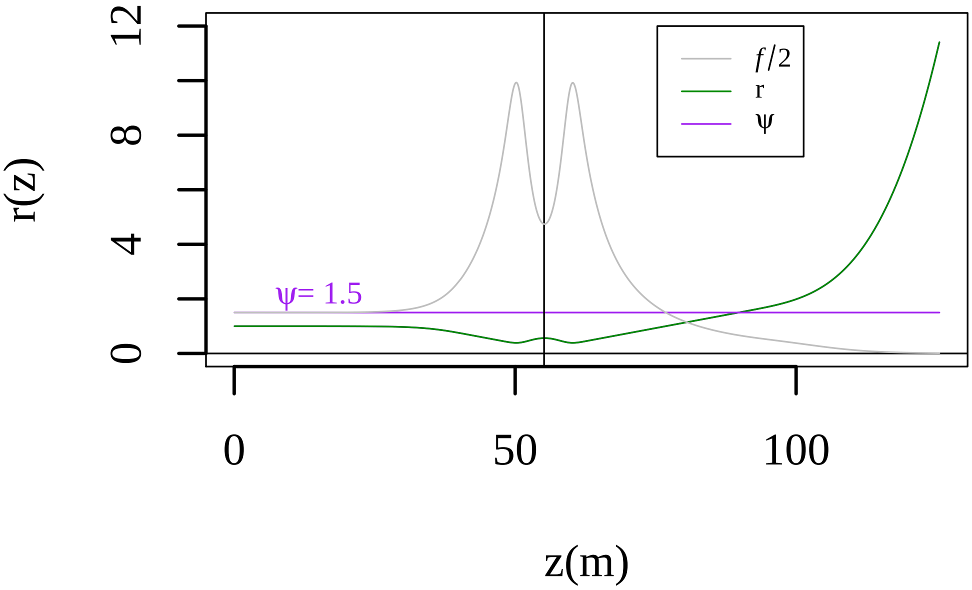

Figure 3.2: The field line radius and magnetic flux in an axisymmetric tandem mirror. In this case the flux coordinates are simple to visualize. θ and z are identical to the same coordinates in cylindrical space. The third flux coordinate, the flux itself, ψ, is a constant that dictates the relationship between radius and the magnetic field. Because ψ is constant along any field line, by specifying ψ the flux surface is determined, and thus the magnetic field line radius $r(z)$. A scaled version of f is given in the background of the figure for reference.

where the dual coordinates are

$$\boldsymbol{u} = \frac{-\hat{b} \times \nabla\theta}{B}, \tag{3.16}$$

$$\boldsymbol{v} = \frac{\hat{b} \times \nabla\psi}{B}. \tag{3.17}$$

The definition of a dual space gives us the following properties which can be directly verified:

$$\begin{aligned} \boldsymbol{u}\cdot\nabla\psi &= \boldsymbol{v}\cdot\nabla\theta = 1 & (3.18)\\ \boldsymbol{u}\cdot\nabla\theta &= \boldsymbol{v}\cdot\nabla\psi = 0 \ . & (3.19) \end{aligned}$$

In magnetic flux coordinate space, we can express the metric distance

$$d\boldsymbol{x}\cdot d\boldsymbol{x} = x_\psi^2 \ d\psi^2 + 2x_\psi x_\theta \ d\psi d\theta + x_\theta^2 \ d\theta^2 \ . \qquad (3.20)$$

The components of this metric are defined

$$\begin{aligned} x_\psi &= \boldsymbol{u}\cdot\nabla x & (3.21)\\ x_\theta &= \boldsymbol{v}\cdot\nabla x & (3.22)\\ \nabla x &= \frac{\partial x}{\partial\psi}\langle\frac{\partial\psi}{\partial x},\frac{\partial\psi}{\partial y}\rangle + \frac{\partial x}{\partial\theta}\langle\frac{\partial\theta}{\partial x},\frac{\partial\theta}{\partial y}\rangle \ . & (3.23) \end{aligned}$$

Here the brackets indicate the standard notation of a vector with components separated by commas. We then define E, F, and G to be the square-distances in flux space in order to match the notation of Newcomb [34] and Kaiser and Pearlstein [36]

$$\begin{aligned} E &= x_\psi^2 & (3.24)\\ F &= x_\psi x_\theta & (3.25)\\ G &= x_\theta^2 \ . & (3.26) \end{aligned}$$

Simply using eqs. (3.21) and (3.22) in these definitions of E, F, and G leads us to the formulas for E, F, and G in terms of the flux coordinates

$$\begin{aligned} E &= x_\psi^2 = (\boldsymbol{u}\cdot\nabla x)^2 = (\boldsymbol{u}\cdot\frac{\partial x}{\partial\psi}\nabla\psi)^2 = \left(\frac{\partial x}{\partial\psi}\right)^2 = \left(\frac{1}{\nabla\psi}\right)^2 \qquad (3.27)\\ &= \boldsymbol{u}^2 = \frac{\nabla\theta^2}{B^2}\ , \\ F &= x_\psi x_\theta = (\boldsymbol{u}\cdot\nabla x)(\boldsymbol{v}\cdot\nabla x) = \left(\boldsymbol{u}\cdot\frac{\partial x}{\partial\psi}\nabla\psi\right)\left(\boldsymbol{v}\cdot\frac{\partial x}{\partial\theta}\nabla\theta\right) \qquad (3.28)\\ &= \left(\frac{\partial x}{\partial\psi}\right)\left(\frac{\partial x}{\partial\theta}\right) = \left(\frac{1}{\nabla\psi}\right)\left(\frac{1}{\nabla\theta}\right) = \boldsymbol{u}\cdot\boldsymbol{v} = \frac{\nabla\theta\cdot\nabla\psi}{B^2}\ , \\ G &= x_\theta^2 = (\boldsymbol{v}\cdot\nabla x)^2 = \left(\boldsymbol{v}\cdot\frac{\partial x}{\partial\theta}\nabla\theta\right)^2 = \left(\frac{\partial x}{\partial\theta}\right)^2 = \left(\frac{1}{\nabla\theta}\right)^2 \qquad (3.29)\\ &= \boldsymbol{v}^2 = \frac{\nabla\psi^2}{B^2}\ . \qquad (3.30) \end{aligned}$$

We also want to include a quadrupole fanning term explicitly, and interpret E, F, and G in terms of the scalar magnetic fields f and g. In order to do this, we use the definition of the field line coordinates x and y

$$\begin{aligned} x &= x_0(\psi,\theta)e^{\gamma(z)}\sqrt{\frac{f(0)}{f(z)}}\ , \qquad (3.31)\\ y &= y_0(\psi,\theta)e^{-\gamma(z)}\sqrt{\frac{f(0)}{f(z)}}\ . \qquad (3.32) \end{aligned}$$

These equations describe field lines in the paraxial limit to leading order in θ [41]. In eqs. (3.31)-(3.32), zero and subscript zero indicate an initial point, usually understood to be inside the central cell of the machine, and thus a place where the flux surface has a circular cross-section

$$\begin{aligned} x_0(\psi,\theta) &= \sqrt{\frac{2\psi_0}{f_0}}\cos\theta\ , \qquad (3.33)\\ y_0(\psi,\theta) &= \sqrt{\frac{2\psi_0}{f_0}}\sin\theta\ . \qquad (3.34) \end{aligned}$$

We define a fanning factor γ (there is a confusion of notation in the literature for this term and so this is our own notation):

$$\gamma = \int_0^z \left(\frac{g}{f}\right) dz \tag{3.35}$$

where again, $z = 0$ is the middle of the central cell. Straightforwardly we take the derivatives (denoted by subscripts)

$$\begin{aligned}
x_\psi &= \sqrt{\frac{1}{2f_0\psi_0}}\cos\theta \ , && (3.36)\\
x_\theta &= -\sqrt{\frac{2\psi_0}{f_0}}\sin\theta \ , && (3.37)\\
y_\psi &= \sqrt{\frac{1}{2f_0\psi_0}}\sin\theta \ , && (3.38)\\
y_\theta &= \sqrt{\frac{2\psi_0}{f_0}}\cos\theta \ . && (3.39)
\end{aligned}$$

Using these derivatives we can recalculate E, F and G explicitly in terms of the fanning factor γ:

$$\begin{aligned}
E &= x_\psi^2 = \mathrm{e}^{2\gamma}\left(\frac{f_0}{f}\right)x_{0,\psi}^2 + \mathrm{e}^{-2\gamma}\left(\frac{f_0}{f}\right)y_{0,\psi}^2 && (3.40)\\
&= \frac{1}{r^2 f^2}\left(\mathrm{e}^{2\gamma}\cos^2\theta + \mathrm{e}^{-2\gamma}\sin^2\theta\right) \ ,\\
F &= x_\psi x_\theta = \mathrm{e}^{2\gamma}\left(\frac{f_0}{f}\right)x_{0,\psi}x_{0,\theta} + \mathrm{e}^{-2\gamma}\left(\frac{f_0}{f}\right)y_{0,\psi}y_{0,\theta} && (3.41)\\
&= \frac{1}{f}\left(\mathrm{e}^{2\gamma} - \mathrm{e}^{-2\gamma}\right)\cos\theta\sin\theta \ ,\\
G &= x_\theta^2 = \mathrm{e}^{2\gamma}\left(\frac{f_0}{f}\right)x_{0,\theta}^2 + \mathrm{e}^{-2\gamma}\left(\frac{f_0}{f}\right)y_{0,\theta}^2 && (3.42)\\
&= \frac{2\psi}{f}\left(\mathrm{e}^{2\gamma}\sin^2\theta + \mathrm{e}^{-2\gamma}\cos^2\theta\right) \ .
\end{aligned}$$

These formulas for E, F and G are intuitive. As $\gamma \rightarrow 0$ the angular dependence drops out of E and G, and G becomes a simple function of radius. The cross-term in the flux-space metric, F, vanishes entirely.

3.1.1 The Gradient in Flux-Coordinates

In the development of our physical eigenmode equations, we would like to evaluate the flux coordinate gradient of an eikonal function S. To take this gradient in flux coordinates, we write out the chain-rule:

$$\nabla S = \frac{\partial S}{\partial \psi}\langle\frac{\partial \psi}{\partial x}, \frac{\partial \psi}{\partial y}\rangle + \frac{\partial S}{\partial \theta}\langle\frac{\partial \theta}{\partial x}, \frac{\partial \theta}{\partial y}\rangle \ . \tag{3.43}$$

Recall that in this equation, the angled brackets indicate the standard notation of a vector with components separated by commas. The combination of eqs. (3.31)-(3.34) gives us

$$x = \sqrt{\frac{2\psi_0}{f}}\mathrm{e}^{\gamma(z)} \cos\theta \ , \tag{3.44}$$

$$y = \sqrt{\frac{2\psi_0}{f}}\mathrm{e}^{-\gamma(z)} \sin\theta \ . \tag{3.45}$$

We use the field-line eqs. (3.44) and (3.45) to eliminate ψ_0. The resulting relation $\tan\theta = (y/x)e^{2\gamma}$ allows us to obtain

$$\left.\frac{\partial \theta}{\partial x}\right|_y = -\sqrt{\frac{f}{2\psi_0}}\mathrm{e}^{-\gamma(z)} \sin\theta \ , \tag{3.46}$$

$$\left.\frac{\partial \theta}{\partial y}\right|_x = \sqrt{\frac{f}{2\psi_0}}\mathrm{e}^{\gamma(z)} \cos\theta \ . \tag{3.47}$$

Likewise eliminating θ from eqs. (3.44) and (3.45) gives us $2\psi_0 = fx^2e^{-2\gamma} + fy^2e^{2\gamma}$. The partial derivatives of ψ_0 are

$$\left.\frac{\partial\psi_0}{\partial x}\right|_y = xf\mathrm{e}^{-2\gamma} = \sqrt{2f\psi_0}\ \mathrm{e}^{-\gamma}\cos\theta\ , \tag{3.48}$$

$$\left.\frac{\partial\psi_0}{\partial y}\right|_x = yf\mathrm{e}^{2\gamma} = \sqrt{2f\psi_0}\ \mathrm{e}^{\gamma}\sin\theta\ . \tag{3.49}$$

The flux-space gradient in eq. (3.43) reduces to

$$\begin{aligned}\frac{|\nabla S|^2}{f^2} &= \frac{2\psi_0}{f}(\mathrm{e}^{-2\gamma}\cos^2\theta + \mathrm{e}^{2\gamma}\sin^2\theta)\left(\frac{\partial S}{\partial\psi}\right)^2 \\ &+ \frac{1}{2\psi_0 f}(\mathrm{e}^{-2\gamma}\sin^2\theta + \mathrm{e}^{2\gamma}\cos^2\theta)\left(\frac{\partial S}{\partial\theta}\right)^2 \\ &+ \frac{2}{f}(\mathrm{e}^{2\gamma} - \mathrm{e}^{-2\gamma})\cos\theta\sin\theta\frac{\partial S}{\partial\theta}\frac{\partial S}{\partial\psi}\ .\end{aligned} \tag{3.50}$$

In more succinct format eq. (3.50) amounts to

$$\frac{|\nabla S|^2}{f^2} = G\left(\frac{\partial S}{\partial\psi}\right)^2 + E\left(\frac{\partial S}{\partial\theta}\right)^2 + 2F\frac{\partial S}{\partial\theta}\frac{\partial S}{\partial\psi}\ . \tag{3.51}$$

As we discussed, when $g = 0$, then γ vanishes and the F cross-term drops out, along with all θ dependence of E and G. In this axisymmetric case, the gradient in eq. (3.51) is simple.

3.2 Derivation of Normal and Geodesic Curvatures

To express the curvature clearly, it is convenient to introduce dimensionless functions σ and τ [35] [42] [43], a short-hand typically employed by tandem mirror researchers to describe the ellipticity of field lines. σ and τ

can be related to the field-line coordinates x and y that we introduced in eqs. (3.44)-(3.45):

$$\begin{aligned} x(z) &= x_0\sigma = \sqrt{2\psi/f(0)}\sigma\cos\theta \ , & (3.52) \\ y(z) &= y_0\tau = \sqrt{2\psi/f(0)}\tau\sin\theta \ , & (3.53) \\ \sigma(z) &= \sqrt{\frac{f(0)}{f(z)}}\exp\left(\int_0^z dz\left(\frac{g}{f}\right)\right) \ , & (3.54) \\ \tau(z) &= \sqrt{\frac{f(0)}{f(z)}}\exp\left(-\int_0^z dz\left(\frac{g}{f}\right)\right) \ . & (3.55) \end{aligned}$$

For an initial radius $r(0)$ of a field line at point $z = 0$, these field-line equations give the change in shape of that flux surface at another point along z. This mapping is visualized in Figure 3.3, which is generated using our model of the f and g fields for the GAMMA-10. A perfectly circular flux surface at $z = 0.5$ (inside the central cell) is mapped through the eqs. (3.55) to the ellipse at $z = 7$ m. Dimensionless functions σ and τ can be related to the ellipticity $\epsilon = x(z)/y(z) = \sigma(z)\cos\theta/\tau(z)\sin\theta$ of a magnetic flux tube. The curvature vector $\boldsymbol{\kappa} = (\hat{b}\cdot\nabla)\hat{b}$ can be expressed in flux coordinates (ψ,θ,z)

$$\boldsymbol{\kappa} \ = \ \kappa_\psi\nabla\psi + \kappa_\theta\nabla\theta \ . \tag{3.56}$$

In an axisymmetric tandem mirror we can rewrite this in physical cylindrical coordinates (r,$\bar{\theta}$,z)

$$\boldsymbol{\kappa} \ = \ \kappa_\psi r_0 f_0 \hat{e}_r + \kappa_\theta\frac{1}{r_0}\hat{e}_{\bar{\theta}} \ . \tag{3.57}$$

The polar coordinate components are given by $\kappa_r = r_0 f_0 \kappa_\psi$ and $\kappa_{\bar{\theta}} = \kappa_\theta/r_0$, where κ_r and κ_θ are the covariant curvature components. The curvature $\boldsymbol{\kappa}$ has

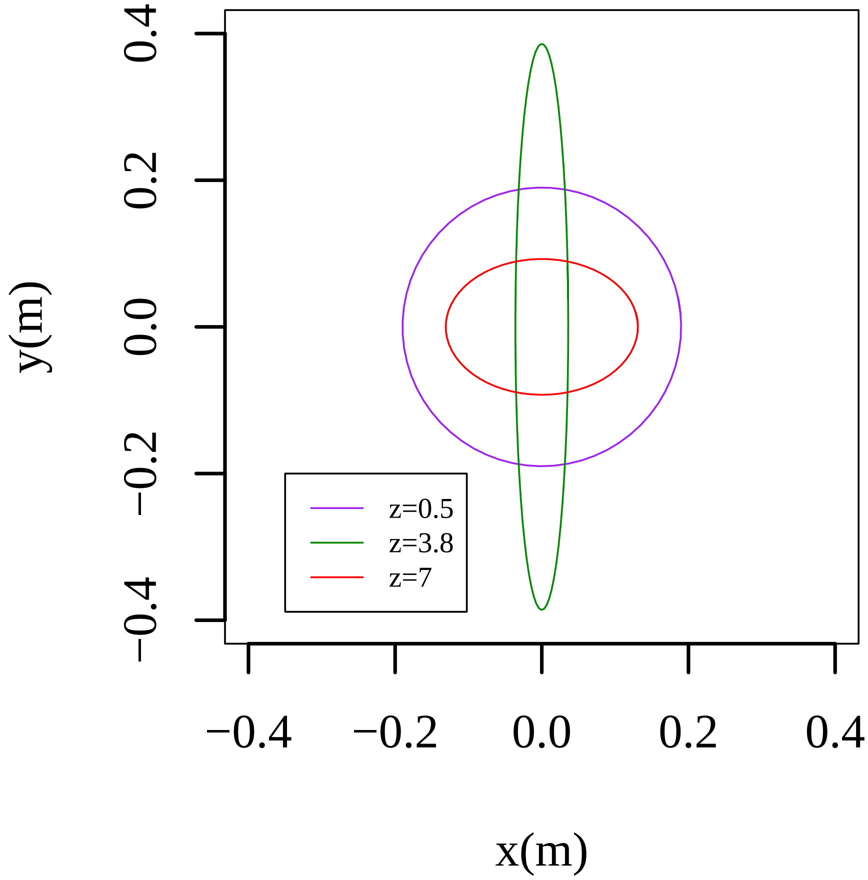

Figure 3.3: A perfectly circular field-line surface at $z = 0.5$ m is distorted into an oval shape at $z = 3.8$ m, and then stretched in the opposite direction at $z = 7$ m.

dimension 1/length. In an axisymmetric machine the geodesic curvature κ_θ is theoretically zero, but in a non-axisymmetric machine κ_θ is assumed to be less than the normal curvature, κ_ψ. The central cell region of any tandem mirror usually possesses an overall magnetic curvature κ that is extremely small or zero.

Here we follow Post [42] in deriving a form for the geodesic curvature κ_θ. This calculation is not fully explained in the literature in this area, and so here we work out every step. We begin with the definition

$$\kappa = \kappa_\psi \cdot \nabla\psi + \kappa_\theta \cdot \nabla\theta = \frac{d^2 r}{ds^2}\hat{r} \ . \tag{3.58}$$

Using the property that flux ψ is constant along any field line we know that $\psi = \psi_0 = r_0^2 f_0/2$ and so

$$\nabla\psi \cdot \kappa = r_0 f_0 \frac{d^2 r}{ds^2} = \kappa_\psi \frac{|\nabla\psi|^2}{rf} \tag{3.59}$$

$$\kappa_\psi = \frac{1}{r_0 f_0}\frac{d^2 r}{ds^2} \ . \tag{3.60}$$

The normal curvature κ_ψ has units of $\frac{1}{\mathrm{T\ m^2}}$, and the geodesic curvature κ_θ is dimensionless.

$$\nabla\theta \cdot \kappa = \nabla\theta \cdot \frac{d^2 r}{ds^2} = \kappa_\theta |\nabla\theta|^2 \tag{3.61}$$

$$\kappa_\theta = \frac{d^2 r}{ds^2}\frac{1}{|\nabla\theta|} \ . \tag{3.62}$$

In order to derive an expression for the curvature in terms of σ and τ we begin with a chain rule. The definition of κ_θ is

$$\kappa_\theta = \left.\frac{\partial^2 x}{\partial z^2}\right|_{\psi,\theta} \frac{\partial x}{\partial\theta} + \left.\frac{\partial^2 y}{\partial z^2}\right|_{\psi,\theta} \frac{\partial y}{\partial\theta} \tag{3.63}$$

If we express x and y in terms of r_0 and θ we have

$$x = \sigma(z) r_0 \cos\theta \tag{3.64}$$

$$y = \tau(z) r_0 \sin\theta \ . \tag{3.65}$$

Then taking the appropriate derivatives

$$\frac{\partial^2 x}{\partial z^2} = \sigma'' r_0 \cos\theta \ , \tag{3.66}$$

$$\frac{\partial^2 y}{\partial z^2} = \tau'' r_0 \sin\theta \ , \tag{3.67}$$

$$\frac{\partial x}{\partial \theta} = -\sigma r_0 \sin\theta \ , \tag{3.68}$$

$$\frac{\partial y}{\partial \theta} = \tau r_0 \cos\theta \ . \tag{3.69}$$

By substituting eqs. (3.66)-(3.69) into (3.63), we find

$$\kappa_\theta = \sigma'' r_0 \cos\theta(-\sigma r_0 \sin\theta) + \tau'' r_0 \sin\theta(\tau r_0 \cos\theta) \ , \tag{3.70}$$

$$\kappa_\theta = -r_0^2 \sin\theta\cos\theta(\sigma\sigma'' - \tau\tau'') \ . \tag{3.71}$$

Note that when $g = 0$, $\sigma = \tau$ and the geodesic curvature, κ_θ, vanishes uniformly. This is illustrated in Figure 3.4. An example of a system with nonzero geodesic curvature is shown in Figure 3.5.

Our derivation of the normal curvature follows the same lines as the geodesic curvature. The definition from the total curvature of the field lines gives us

$$\kappa_\psi = \left.\frac{\partial^2 x}{\partial z^2}\right|_{\psi,\theta} \frac{\partial x}{\partial \psi} + \left.\frac{\partial^2 y}{\partial z^2}\right|_{\psi,\theta} \frac{\partial y}{\partial \psi} \ . \tag{3.72}$$

Here we use the field line coordinates x and y in the form

$$x = \sqrt{\frac{2\psi}{f(z)}} \mathrm{e}^{\gamma(z)} \cos\theta \ , \tag{3.73}$$

$$y = \sqrt{\frac{2\psi}{f(z)}} \mathrm{e}^{-\gamma(z)} \sin\theta \ . \tag{3.74}$$

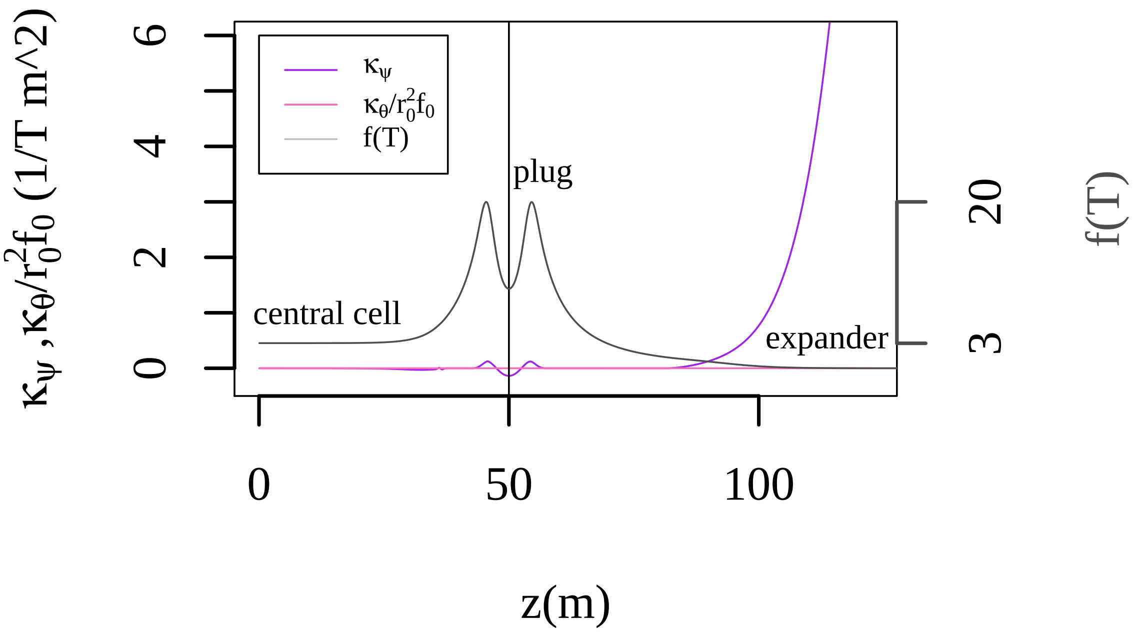

Figure 3.4: Axial magnetic field in the KSTM, along with normal and geodesic curvatures for this machine. Negative values of κ_ψ are destabilizing regions, and positive regions of κ_ψ contribute to the overall MHD stability. The relationship between curvature and stability will be worked out mathematically in section 4.7.

Thus we find the derivatives

$$\frac{\partial x}{\partial \psi} = \frac{x}{2\psi} , \tag{3.75}$$

$$\frac{\partial y}{\partial \psi} = \frac{y}{2\psi} . \tag{3.76}$$

The final formula for the normal curvature is then

$$\kappa_\psi = \sigma'' r_0 \cos\theta (\frac{1}{r_0^2 f_0} \sigma r_0 \cos\theta) + \tau'' r_0 \sin\theta (\frac{1}{r_0^2 f_0} \tau r_0 \sin\theta) \tag{3.77}$$

$$\kappa_\psi = \frac{1}{f_0} (\sigma\sigma'' \cos^2\theta + \tau\tau'' \sin^2\theta) \tag{3.78}$$

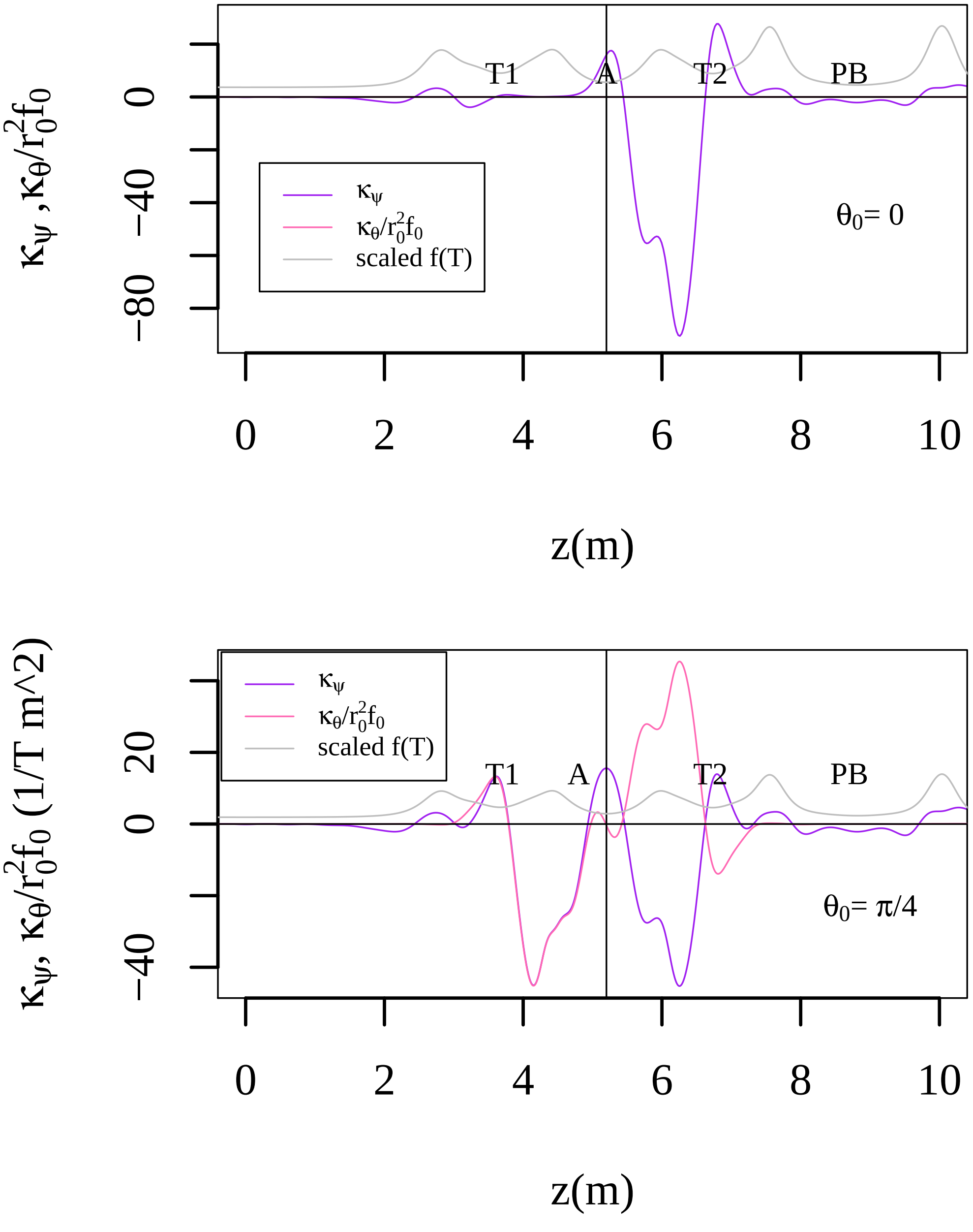

Figure 3.5: Normal and geodesic curvatures in the GAMMA-10, (above) at $\theta = 0$ and (below) at $\theta = \pi/4$. The geodesic curvature vanishes at $\theta = 0$, but is on the same order as the normal curvature for $\theta = \pi/4$. Data provided by the I. Katanuma and the GAMMA-10 team [18].

Here it is important to note that when $g = 0$, $\sigma = \tau$ and all angular dependence of the normal curvature drops out. This is why $g = 0$ is the condition for axisymmetry.

3.3 Summary

In this chapter we have explored the mathematical description of tandem mirror geometries, ending with a derivation of the normal and geodesic curvatures. The curvature is crucial to understanding the MHD stability of a tandem mirror, as we will see in the next chapter in eq. (4.50). Areas where the curvature is positive are favorable for stability, while areas of negative curvature contribute to over-all *in*stability in the machine.

Chapter 4

Ideal MHD Eigenmode Theory

In this chapter we derive an eigenmode equation for the electric potential, an equation necessary for discussion of unstable modes and their growth rates. We then examine several limiting forms of this equation that have been used in the literature. The solution of the ideal MHD eigenmode equation gives the entire frequency spectrum of modes, including those characterized by imaginary frequency that are therefore unstable. In these derivations we will use MKS units, and assume $\mu_0 = 1$ for notational simplicity. The plasma parameter β that we defined in eq. (1.8) will appear in these equations in the form

$$\beta \;=\; \frac{-2r}{f^2}\frac{\partial p}{\partial r} = \frac{-2r^2}{f}\frac{\partial p}{\partial \psi} \approx \frac{2p}{f^2}\frac{r}{L_p}\ . \tag{4.1}$$

In the last equality in eq. (4.1) the pressure gradient has been approximated using a pressure length scale L_p. We also will use the Alfvén speed $v_{\mathrm{A}}^2 = f^2/2\rho$ throughout this chapter.

4.1 Derivation of the Ballooning mode equation

The derivation of the ballooning mode equation begins with the Lagrangian

$$\delta \int_{t_0}^{t_1} dt(T - W) = 0 \tag{4.2}$$

where T is the kinetic energy and W is the potential energy of the MHD system. The ideal Ohm's Law in a magnetized plasma is $\boldsymbol{E} = -\boldsymbol{v} \times \boldsymbol{B}$. This is $\boldsymbol{j} = \sigma \boldsymbol{E}$, for $\sigma \rightarrow \infty$. In this setting $\boldsymbol{E} \rightarrow \boldsymbol{E} + \boldsymbol{v} \times \boldsymbol{B} = 0$. From this we derive a perturbation of the magnetic field $\delta B = [\nabla \times (\xi \times \boldsymbol{B})]_{\perp}$. In terms of the MHD displacement ξ of the plasma in response to this perturbation of the magnetic field, the kinetic energy is

$$T = \frac{1}{2} \int d^3x \rho |\dot{\xi}|^2 \ . \tag{4.3}$$

Here ρ is the mass density, and $\dot{\xi} = \partial \xi / \partial t$. We restrict our consideration to the most unstable perturbations, those that are incompressible and perpendicular to the magnetic field,

$$\begin{aligned} \xi \cdot \hat{b} &= 0 \ , & (4.4) \\ \nabla \cdot \xi &= 0 \ . & (4.5) \end{aligned}$$

For the incompressible mode, the potential energy W is

$$W = \frac{1}{2} \int d^3x \left[(\xi \cdot \nabla Q)(\xi \cdot \boldsymbol{\kappa}) + Q(\frac{\delta B}{B})^2 + \iota Q \hat{b} \cdot \xi \times \frac{\delta B}{B} \right] \ . \tag{4.6}$$

Here ι is the parallel current (parallel to the magnetic field $\boldsymbol{B}$), and the pressure term $Q = B^2 + p_\perp - p_{||}$. The first term in eq. (4.6) is the potential energy from the magnetic field curvature and the pressure gradient. The second term is the energy from the perturbation of the magnetic field, commonly called the line-bending energy. The third term in eq. (4.6) is known as the kink-drive term.

We define the contravariant components of the magnetic perturbation

$$\begin{aligned}
\xi^\psi &= \xi \cdot \nabla\psi = -B\frac{\partial \chi}{\partial \theta} \ , && (4.7)\\
\xi^\theta &= \xi \cdot \nabla\theta = B\frac{\partial \chi}{\partial \psi} \ , && (4.8)\\
\xi^{||} &= \xi \cdot \hat{b} = 0 \ . && (4.9)
\end{aligned}$$

We also introduce an eikonal expansion,

$$\xi = \hat{\xi}(\psi, \theta, z, t)\mathrm{e}^{\mathrm{i}S(\psi,\theta)} \ , \tag{4.10}$$

$$\chi = \hat{\chi}(\psi, \theta, z, t)\mathrm{e}^{\mathrm{i}S(\psi,\theta)} \ . \tag{4.11}$$

Here S is called the "phase" or the "eikonal" and possesses the property that $\boldsymbol{B} \cdot \nabla S \equiv 0$. The eikonal amplitude is indicated with a hat in eq. (4.11), and $\hat{\xi}$ varies on the same scale as ξ. The eikonal S is assumed to vary on a faster time scale than the amplitude. We then define the potential to be $\phi = B\hat{\chi}$. From the eikonal expansion we take simple derivatives to get

$$\begin{aligned}
\xi^\psi &= -\mathrm{i}B\hat{\chi}\frac{\partial S}{\partial \theta}\mathrm{e}^{\mathrm{i}S(\psi,\theta)} = -\mathrm{i}S_\theta\phi \ , && (4.12)\\
\xi^\theta &= \mathrm{i}B\hat{\chi}\frac{\partial S}{\partial \psi}\mathrm{e}^{\mathrm{i}S(\psi,\theta)} = \mathrm{i}S_\psi\phi \ , && (4.13)
\end{aligned}$$

where we have used a subscript to denote the partial derivative.

$$\boldsymbol{\xi} \;=\; \mathrm{i}\phi\langle -S_\theta, S_\psi, 0\rangle = \mathrm{i}\phi\frac{\boldsymbol{B}\times\nabla S}{B^2}\ . \tag{4.14}$$

Eq. (4.14) is the WKB form of the $\boldsymbol{E}\times\boldsymbol{B}$ plasma velocity from an electrostatic potential $\boldsymbol{E} = -\nabla\phi = -\mathrm{i}\phi\nabla S$.

Using the definition of the magnetic perturbation that we have just worked out, we can begin to work out the terms in eq. (4.2). Using the property of the eikonal that $\boldsymbol{B}\cdot\nabla S = 0$, the kinetic energy is

$$T \;\sim\; \frac{1}{2}\rho|\dot{\xi}|^2 = -\,\frac{1}{2}\rho\dot{\phi}^2\frac{|\nabla S|^2}{B^2}\ . \tag{4.15}$$

The first of the three potential energy terms in eq. (4.6) is

$$(\xi\cdot\nabla Q)(\xi\cdot\boldsymbol{\kappa}) \;=\; (\xi^\psi\frac{\partial Q}{\partial\psi} + \xi^\theta\frac{\partial Q}{\partial\theta})(\xi^\psi\kappa_\psi + \xi^\theta\kappa_\theta)\ .$$

Following Kaiser and Pearlstein [36], we keep only the lowest order terms in the paraxial approximation. The pressures $p_\perp$, $p_{||}$, and Q depend only on ψ and $\boldsymbol{B}$ to this order. The derivative of Q with respect to θ must vanish [36] to first order.[1] The paraxial limit has been applied to the GAMMA-10 in the past [43]. We use this limit to obtain Q dependent only on ψ. The gradient is

---

[1] Many of the older and more careful contributions to the literature call this result the isorrhopic limit. The term *isorrhopic* is an archaic technical term used in elastic theory, not to be confused with *isotropic*. Isorrhopicity amounts to the fact that elements of the plasma on the same magnetic flux line are interchangeable [44].

then simply

$$\begin{aligned}\frac{\partial Q}{\partial \psi} &= \frac{\partial}{\partial \psi}\left[2(p_\perp + B^2/2) - (p_\perp + p_{||})\right] \\ &= \frac{\partial}{\partial \psi}\left[-(p_\perp + p_{||})\right] = -2\frac{\partial p}{\partial \psi}\ .\end{aligned} \tag{4.16}$$

The total pressure $p_\perp + B^2/2$ is a function only of z in the paraxial limit, and therefore drops out of the above expression. We define $p = (p_\perp + p_{||})/2$ in simplifying this expression. Using this result we have

$$\begin{aligned}(\xi \cdot \nabla Q)(\xi \cdot \boldsymbol{\kappa}) &= -\mathrm{i}S_\theta \phi(-\frac{\partial p}{\partial \psi})\left[-\mathrm{i}S_\theta \phi \kappa_\psi + \mathrm{i}S_\psi \phi \kappa_\theta\right] \\ &= \frac{\partial p}{\partial \psi}\phi^2\left[S_\theta^2 \kappa_\psi - S_\theta S_\psi \phi \kappa_\theta\right]\ .\end{aligned} \tag{4.17}$$

The second of the three potential energy terms in eq. (4.6) is $Q(\frac{\delta B}{B})^2$, also known as the line-bending energy. We work out δB

$$\begin{aligned}\delta B &= \left[\nabla \times (\xi \times \boldsymbol{B})\right]_\perp \\ &= \left[\nabla \times (\mathrm{i}\phi\frac{\boldsymbol{B} \times \nabla S}{B^2} \times \boldsymbol{B})\right]_\perp \\ &= \left[\nabla \times \mathrm{i}\phi \nabla S\right]_\perp \\ &= \mathrm{i}\frac{\partial \phi}{\partial z}\hat{b} \times \nabla S\ .\end{aligned} \tag{4.18}$$

δB is explicitly perpendicular to the equilibrium magnetic field direction $\hat{b}$. The result is that the line-bending energy is

$$Q(\frac{\delta B}{B})^2 = \frac{Q|\delta B|^2}{B^2} = \frac{Q}{B^2}(\frac{\partial \phi}{\partial z})^2|\nabla S|^2\ . \tag{4.19}$$

As a consequence of the restrictions we have placed on δB the kink-drive energy, vanishes.

$$\begin{aligned}
\iota Q\hat{b}\cdot\xi\times\frac{\delta B}{B} &\propto \hat{b}\cdot\xi\times\delta b \\
&= \xi\cdot\delta B\times\hat{b} = \xi\cdot(\hat{b}\times\nabla S)\times\hat{b} \\
&= \xi\cdot\nabla S = (B\times\nabla S)\cdot\nabla S = 0 \ . \qquad (4.20)
\end{aligned}$$

The form of the Lagrangian density is thus

$$\mathfrak{L} = -\frac{1}{2}\rho\dot{\phi}^2\frac{|\nabla S|^2}{B^2} + \frac{\partial p}{\partial\psi}\phi^2\left[S_\theta^2\kappa_\psi - S_\theta S_\psi\phi\kappa_\theta\right] - \frac{Q}{B^2}\left(\frac{\partial\phi}{\partial z}\right)^2|\nabla S|^2 \ . \qquad (4.21)$$

The partial derivatives of the Lagrangian density are

$$\begin{aligned}
\frac{\partial\mathfrak{L}}{\partial\tilde{\phi}} &= \frac{4}{B}\frac{\partial p}{\partial\psi}\phi^2\left[S_\theta^2\kappa_\psi - S_\theta S_\psi\phi\kappa_\theta\right] && (4.22)\\
\frac{\partial\mathfrak{L}}{\partial\tilde{\phi}_t} &= -\frac{\rho}{B}\dot{\phi}\frac{|\nabla S|^2}{B^2} && (4.23)\\
\frac{\partial\mathfrak{L}}{\partial\tilde{\phi}_z} &= \frac{2Q}{B^2}\left(\frac{\partial\phi}{\partial z}\right)\frac{|\nabla S|^2}{|B|} \ . && (4.24)
\end{aligned}$$

Here the subscripts on ϕ denote a partial derivative. The standard Lagrange field equation is

$$\frac{\partial\mathfrak{L}}{\partial\tilde{\phi}} - \frac{\partial}{\partial t}\frac{\partial\mathfrak{L}}{\partial\tilde{\phi}_t} - \frac{\partial}{\partial z}\frac{\partial\mathfrak{L}}{\partial\tilde{\phi}_z} = 0 \ . \qquad (4.25)$$

This results in an eigenmode equation in MKS units

$$\begin{aligned}
&\frac{B}{|\nabla S|^2}\frac{\partial}{\partial z}\left(\frac{Q}{B^2}\frac{|\nabla S|^2}{B}\frac{\partial}{\partial z}\right)\phi \\
+ &\left[\frac{\omega^2}{v_{\mathrm{A}}^2} + 2\frac{\partial p}{\partial\psi}\left(\boldsymbol{\kappa}_\psi\frac{S_\theta^2}{|\nabla S|^2} - \boldsymbol{\kappa}_\theta\frac{S_\psi S_\theta}{|\nabla S|^2}\right)\right]\phi = 0 \ . \qquad (4.26)
\end{aligned}$$

The standard plasma $\beta \sim 2\frac{\partial p}{\partial \psi}$ multiplies the last term. The first term in the square brackets of eq. (4.26) represents the kinetic energy density; if the kinetic energy and the second derivative of ϕ (the line-bending magnetic energy) dominate this equation, the resulting modes will be shear Alfvén waves. The second term in the square brackets is the potential energy from the magnetic field curvature and the pressure gradient. The lowest eigenmode may have negative $\omega^2 = -\gamma_{\mathrm{MHD}}^2$ when the plasma β is sufficiently high.

4.2 Axisymmetric Ballooning mode equation from Kaiser and Pearlstein

Having derived eq. (4.26) we would like to reduce it to its simplest axisymmetric form, which neglects the geodesic curvature and the eikonal S. To do this we first drop the geodesic curvature that vanishes when $g = 0$. We then assume isotropic pressure $Q = B^2$ and neglect the geodesic curvature so that eq. (4.26) reduces to

$$\frac{B}{|\nabla S|^2}\frac{\partial}{\partial z}\left(\frac{|\nabla S|^2}{B}\frac{\partial}{\partial z}\right)\phi + \left[\frac{\omega^2}{v_{\mathrm{A}}^2} + 2\frac{\partial p}{\partial \psi}\boldsymbol{\kappa}_{\psi}\frac{S_{\theta}^2}{|\nabla S|^2}\right]\phi = 0 \ . \tag{4.27}$$

Recall from eq. (3.51) that in the case that geodesic curvature contributions are negligible we have

$$\frac{B}{|\nabla S|^2} \sim \text{const} \ , \tag{4.28}$$

$$\frac{S_{\theta}^2}{|\nabla S|^2} \sim r^2 \ . \tag{4.29}$$

The result is the simple axisymmetric ballooning-mode equation:

$$\frac{\partial}{\partial z}\left(\frac{\partial}{\partial z}\right)\phi+\left[\frac{\omega^2}{v_{\mathrm{A}}^2}-\left(\frac{-2r^2}{f}\frac{\partial p}{\partial \psi}\right)f\boldsymbol{\kappa}_\psi\right]\phi=0\ . \tag{4.30}$$

where we see $\beta=\frac{-2r^2}{f}\frac{\partial p}{\partial\psi}$.

4.3 Normal mode equation for the mth Azimuthal Eigenmode

Berk and Kaiser [45] use a non-eikonal normal mode equation which includes FLR terms and terms of higher order than those we have so far considered. This equation is useful for examining $m > 1$ modes in an axisymmetric system. In this section, we show that the Berk and Kaiser equation reduces to the same simple ballooning mode equation (4.30) in the $m = 1$ limit. For general mode m, the eigenmode equation from Berk and Kaiser is

$$\begin{aligned}&\frac{\partial}{\partial\psi}\left[\frac{\partial}{\partial z}\left(\psi\frac{\partial}{\partial\psi}\right)\right]\frac{\partial\phi}{\partial z} \\ -\ &\frac{m^2}{4\psi}\frac{\partial^2\phi}{\partial z^2}+\frac{\partial}{\partial\psi}\left(\frac{\rho}{f^2}\omega^2\psi\frac{\partial\phi}{\partial\psi}\right)-\frac{m^2}{4\psi}\frac{\rho}{f^2}\omega^2\phi+G\phi=0\ .\end{aligned} \tag{4.31}$$

where

$$G=-m^2\frac{\kappa_\psi}{f}\frac{\partial}{\partial\psi}\frac{1}{2}(p_\perp+p_{||})\ . \tag{4.32}$$

Note that this equation does not include geodesic curvature. For an axisymmetric system, $\psi(r,z)=\frac{r^2}{2}f(z)$ along any field line. Thus a derivative with respect to ψ is

$$\frac{\partial}{\partial\psi} = \left.\frac{\partial r}{\partial\psi}\right|_z \frac{\partial}{\partial r} + \left.\frac{\partial f}{\partial\psi}\right|_r \frac{\partial z}{\partial f}\frac{\partial}{\partial z} \tag{4.33}$$

$$= \frac{1}{rf}\frac{\partial}{\partial r} + \frac{2}{r^2 f'}\frac{\partial}{\partial z} \ . \tag{4.34}$$

Using this relation we straightforwardly work out this equation in terms of the derivative order of ϕ.

$$\begin{aligned} \frac{-4f^2}{f'^2}\frac{\partial^4\phi}{\partial z^4} &+ 8\frac{f}{f'}(\frac{ff''}{f'^2}-1)\frac{\partial^3\phi}{\partial z^3} + \frac{\partial^2\phi}{\partial z^2}\left[m^2 + \frac{\omega^2}{v_{\mathrm{A}}^2}\frac{4f^2}{f'^2} - \frac{4f^2f''^2}{f'^4} + \frac{4ff''}{f'^2} + \frac{4ff'''}{f'^3}\right] \\ &+ 4\frac{\omega^2}{v_{\mathrm{A}}^2}\left(\frac{f^2f''}{f'^3} + \frac{f}{f'}\right) + m^2\left(\frac{\omega^2}{v_{\mathrm{A}}^2} - \beta f\kappa_\psi\right)\phi = 0 \end{aligned} \tag{4.35}$$

where $\beta = \frac{-2r}{f^2}\frac{\partial p}{\partial r}$, which is consistent with our definition from the $m = 1$ eikonal equation in eq. (4.30). If we consider only the lowest order terms in ϕ and f, m^2 drops out of the equation and we are left with

$$\frac{\partial^2\phi}{\partial z^2} + \left(\frac{\omega^2}{v_{\mathrm{A}}^2} - \beta f\kappa_\psi\right)\phi = 0 \ . \tag{4.36}$$

This ballooning mode equation for an axisymmetric tandem mirror is identical to eq. (4.30).

4.4 Axisymmetric Ballooning Mode Equation

Using a non-eikonal approach, Katanuma [43] [46] independently derives a partially axisymmetric eigenmode equation that is identical to eq. (4.27). Katanuma applies this axisymmetric eigenmode to the GAMMA-10 by assuming a very strict paraxial approximation in which B_x and B_y field components are assumed to be small compared with B_z. He also only considers axial ballooning modes (corresponding to $m > 1$), and neglects motion of the plasma in the θ direction. This allows Katanuma to drop the geodesic curvature term while still considering small field ellipticities due to σ and τ. In this section, we work out the simple limit of the fully-axisymmetric case of Katanuma's equation. In this limit $\sigma(z) = \tau(z) = \sqrt{f(0)/f(z)}$ in order to compare with eqs. (4.30) and (4.36). Katanuma's equation is

$$\begin{aligned}&\frac{\partial}{\partial z}\left[\frac{\sigma^2\cos^2\theta+\tau^2\sin^2\theta}{2f(z)/f_0}Q\frac{\partial}{\partial z}\phi\right]\\+\;&\omega^2\left[\frac{\sigma^2\cos^2\theta+\tau^2\sin^2\theta}{2f(z)/f_0}\rho\right]\phi-\left(\frac{p_\perp+p_{||}}{f(z)/f_0}\right)\kappa_\psi\phi=0\;.\end{aligned}\tag{4.37}$$

We assume isotropic pressure so that $Q = f^2/f_0^2$, and the result is

$$\frac{\partial^2\phi}{\partial z^2}+\left[\frac{\omega^2}{v_{\mathrm{A}}^2}-2(\frac{2p}{f^2})f\kappa_\psi\right]\phi=0 \tag{4.38}$$

where we identify $\beta = \frac{2p}{f^2}$.

For this simple system we can directly calculate the normal curvature κ_ψ in terms of the axial magnetic field line radius in a simple, compact form

$$\begin{aligned}\kappa_\psi &= \sigma\frac{\partial^2}{\partial z^2}\sigma\cos^2\theta+\tau\frac{\partial^2}{\partial z^2}\tau\sin^2\theta &(4.39)\\&= \sqrt{\frac{f(0)}{f(z)}}\frac{\partial^2}{\partial z^2}\sqrt{\frac{f(0)}{f(z)}} &(4.40)\\&= \frac{3}{4}\frac{f'^2}{f(z)^3}-\frac{1}{2}\frac{f''}{f^2}\equiv r(z)^3r''(z)\left(\frac{f(z)}{r_0^4f_0^2}\right)\;. &(4.41)\end{aligned}$$

where $r(z) = r_0\sqrt{f_0/f}$ is the radius of the magnetic field line at constant ψ. In this simple axisymmetric case, the geodesic curvature κ_θ in the axisymmetric case is clearly zero, as we have discussed previously, since σ and τ are equal. This can be seen immediately:

$$\kappa_\theta = -2\psi/f(0)(\sigma\frac{\partial^2\sigma}{\partial z^2} - \tau\frac{\partial^2\tau}{\partial z^2})\cos\theta\sin\theta = 0 \ . \tag{4.42}$$

Eq. (4.37) can be written in terms of the field line radius. This equation has the well-recognized r^3r'' effective potential:

$$\frac{\partial^2}{\partial z^2}\phi + \left[\frac{\omega^2}{v_{\mathrm{A}}^2} - \frac{4p}{r_0^4 f_0^2}r^3r''\right]\phi \ = \ 0 \ . \tag{4.43}$$

This form is extensively used by Post in his design of the KSTM magnetic field profile. Eq. (4.43) will leads us to the MHD stability integral in section 4.7.

If we develop eq. (4.37) for non-zero quadrupole magnetic fields, we must use the full definition of σ and τ from eq. (3.55). In this case the normal curvature is

$$\begin{aligned}\kappa_\psi \ &= \ \frac{\mathrm{e}^{2\gamma}}{f}\cos^2\theta[\frac{3}{4}(\frac{f'}{f})^2 - \frac{1}{2}\frac{f''}{f} - \frac{f'\gamma'}{f} + (\gamma'^{\,2} + \gamma'')] \\ &+ \ \frac{\mathrm{e}^{-2\gamma}}{f}\sin^2\theta[\frac{3}{4}(\frac{f'}{f})^2 - \frac{1}{2}\frac{f''}{f} + \frac{f'\gamma'}{f} + (\gamma'^{\,2} - \gamma'')] \ .\end{aligned} \tag{4.44}$$

And the geodesic curvature is

$$\begin{aligned}\kappa_\theta \ = \ & -2r^2\cos\theta\sin\theta \times \\ & [\sinh 2\gamma(\frac{3}{4}(\frac{f'}{f})^2 - \frac{1}{2}\frac{f''}{f} + \gamma'^{\,2}) + \cosh 2\gamma(\gamma'' - \frac{f'\gamma'}{f})] \ .\end{aligned} \tag{4.45}$$

It is important to note here that θ and r are not functions of z, but independent variables. In order to calculate the curvature at any point, specification of the

3-dimensional point (r, θ, z) must be given. Examples of how the normal and geodesic curvatures look in the GAMMA-10 and KSTM machines are shown in Figures 3.5 and 3.4.

4.5 Kinetic theory models of MHD Modes

Our analysis in later chapters uses the ideal MHD eigenmode equation. Nevertheless, the eigenmode equation derived from kinetic theory gives important context to our discussion. When treating eigenmodes in the MHD limit, we are constrained to use the ideal MHD Ohm's Law: $\boldsymbol{E} = -\boldsymbol{v} \times \boldsymbol{B}$, a condition that demands $E_{||} = 0$. In a kinetic theory approach, we could consider parallel electric fields, $E_{||} \neq 0$, which result in drift wave oscillations with $\omega = \omega_{*e}/(1 + k_{\perp}^2 \rho_{\mathrm{s}}^2)$. The ballooning mode derived from this equation takes the form

$$B \frac{\partial}{\partial z} \frac{k_{\perp}^2(z)}{B(z)} \left[\frac{1 + k^2 \rho_s^2}{1 + k_{\perp}^2 \delta^2} \frac{\partial \phi}{\partial z} \right] + \left[\frac{\rho \omega^2 k_{\perp}^2}{B^2} + \frac{2 k_{\theta}^2 \kappa_r}{B^2} \frac{\partial p}{\partial r} \right] \phi = 0 \tag{4.46}$$

In this equation ρ_s is the sound radius and δ is the electron skin depth (or inertial length). The numerator in the fraction $(1 + k^2 \rho_s^2)/(1 + k_{\perp}^2 \delta^2)$ represents the kinetic Alfvén wave, whereas the denominator represents the inertial Alfvén wave. In our current approach we neglect these effects, expecting that they are small in the regime we consider.

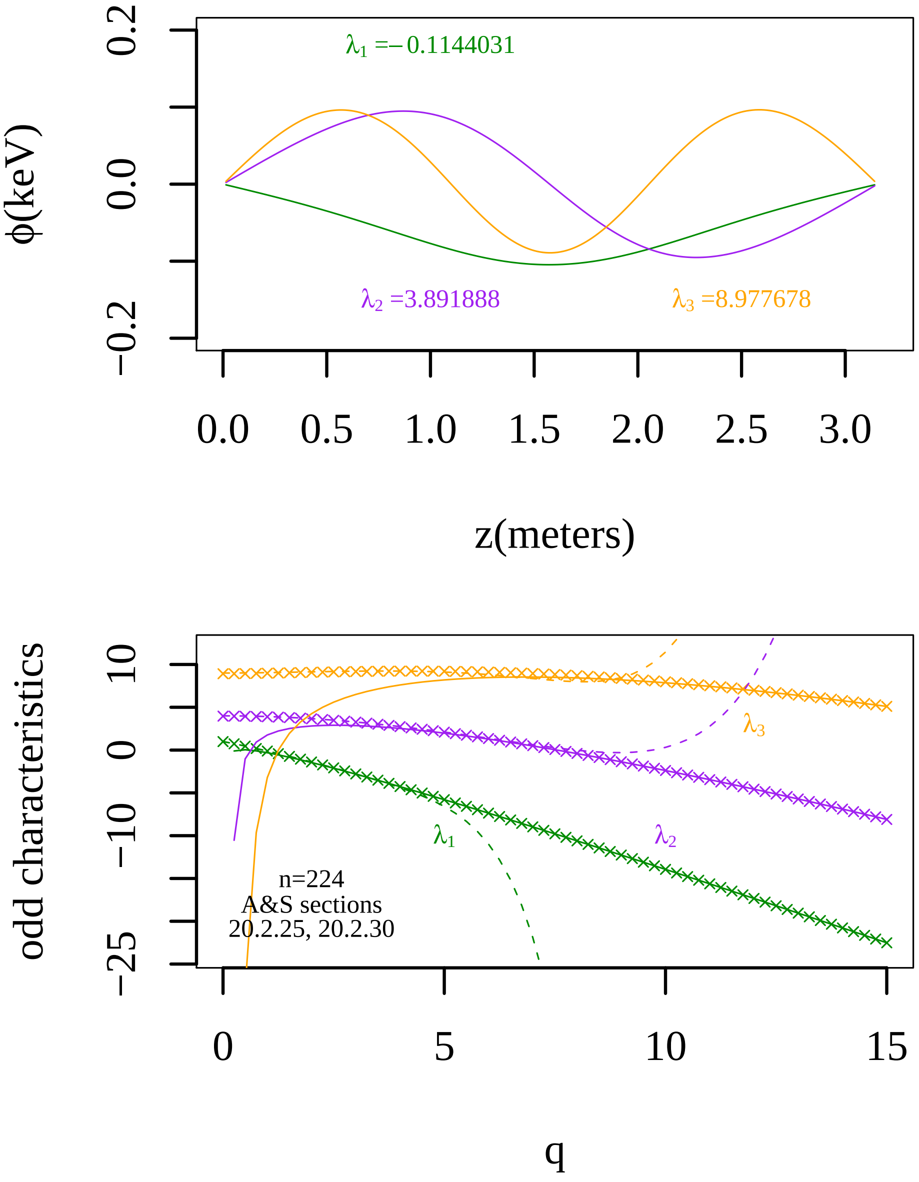

Figure 4.1: (Above) The eigenmodes that correspond to the three lowest eigenvalues of the Mathieu equation for $q = 1$. (Below) A plot of the odd eigenvalues for various Mathieu equation q values produced by our F90 code (marked by x's), and their formulas given in Abramowitz and Stegun [47] section 20.2.25 (the low q formula denoted by dashed lines) and 20.2.30 (the high q formula denoted by solid lines).

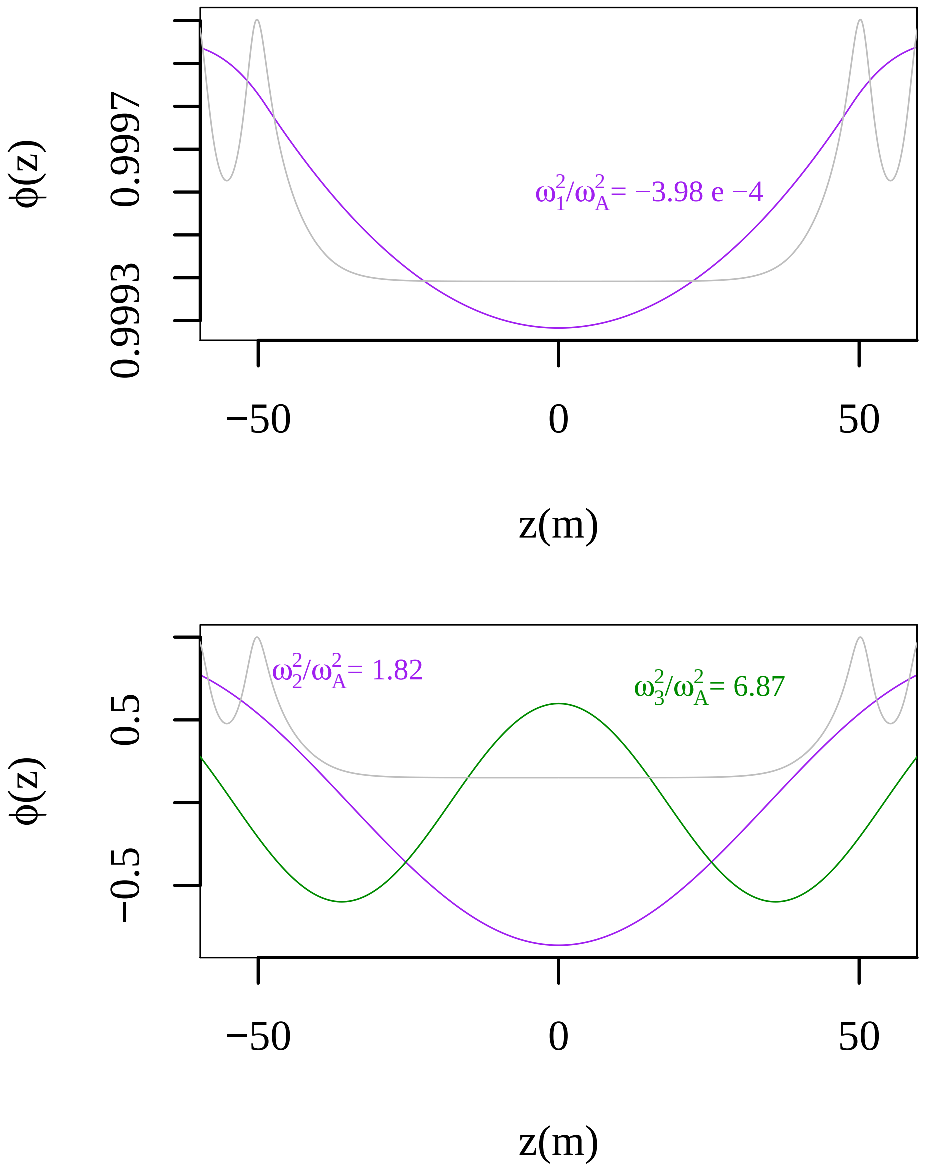

Figure 4.2: (Above) The lowest eigenmode of eq. (4.36), often called the flute mode for a tandem mirror like the KSTM before a kinetic stabilizer is applied. ω_{A}^2 is the Alfvén frequency. Since ω^2 is negative the system is unstable. In the background a scaled version of f is given for reference. (Below) The second and third lowest eigenmodes of eq. (4.36). These modes are stable because ω^2 is positive and thus these MHD growth rates are zero.

4.6 Analysis of Eigenmodes in Tandem Mirrors

We would like to solve the $m = 1$ axisymmetric eigenmode equation, eq. (4.36), for the electric potential. We have written a Fortran 90 code to solve the discrete form of the eigenmode equations, using a NAG library routine (F02GJF). A separate shooting code that solves the identical equation allows us to compare results.

We investigate a classical eigenvalue problem, the Mathieu equation, to verify that our code gives correct results. The Mathieu equation is

$$\frac{d^2\phi}{dz^2} + (\lambda - 2q\cos(2z))\phi = 0 \tag{4.47}$$

$$\phi(N) = \phi(0) \tag{4.48}$$

where N is the right-most point in the range we consider. Using a F90 code that utilizes NAG eigen-system subroutines, we find the three lowest eigenvalues to be -0.114, 3.892, and 8.978 for $q = 1$. Absolute discrepancies between these eigenvalues and the characteristics calculated from Abromowitz and Stegun's [47] truncated, low-q, series in section 20.2.25 are 0.004, 0.025, and 0.05 respectively.

We then apply our code to the axisymmetric $m = 1$ eigenmode equation, using an optimized shape for the plug and expander regions of f supplied by Post [48]. This is the shape of the magnetic field that is projected for a KSTM reactor. No kinetic stabilizer is applied in this calculation; the implementation of a kinetic stabilizer will be described at length in Chapter 6. The resulting eigenmodes are shown in Figure 4.2. The lowest eigenmode is unstable, *i.e.* $\omega^2 < 0$ or $\mathrm{Im}[\omega] = \gamma_{\mathrm{MHD}} > 0$. It has the characteristic flat profile of a flute mode. All other $m = 1$ eigenmodes of this system are stable.

4.7 MHD Stability

The MHD stability of a system depends on the lowest frequency modes, the flute modes, being stable. In order to investigate the stability of the flute mode, we return to eq. (4.36). The axial profile of ϕ for a flute mode is flat; thus we can reasonably neglect the second derivatives of ϕ. If we do this and then integrate over all z

$$\omega^2 = \frac{\int dz\ \beta f \kappa_\psi}{2 \int dz\ f^2}\ . \tag{4.49}$$

For a flute mode to be stable, ω^2 must be positive. Using the definition of β from eq. (4.1) we find that the constraint for MHD stability is

$$\int dz\ \frac{p\kappa_\psi}{f} > 0\ . \tag{4.50}$$

For simplicity we can eliminate all positive and constant quantities. Using the formula for κ_ψ in terms of the field line radius r that we worked out in eq. (4.41), we find the result

$$\int dz\ (p_\perp + p_{||}) r(z)^3 r''(z) > 0\ . \tag{4.51}$$

This result is known as the MHD stability integral, and we will use it extensively in our investigation of the KSTM. The MHD stability integral of this form was first derived by Rosenbluth and Longmire [49] from energy considerations.

4.8 Summary

In this chapter we have derived a ballooning mode equation for electric potential using the eikonal approach eq. (4.26). In the axisymmetric limit, we confirmed that this equation matches the paraxial ballooning mode equation of Katanuma in eq. (4.37) and the normal mode equation of Berk and Kaiser in eq. (4.31). From the axisymmetric eigenmode equation we derived the condition for MHD stability eq. (4.51).

Chapter 5

Spectral Gaps in Tandem Mirrors

Spectral gaps are frequency domains where there is no propagating solution to the wave equation. Gaps arise when a wave propagates in a periodic medium. Because of the quasi-periodic nature of tandem mirror machines, we examine whether the shear Alfvén wave spectrum in tandem mirrors has spectral gaps. Spectral gaps in the Alfvén wave spectrum are significant because discrete modes in the gap are easily destabilized. In particular, energetic ions can drive Alfvén gap modes unstable, causing large losses of fast ions; when expelled from the machine they can damage vessel components [50].

Zhang, *et al.* [51] estimate an Alfvén wave frequency gap, $\Delta\omega$:

$$\begin{aligned} \Delta\omega &= M\omega_{\mathrm{Bragg}} = M\omega_{\mathrm{A}}/2 && (5.1) \\ M &= \frac{B_{\max} - B_{\min}}{B_{\max} + B_{\min}} = \frac{R_M - 1}{R_M + 1} && (5.2) \end{aligned}$$

where $\omega_{\mathrm{Bragg}} = \bar{v}_{\mathrm{A}}/2L$, $\bar{v}_{\mathrm{A}}$ is the average Alfvén velocity and L is the average length between the mirrors; ω_{A} in the infinite mirror case is simply v_{A}/L. Zhang, *et al.* [51] perform three experiments on the LArge Plasma Device (known as the LAPD, the 'A' in large is typically capitalized in order to make the clever acronym), a basic plasma physics experiment at UCLA in which the magnetic field can be modulated to form a multiple mirror-like system. They find spectral gaps with a size between $M/2 < \Delta\omega/\omega_{\mathrm{A}} < M$.

5.1 Tandem mirror formulation of the Spectral Gap Problem

The Alfvén wave equation in flux coordinates (ψ, θ, z) from Kaiser and Pearlstein [36] was derived in Chapter 4. Here we treat cases and angles where the geodesic curvature κ_θ is zero, as occurs in axisymmetric systems, and the spectral gap structure appears clearly. The axisymmetric version of eq. (4.26) is eq. (4.30), namely

$$\frac{\partial^2}{\partial z^2}\phi + \left[\frac{\omega^2}{v_{\mathrm{A}}(z)^2} - 2\beta f(z)\boldsymbol{\kappa}_\psi(z)\right]\phi = 0$$

where $\beta = 2p/f(z)^2$ and both the pressure p and the density are treated as uniform parameters. The notation of f and g for the two scalar magnetic fields is defined in Chapter 3; an example of how these fields look was given in Figure 3.1. For the LAPD we employ a sinusoidal model for f that matches the magnitude and spacing of the LAPD machine [52].

For a multiple mirror system with an infinite number of cells, the solution has a Bloch function form $\phi(z) = \exp{(\mathrm{i}kz)}\tilde{\phi}(z)$ where $\tilde{\phi}$ is periodic in z. We then solve eq. (5.3) by means of a shooting code for the eigenvalue $\omega^2/\bar{v}_{\mathrm{A}}^2$, *i.e.* we normalize by a mean Alfvén speed $\bar{v}_{\mathrm{A}}$ to preserve the z dependence in v_{A}.

In the case of a finite mirror system, we cannot use a Bloch solution.

Instead, we solve for the reflection and transmission coefficients ($r^*r = R$, $t^*t = T$, $R + T = 1$) using a model of the LAPD modulated mirror and the GAMMA-10 tandem mirror on the range $0 < z < L$.

If we consider the left cell in Figure 5.1, we define the amplitudes of the reflection coefficients $r * r = R$:

$$\phi(z) \quad = \quad \exp\left(\mathrm{i}z\omega/v_{\mathrm{A}}\right) + r\exp\left(2\mathrm{i}kL\right)\exp\left(-\mathrm{i}z\omega/v_{\mathrm{A}}\right) \ . \tag{5.3}$$

We derive

$$r \quad = \quad \frac{\mathrm{i}\omega - f(0)\phi'(0)/\phi(0)}{\mathrm{i}\omega + f(0)\phi'(0)/\phi(0)} \ . \tag{5.4}$$

If we consider the right cell in Figure 5.1, we define the amplitudes of the reflection coefficients $t * t = T$:

$$\phi(z) \quad = \quad t\ \exp\left(\mathrm{i}(z - L)\omega/v_{\mathrm{A}}\right) \ . \tag{5.5}$$

We derive

$$t \quad = \quad (1 + r)\frac{\phi(L)}{\phi(0)} \ . \tag{5.6}$$

In all of these formulas, L is the distance to the right side boundary and 0 is the left side boundary of the cell. In order to calculate the gap width from r and t we identify a peak where $r = 1$ and measure the full width at half of the maximum.

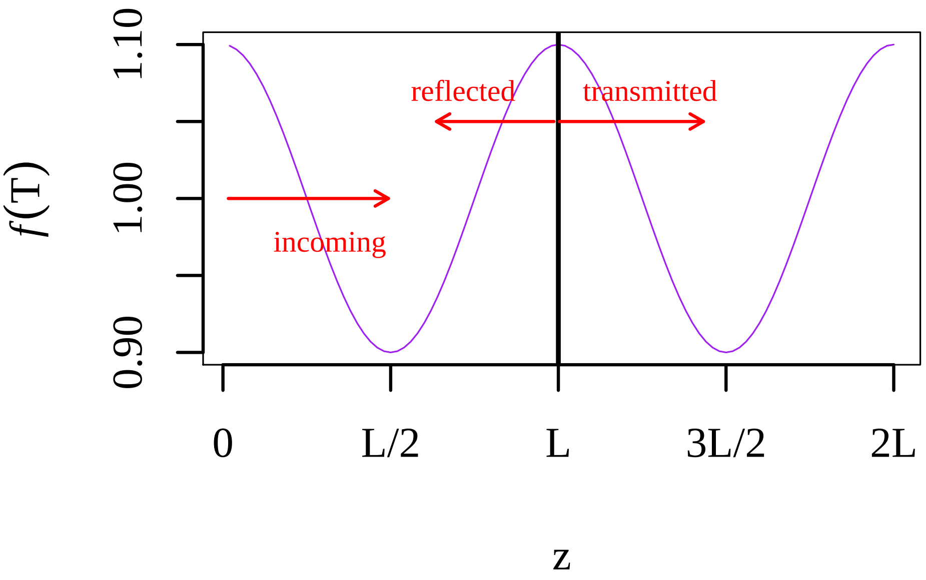

Figure 5.1: The magnetic field f in two cells of our multiple mirror configuration. Particles are either reflected or transmitted at the peaks of the mirror field at L, $2L$, etc.

5.2 Spectral Gap Results

The gap width increases with mirror depths M as demonstrated in Figure 5.2. The gap in frequency is readily visible around $(kL = 0.5, \omega/\omega_{\mathrm{A}} = 0.5)$ and also at $(kL = 0, \omega/\omega_{\mathrm{A}} = 1)$. The lines in Figure 5.2 show frequency data from a a period multiple mirror with an infinite number of cells, while the various plotted points show data from a calculation performed on a modulated mirror with a finite number of mirror cells. When there are a finite number of mirrors there is a modulation of the reflection coefficient as shown in Figures 5.3 and 5.4, with a reflection coefficient of unity at the gap. As the number of mirrors in the system increase, going from Figure 5.3 to Figure 5.4 the structure of the gap becomes closer to ideal, *i.e.* the reflection coefficient becomes unity everywhere within the gap. In order to calculate the frequency dependence on the wave number, we interpret the zeroes of the reflection coefficient as an eigenmode of the system (as the number of cells goes to infinity these eigenmodes become dense and cover the plotted curves). In Figure 5.2 finite-mirror data is plotted for $M = 0.5$ for 8 mirrors (solid dots) and 4 mirrors (triangles), and also $M = .1$ for 8 mirrors (small solid squares) and 4 mirrors (large quartered squares). The frequencies, as functions of k of a finite cell system, closely match the continuous spectrum. Reflection-coefficient results for a multiple mirror with a finite number of mirror cells show a spectral gap similar to shooting code results for an infinite number of mirror cells.

Figure 5.5 demonstrates the widening in gap width increases with an increasing dimensionless plasma pressure β. Because β is finite, normal curvature is taken into account in this calculation, but the system is assumed to be axisymmetric. Instabilities driven by the inward pressure gradient, $\beta\kappa_\psi$ exist for the smallest frequency solutions; the growth rates are plotted on the graph within the boxed region and correspond to the right y-axis.

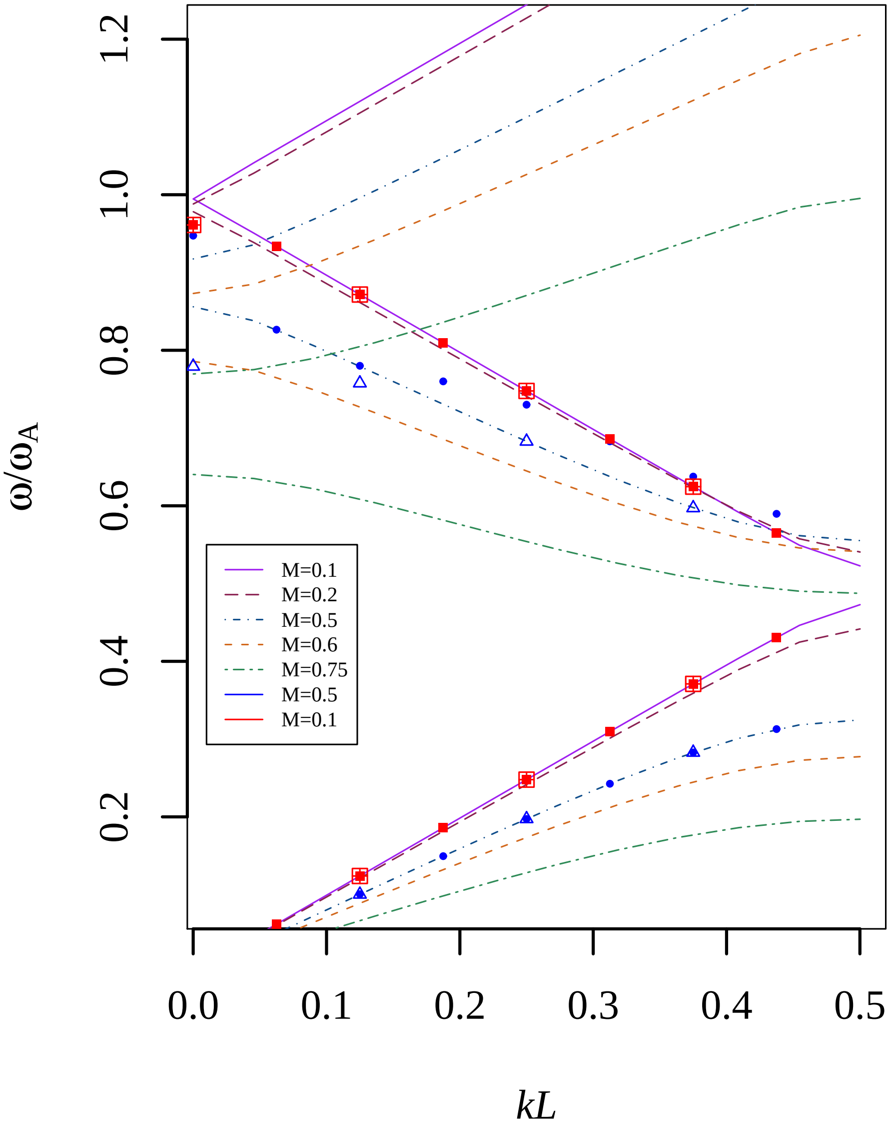

Figure 5.2: Frequency *vs.* wavenumber calculated with a shooting method, for a multiple mirror with an infinite number of cells of varying mirror depth M. The model of magnetic field used in eq. (5.3) is $f = 1 + M \sin z$ at zero plasma pressure, $\beta = 0$. The lines show frequency data from a multiple mirror with an infinite number of cells. The various plotted points show data from a reflection coefficient calculation performed on a modulated mirror with a finite number of mirror cells.

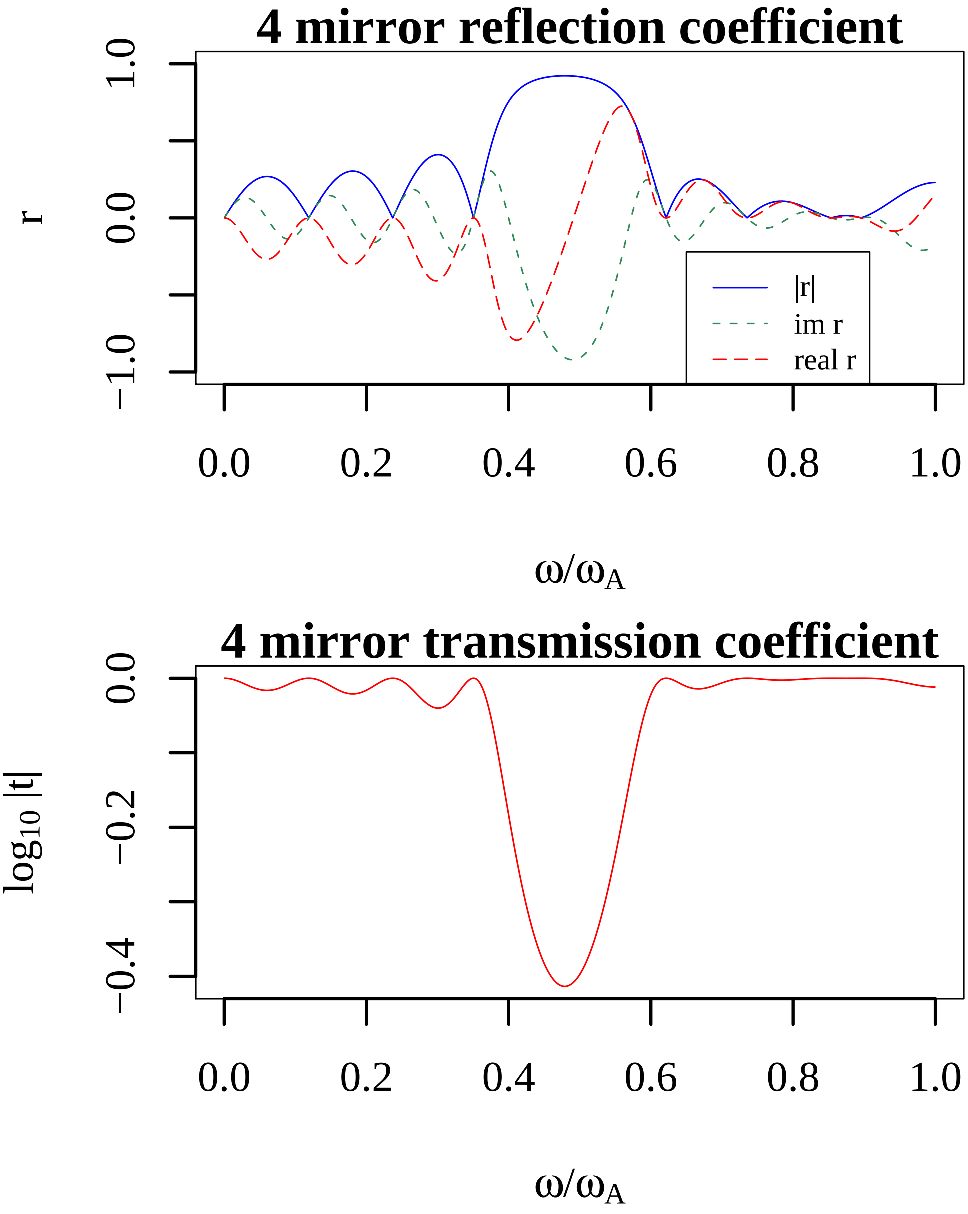

Figure 5.3: The reflection and transmission coefficients for a model of the LAPD magnetic profile. This model consists of 4 mirror cells defined by a $f = 1 + M\cos z$, where $M = .25$. We find a frequency gap at $\omega/\omega_{\mathrm{A}} = 0.5$ (where the reflection coefficient approaches 1) with a gap width of $\Delta\omega/\omega_{\mathrm{A}} = 0.208 < M$.

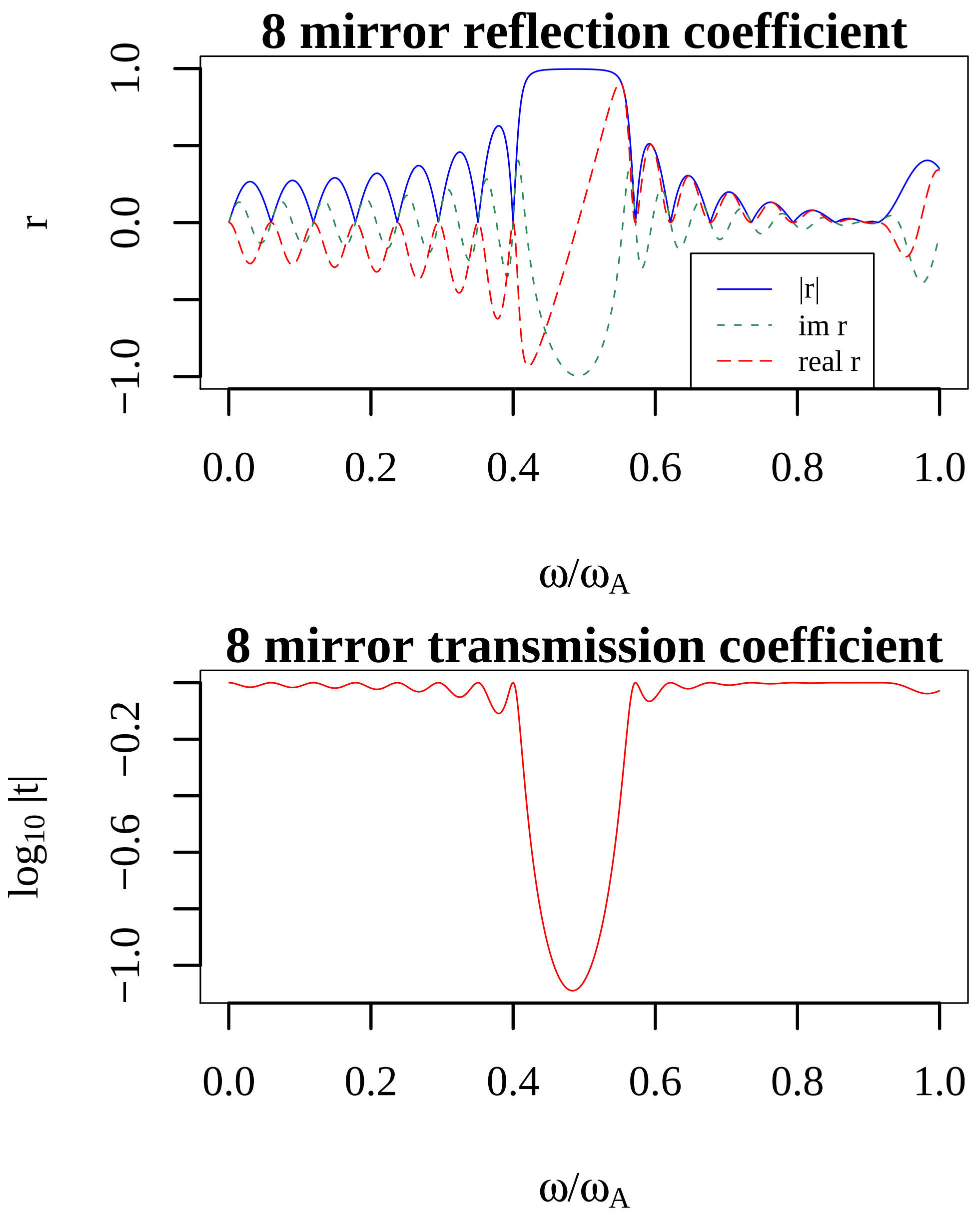

Figure 5.4: The reflection and transmission coefficients for a magnetic field similar to the LAPD, but with twice as many mirror cells. This model consists of 8 mirror cells defined by a $f = 1 + M \cos z$, where $M = .25$. We find a frequency gap of $\Delta\omega = 0.155 \approx M/2$ which approaches the result obtained from an infinite array of equally spaced mirror wells.

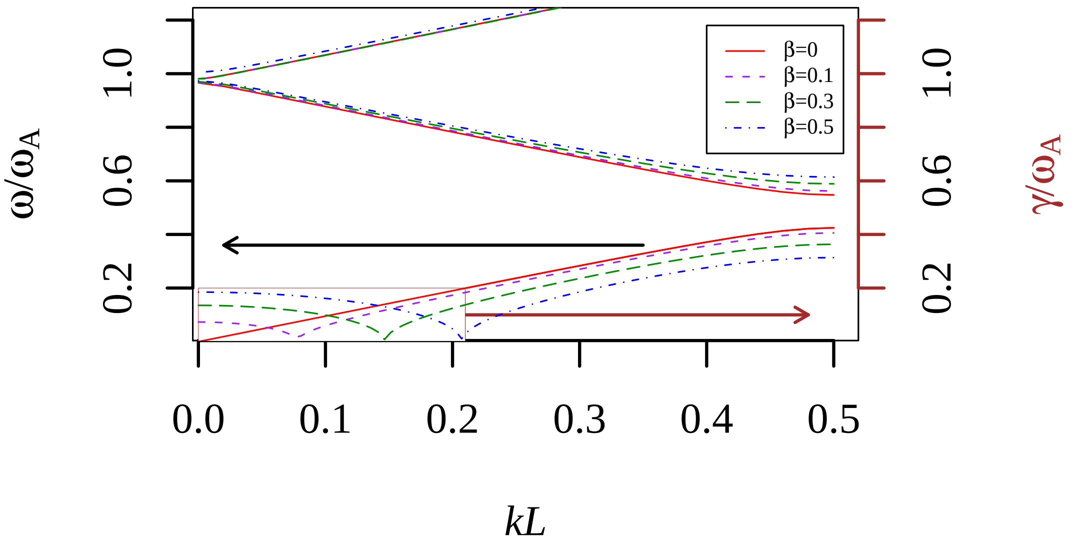

Figure 5.5: Magnitude of frequency *vs.* wavenumber calculated with a shooting method. Here we examine an infinite mirror array described by $f = 1+M \sin z$ (and setting M to a modest 0.26) while varying β. As the dimensionless plasma pressure β is increased, instability develops. The box draws attention to these growth rate magnitudes.

In the LAPD experiment three differently shaped antennas (disk, blade, and rectangular loop) located at $z = 0$ are used to launch shear Alfvén waves in a modulated mirror array [53] [54]. The magnetic fields and their time derivatives are measured by a set of ten identical B-dot probes located near the end of the mirror field at the south end of the machine [51]. From this experimental data, the LAPD team is able to extract a spectral intensity, dependent on B_θ. For waves launched at different frequencies a graph of spectral intensity *vs.* frequency can be constructed, and the frequency difference between peaks in spectral intensity is the measured gap width. In Figure 5.6 we compare our reflection-coefficient calculation for a modeled LAPD profile (star shaped data points) to the experimental data from Figure 9 of Zhang, *et al.*. Our results show gaps in a comparable range to the experimental data of the LAPD device; our results also seem to indicate a slightly shallower slope over-all.

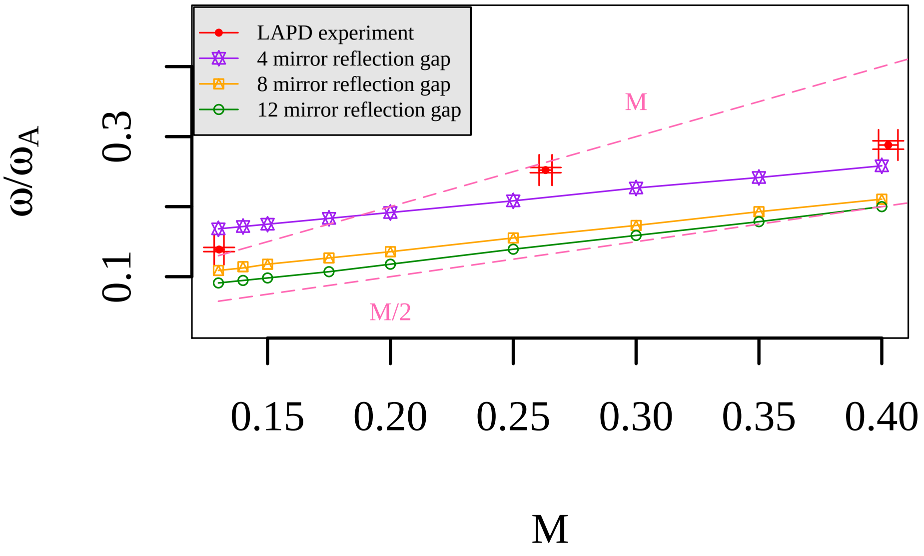

Figure 5.6: Spectral gaps calculated from the reflection coefficient for the LAPD fall in the frequency range $M/2 < \omega/\omega_{\mathrm{A}} < 2M$. This is a frequency range that covers the experimental data collected by Zhang, *et al.* (depicted as red points with error bars).

In Figure 5.6 we display additional simulation results for a model of the LAPD machine that has 8 mirrors or 12 mirrors instead of four. This data shows that as the number of mirror cells increase, the spectral gap width approaches $M/2$ for reasonably small M.

5.2.1 GAMMA-10 Tandem Mirror predictions

The GAMMA-10 machine has a larger number of mirror peaks (10 rather than 4 that the LAPD possesses) and the mirrors have a larger mirror depth M than the LAPD. The GAMMA-10 possesses 5 mirror peaks on each side of the central cell. These mirror cells are not entirely periodic, but similarly spaced and of most are of similar mirror depth, and so we consider the machine to be quasi-periodic. Thus we expect that large gap structures are possible in that machine. If present, these gaps should be closer to the result of the 4 mirror cell results in Figure 5.3. In practice, the GAMMA-10 also has finite β; here we will examine the zero β limit in order to more clearly see any spectral gap structure. For the modeled GAMMA-10, the reflection coefficient calculation was performed from the peak of the plug barrier region at approximately -10 m to the opposite peak at 10 m. The results in Figure 5.7 show that the reflection coefficient for the GAMMA-10 machine at zero β does indeed have structures similar to the gap structure we have found for the LAPD; in the GAMMA-10, the reflection coefficient approaches unity at several areas of frequency, midway between the strong transmission regions.

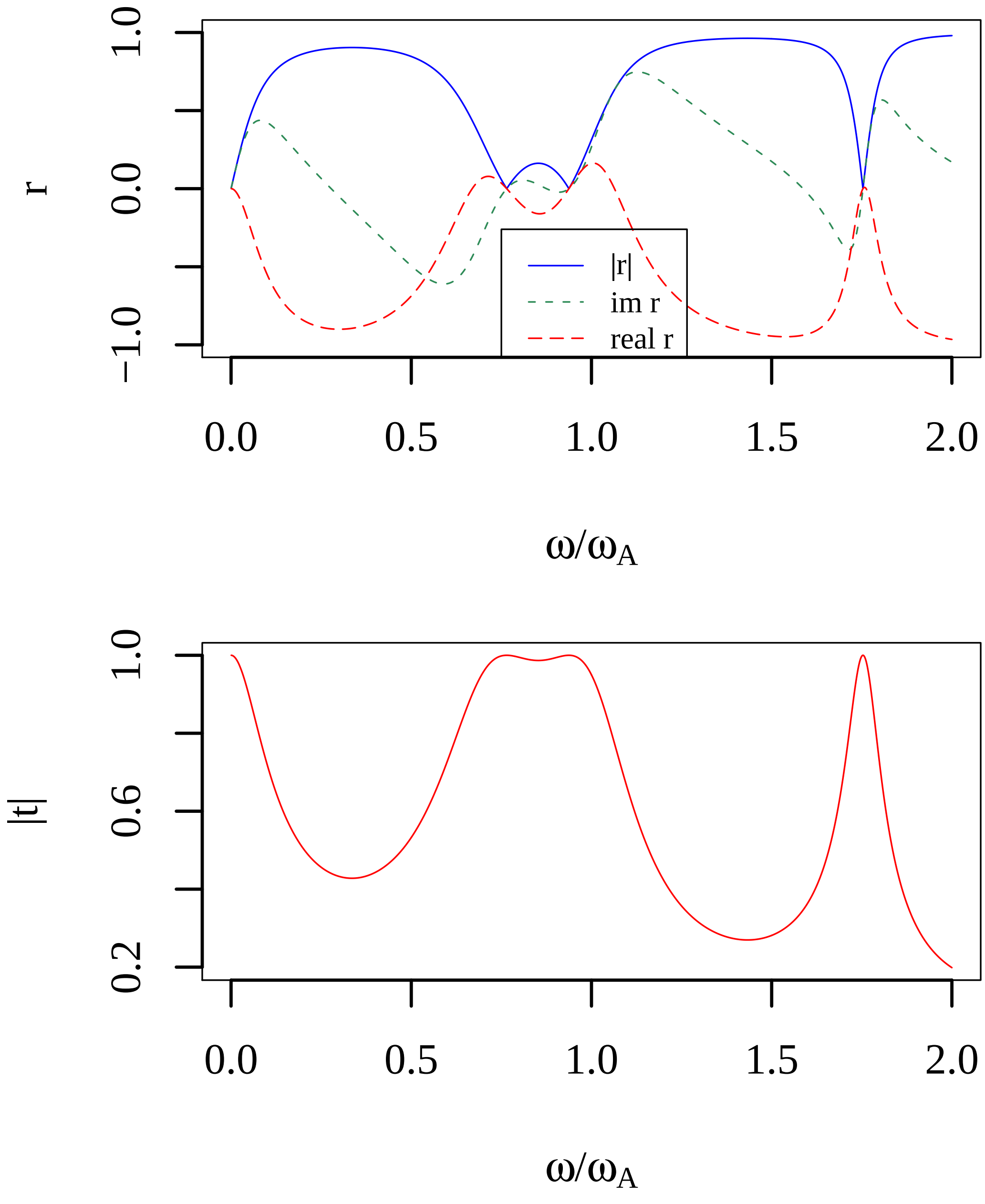

Figure 5.7: The amplitudes of the reflection and transmission coefficients, r and t for the GAMMA-10 magnetic profile in the case of vanishing plasma pressure $\beta = 0$.

5.3 Summary

Our analysis of eigenmode frequencies confirms and extends the properties of mirror gaps discussed by Zhang *et al.* [51] We find spectral gaps in the range $M/2 < \omega/\omega_{\mathrm{A}} < M$, a range that includes the experimental data collected by Zhang, *et al.*. The width of the spectral gaps clearly increases with the mirror depth M, with β, and with the number of mirror cells in the model. We also find spectral gap structure in the modeled axisymmetric GAMMA-10 studied in the limit of zero-β.

Chapter 6

Trapped Particle Modes

In this chapter we seek to answer two important questions about the kinetic stabilizer design. The first of these questions is whether the kinetic stabilizer does indeed produce MHD (magnetohydrodynamic) stability as Post *et al.* have reported [15]. We saw in section 4.7 that this is a matter of having sufficient pressure where there is favorable curvature in the expander region. The second question is whether a trapped particle mode that is excited in a kinetically stabilized tandem mirror can be stabilized *in addition* to MHD stability. A trapped particle mode is an electrostatic mode. We will introduce a trapped particle mode stability criterion [55] [56] that was derived by Berk and Lane for long mean-free-path electrons in the expander of a tandem mirror. The method of stabilization used to derive this criterion depends on charge separation. If a trapped particle mode is present then there is a perturbed potential ϕ_{tpm} in the central cell and plug regions that vanishes before the kinetic stabilizer region where favorable curvature exists; this is shown in Figure 6.1. In a tandem mirror, ions are well-trapped by an ambipolar potential in the plug, but electrons can sample the entire region inside of the kinetic stabilizer. Ions and electrons experience a different average $\boldsymbol{E} \times \boldsymbol{B}$ drift because the electric field due to the perturbed potential ϕ_{tpm} is zero for part of the bounce motion of the electrons. This causes a fluctuating current that forces the lowest frequency trapped particle mode ($m = 1$ with a flat, flute-like ϕ profile) to oscillate [57]. In the relevant dispersion relation [56] a Maxwell-Boltzman term, dependent on the electron temperature, and a charge uncovering term in the relevant dispersion relation [56] can balance the MHD term. The consequence is that if a warm body of electrons in the expander region also samples the plug region, a trapped particle mode can be stabilized.

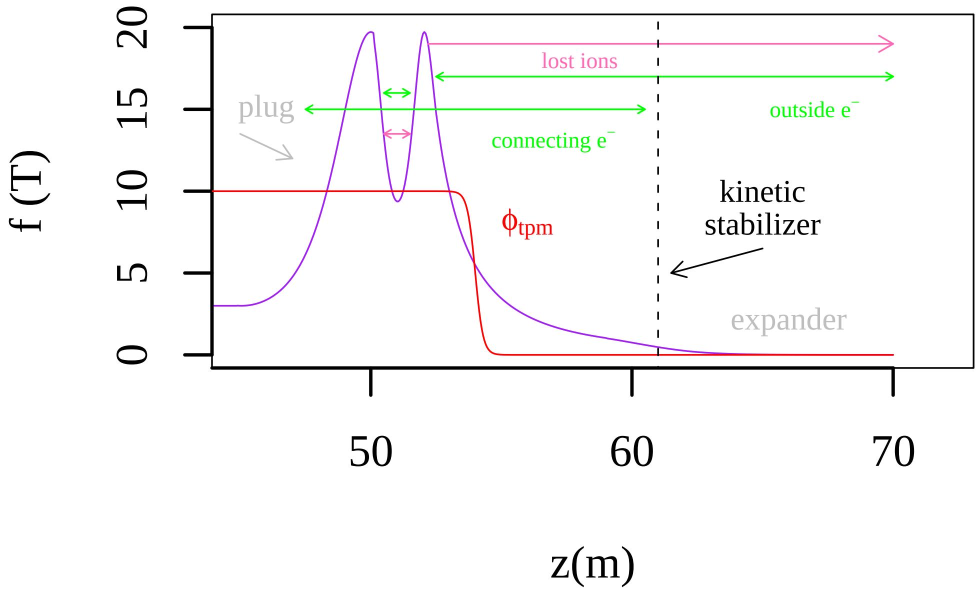

Figure 6.1: A trapped particle mode in a tandem mirror. Electrons are indicated in green; there are electrons trapped in the plug, connecting electrons that sample the plug and kinetic stabilizer regions, and electrons from outside the machine that reflect off of the ambipolar potential in the plug. Ions are indicated in pink. Most ions are trapped in the plug region by the ambipolar potential, those that are not leave the expander immediately.

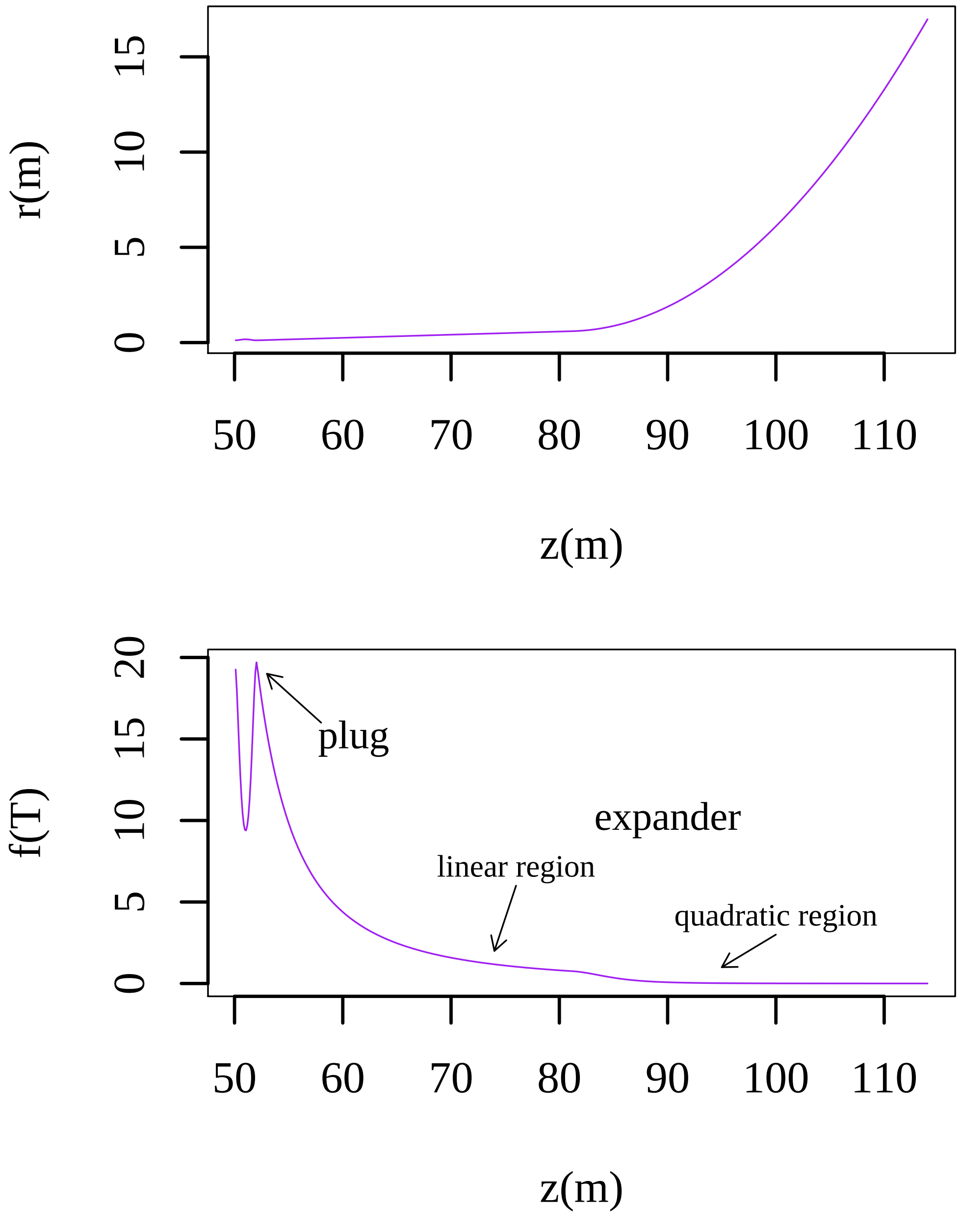

Figure 6.2: Model for the magnetic field-line radius r (above) and the axial magnetic field f (below). These particular fields are representative of the shape we are taking, but we consider a wide range of lengths for the expander region, and a wide range of magnitudes for the axial magnetic field.

6.1 Simple Model of the KSTM

Post has optimized the shape of the plug and expander regions of magnetic field on axis, $f(z)$, for MHD stability [48]. In our calculations we construct a profile for f that is similar to Post's, but which has a simple analytical form; we then optimize important quantities of the system such as magnetic field magnitude, the lengths of each region of the machine, density, and pressure. Our model for a kinetically stabilized tandem mirror machine has a cosine-shaped plug region of length $L_{\mathrm{plug}} = 2.05$ m. The axial magnetic field f is related to the magnetic field-line radius r through the condition of constant magnetic flux. Thus we can specify the desired $r(z)$ and calculate the required magnetic field from

$$f(z) = f_0 \left(\frac{r_0}{r(z)} \right)^2 \ . \tag{6.1}$$

We model the field-line radius in the plug region:

$$r(z) = r_{\mathrm{mxp}} \left[\frac{1 + r_{\mathrm{p}}}{2} + \frac{1 - r_{\mathrm{p}}}{2} \cos\left(\frac{2\pi(z - L_c)}{L_{\mathrm{plug}}} \right) \right] \ . \tag{6.2}$$

Here r_{mxp} and r_{p} are parameters that we can ultimately adjust in order to achieve stability. On one side, the plug region connects to the central cell, which has electron temperature $T_{\mathrm{e}} = 60$ keV, ion temperature $T_{\mathrm{i}} = 20$ keV, $\beta = 0.5$, and a power output of 100 MW. The plug region has an ambipolar potential $e\phi_{\mathrm{c}} = T_{\mathrm{e}} \ln n_{\mathrm{p}}/n_{\mathrm{c}}$ where n_{p} is the density in the plug and n_{c} is the density in the central cell. An ambipolar potential traps the bulk of the central cell ions with only a tail escaping.

On the other side, the plug connects to an expander; this expander consists of first a region where we take the field-line radius to rise linearly (*i.e.* $\kappa_\psi = 0$) and then a region where the field-line radius expands quadratically. We model the quadratically expanding field-line radius

$$r(z) = r_{\mathrm{mks}} \left[1 + \frac{(z - L_{\mathrm{ks}})^2}{L_{\mathrm{ks}}^2} \right] \ . \tag{6.3}$$

Here z_{ks}, r_{mks}, and L_{ks} are parameters we can adjust to achieve stability. The field-line radius throughout the machine is limited by the paraxial approximation, which constrains us to $r(z)r''(z) \leq 1/2$. Additionally, at the end of the tandem mirror both the paraxial condition and the adiabaticity condition will be satisfied by only a small margin. The adiabaticity condition takes the simple form that the curvature drift of electrons is smaller than the inertial drift

$$v_{\mathrm{c}} = \frac{v_{||}^2}{\omega_{\mathrm{c}} R_{\mathrm{c}}} << v_{||}. \tag{6.4}$$

We therefore require

$$v_{||}\kappa/\omega_c < 1/2 \ , \tag{6.5}$$

and we tailor the expander field so that the magnetic field at the wall satisfies the adiabaticity condition. An example of the field-line radius and axial magnetic field are shown in Figure 6.2.

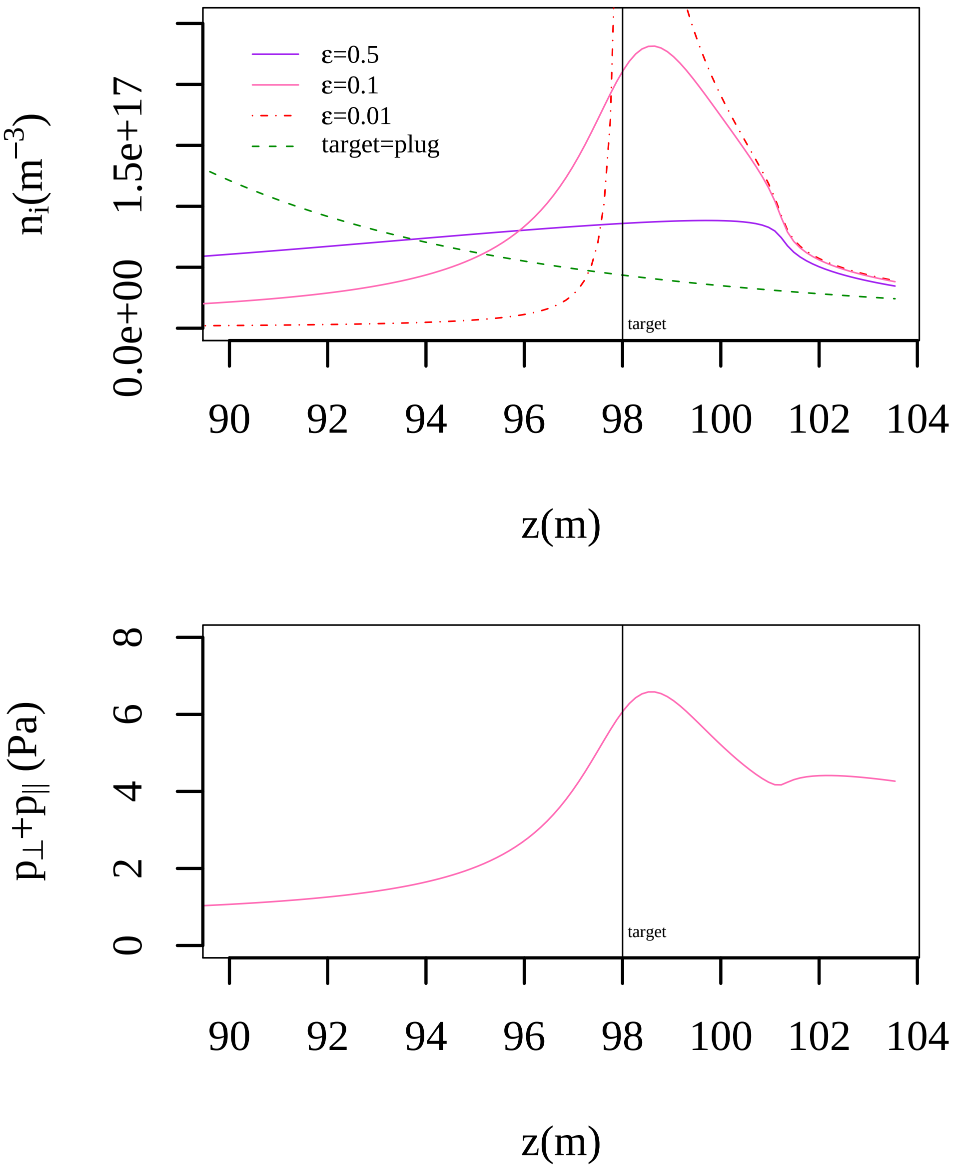

Figure 6.3: (Above) Ion density in the expander created by the kinetic stabilizer beam. The red dashed line shows density peak in the limit of small ε, the width of the μ distribution. The green dashed line shows the density profile if the target is moved into the plug region. (Below) The corresponding pressure for $\varepsilon = 0.1$. For this example machine the target is taken at $z_{\mathrm{T}} = 98$ m, $E_0 = 200$ eV and $\varphi_{\mathrm{T}}/E_0 = 0.58$, $T_{\mathrm{e}}/E_0 = 0.64$. Both density and pressure are significantly lower than density and pressures in the plug region.

6.1.1 The Kinetic Stabilizer Beam

The kinetic stabilizer consists of an ion beam injected at a small pitch angle α into the expander region of the tandem mirror. We consider the ions that make up the beam to be deuterium. The kinetic stabilizer beam is designed to reflect at a specific point in the expander region, creating a maximum in density, pressure, and electric potential. Ions in the kinetic stabilizer beam have an energy E_0 and a narrow range of magnetic moments μ as a consequence of their small pitch angles. The phase space probability density, $F(E,\mu)$

$$F(E,\mu) \quad = \quad \frac{\Gamma_{\mathrm{ks}}}{\pi}\delta(E-E_0)\frac{\varepsilon\mu_0}{(\mu-\mu_0)^2+\varepsilon^2\mu_0^2}. \tag{6.6}$$

Here we introduce the particle flux per unit magnetic flux from a single end of the tandem mirror, Γ_{ks}. Γ_{ks} is set to its maximum possible value by balancing the power necessary to sustain the beam in a single kinetic stabilizer and the fusion power produced in one half of the central cell

$$mE_0\Gamma_{\mathrm{ks}}r_0^2f_0 = \frac{3\pi r_0^2L_c(T_{\mathrm{e}}+T_{\mathrm{i}})n_c^2}{2\langle n\tau_{||}\rangle} \tag{6.7}$$

where $\tau_{||}$ is the axial energy confinement time and $\langle n\tau_{||}\rangle = 2\cdot 10^{20}$ s m^{-3} satisfies the Lawson criterion for fusion. The left hand side of eq. (6.7) is the power required to maintain a kinetic stabilizer beam, *i.e.* the energy per deuterium ion times the total particle flux $\Gamma_{\mathrm{ks}}r_0^2f_0$.

Eq. (6.6) leads to an ion density $n_{\mathrm{i}}(B)$

$$n_{\mathrm{i}}(B) \quad = \quad \int_0^\infty \mathrm{d}E \int_0^{(E_0-\varphi)/B} \frac{\mathrm{d}\mu B}{\sqrt{(E_0-\varphi)-\mu B}}F(E,\mu)\ . \tag{6.8}$$

Here $\varphi(z) = q\phi$ is the electric potential energy setup by the kinetic stabilizer beam in the expander region. We have employed a dimensionless parameter ε to control the range of magnetic moments; $2\varepsilon\mu_0$ is the full-width at half-maximum of the μ distribution. The parameters ε ultimately controls how high and how steeply the density peaks at the position where the beam is intended to reflect.

Performing the energy integral in eq. (6.8) we have a more intuitive formula for the density:

$$n_{\mathrm{i}}(B) = \frac{\sqrt{2}\Gamma_{\mathrm{ks}} B_{\mathrm{T}} \sqrt{E_0 - \varphi}}{\pi(E_0 - \varphi_{\mathrm{T}})} \varepsilon x_0^2 \int_0^1 \left(\frac{1}{\sqrt{1-x}} \right) \frac{\mathrm{d}x}{(x - x_0)^2 + \varepsilon^2 x_0^2} \ , \quad (6.9)$$

where we have defined useful dimensionless quantities x and x_0

$$x = \frac{\mu B}{E_0 - \varphi} \ , \quad (6.10)$$

$$x_0 = \frac{\mu_0 B}{E_0 - \varphi} = \left(\frac{B}{B_{\mathrm{T}}} \right) \left(\frac{E_0 - \varphi_{\mathrm{T}}}{E_0 - \varphi} \right) \ . \quad (6.11)$$

This ion density is shown in Figure 6.3. We will refer to the end of the expander region as the wall, the peak of the plug as the maximum, and the target position where the kinetic stabilizer beam reflects, as simply the target. We use the subscripts "T", "w", and "m" for quantities at the target, wall, and plug maximum points, respectively. This notation is used already in eqs. (6.9) and (6.11).

6.1.2 Pressure in the kinetic stabilizer

The kinetic stabilizer beam causes a local maximum in pressure around the target point. In magnetized plasmas, pressure is typically anisotropic with $p = p_\perp + p_{||}$. The perpendicular and parallel pressures are

$$p_\perp(B) = 2m\Gamma_{\mathrm{ks}} \int_0^\infty dE \int_0^{(E-\varphi)/B} \frac{d\mu \mu B^2}{\sqrt{2(E-\varphi-\mu B)}} F(E,\mu) \ , \tag{6.12}$$

$$p_{||}(B) = 2m\Gamma_{\mathrm{ks}} \int_0^\infty dE \int_0^{(E-\varphi)/B} d\mu B \sqrt{(E-\varphi)-\mu B}\, F(E,\mu) \ . \tag{6.13}$$

We perform these energy integrals and find

$$p_\perp(B) = \frac{\sqrt{2}}{\pi} m B_T \Gamma_{\mathrm{ks}} \frac{(E_0-\varphi)^{3/2}}{E_0-\varphi_{\mathrm{T}}} \int_0^1 \frac{dx x}{\sqrt{1-x}} \frac{\varepsilon x_0^2}{(x-x_0)^2+\varepsilon^2 x_0^2} \ , \tag{6.14}$$

$$p_{||}(B) = \frac{2\sqrt{2}}{\pi} m B_T \Gamma_{\mathrm{ks}} \frac{(E_0-\varphi)^{3/2}}{E_0-\varphi_{\mathrm{T}}} \int_0^1 \frac{dx \varepsilon x_0^2 \sqrt{1-x}}{(x-x_0)^2+\varepsilon^2 x_0^2} \ . \tag{6.15}$$

It is worth noting here that as a consequence of power balance in eq (6.7) both the density in eq. (6.9) and the pressures in eqs. (6.14)-(6.15) increase with a decreasing E_0. The pressure scales as $p \propto \Gamma_{\mathrm{ks}}\sqrt{E_0}$, and we have limited the applied power using the power balance so $\Gamma_{\mathrm{ks}} \propto 1/E_0$. Thus $p \propto 1/\sqrt{E_0}$ and as the energy of the kinetic stabilizer beam is reduced, the pressure in the expander region grows and the overall MHD stability of the system improves. The minimum magnitude of E_0 is limited only by the energy required for the particles in the beam to fully ionize. These pressures are shown in Figure 6.3 for reference parameters.

The target position for the kinetic stabilizer beam should be placed so that pressure in the positive curvature region is large. This occurs if we place the target in the linear region that precedes the positive curvature region. The target for the kinetic stabilizer beam must be carefully chosen if the electrons are to sample both the plug and the kinetic stabilizer region, and the plasmas is to be connected enough for the kinetic stabilizer to stabilize a trapped particle mode.

6.1.3 Electric potential in the kinetic stabilizer

In addition to a jump in density and pressure, the ions from the kinetic stabilizer beam set up an electric potential in the expander region. We solve for this potential using the quasi-neutral assumption $n_\mathrm{i} = n_\mathrm{e}$; in the rare case that the quasi-neutral assumption fails, we solve for the potential using the full Poisson equation.

The most common situation in a tandem mirror is that the plugs of a tandem mirror trap particles well, and that electrons in the expander are immediately lost from the ends of the machine. These expander electrons therefore have a long mean-free-path; their collision time τ_e is greater than their end-loss time $\tau_{||}$. With the addition of a kinetic stabilizer beam it is unclear what portion of electrons will be trapped and what portion lost. In section 6.3 we will calculate the fraction of electrons trapped in the expander in order to determine the model that is most appropriate to adopt for the electron distribution. There are two possibilities: if most electrons are well-trapped by the kinetic stabilizer beam, then the electrons will have a collision time $\tau_e < \tau_{||}$ and will thus be isotropic. Such a distribution is well described by a Maxwellian. Otherwise, if electron are not trapped well enough to become isotropic, they will be described by a non-isotropic distribution. In this section we examine potentials that result from a Maxwellian distribution of electrons.

When a critical mass of warm electrons is trapped in the expander, electrons are well described by a Maxwellian distribution, as noted above. For a Maxwellian distribution of electrons, the electron density is proportional to the ion density at the wall, and grows as an exponential of the electric potential energy divided by the electron temperature away from the wall. If the ion density at the wall is n_{w}, then the density of electrons is

$$n_e(B) = n_i(B_{\mathrm{w}})\mathrm{e}^{\varphi/T_{\mathrm{e}}} = n_{\mathrm{w}}\mathrm{e}^{\varphi/T_{\mathrm{eks}}} \ . \tag{6.16}$$

We solve the quasi-neutral condition using the boundary conditions $\varphi_{\mathrm{w}} = 0$ and φ_{T} constant at the target. We consider the electron temperature in an implicit manner, dependent on φ_{T} and specified values of the magnetic field

$$T_{\mathrm{eks}}(\varphi_{\mathrm{T}}) = \frac{\varphi_{\mathrm{T}}}{\ln n_{\mathrm{i}}(B_{\mathrm{T}}, \varphi_{\mathrm{T}}, B_{\mathrm{w}}) - \ln n_{\mathrm{w}}(\varphi_{\mathrm{T}}, B_{\mathrm{w}})} \ . \tag{6.17}$$

The temperatures that result from a Maxwellian electron distribution are shown in Figure 6.4; these temperatures are low enough that the temperature needed to meet the stability criterion for the trapped particle mode may

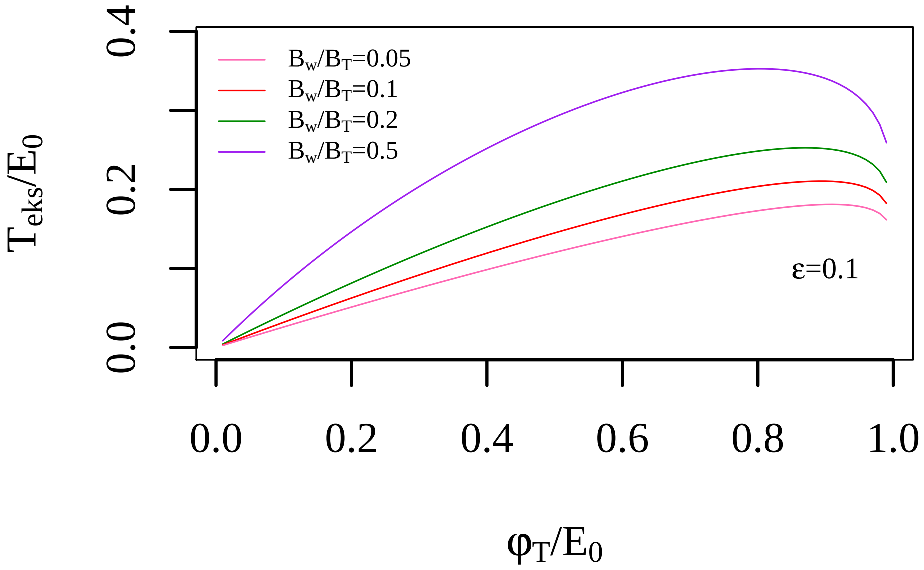

Figure 6.4: Electron temperature of a short-mean-free-path electron distribution *vs.* the value of the electric potential at the target φ_{T}. Both quantities are normalized to the energy of the incoming beam E_0.

be difficult to obtain. To solve for φ, we use the quasi-neutral condition in the form of a differential equation

$$\varphi = T_{\mathrm{eks}} \left[\ln n_{\mathrm{i}}(B,\varphi) - \ln n_{\mathrm{w}}\right] , \tag{6.18}$$

$$\frac{1}{T_{\mathrm{eks}}} \frac{\partial \varphi}{\partial B} \mathrm{e}^{\varphi/T_{\mathrm{eks}}} = \frac{\partial}{\partial B} \left(\frac{n_{\mathrm{i}}(B,\varphi)}{n_{\mathrm{w}}} \right) . \tag{6.19}$$

The electrostatic potential has two characteristic types of solutions. If $B_{\mathrm{w}}/B_{\mathrm{T}} < \varepsilon$, φ has a limiting value φ_p as the magnetic field B becomes large and φ_p is positive. Physically, φ_p is the potential energy of the plasma in the plug of the tandem mirror. If $B_{\mathrm{w}}/B_{\mathrm{T}} > \varepsilon$ then the electrostatic potential φ asymptotes

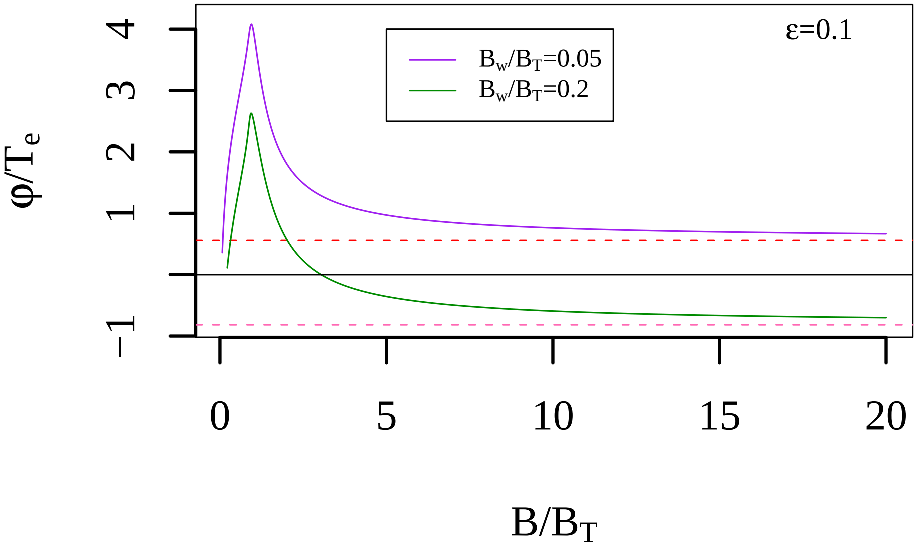

Figure 6.5: Potential φ in the case of a Maxwellian electron distribution. For this choice of parameters ($\varepsilon = .1$, $\varphi_\mathrm{T}/E_0 = .3$) the potential has two characteristic types of solutions: those that are positive for all B/B_T , and those that become negative as B/B_T increases. The dashed lines show the limit of each φ as the magnetic field becomes large.

to a negative value φ_p; this negative potential has the same effect as a thermal barrier, trapping electrons that leave the plug region and preventing them from reaching the kinetic stabilizer. Examples of these two types of solutions are shown in Figure 6.5. The negative φ_p solution would prevent stabilization of trapped particle mode. However if there is sufficient spread of magnetic moments in the kinetic stabilizer beam, measured by $\varepsilon > B_\mathrm{w}/B_\mathrm{T}$, φ_p is positive, and stabilization of the trapped particle φ mode is possible.

In section 6.3 we will verify whether a Maxwellian distribution occurs by calculating the fraction of particles trapped by the kinetic stabilizer. If a Maxwellian distribution of electrons exists around the kinetic stabilizer, this is a major insight into how the kinetic stabilizer effects both the plasma and the character of a trapped particle mode. Trapped particle instabilities are of great concern because they can have a growth rate that is close to the growth rate of ideal MHD modes [59]. Collisional terms could contribute to lowering the growth rate of the the trapped particle mode, with the result that it would be small compared with the MHD growth rate.

6.2 MHD Stabilization

In most tandem mirror designs, the primary destabilization is caused by the negative (unfavorable) curvature in the plug; the central cell destabilization is small in comparison. This is the case if the central cell is much longer than the plug, because the instability drive scales inversely with the axial length of the machine; in our proposed machine the central cell length $2L_\mathrm{c} = 200$ m and the plug length $L_\mathrm{p} = 2.05$ m. For an axisymmetric magnetic field, the criterion for MHD stability is the integral we derived in eq. (4.51):

$$I = \int_{-L}^{L} \mathrm{d}z (p_\perp + p_{||}) r^3(z) \frac{d^2 r(z)}{dz^2} > 0 \quad . \tag{6.20}$$

The stability integral is performed over the entire length of the system between its physical ends. The field-line radius r is given by eqs. (6.2) and (6.3).

To determine whether MHD stability can be achieved, we evaluate eq. (6.20) separately over the plug region and the expander region. For the tandem mirror machine with parameters given in column two of Table 6.1, the stability integral in the plug region is

$$I_{\text{plug}} = \int_{\text{plug}} \mathrm{d}z (p_\perp + p_{||}) r^3(z) \frac{\partial^2 r(z)}{\partial z^2} = -8850.1 \text{ Pa m}^3 \ . \tag{6.21}$$

This is a negative stability number because the plug region is destabilizing. In the case of the kinetic stabilizer, there is a large positive contribution to this integral outside the plugs, because of the pressure from the kinetic stabilizer beam in the expander. If this positive curvature exceeds the net negative contribution that arises from the plasma in the plugs and in the central cell, the machine will be MHD stable. The kinetic stabilizer has the effect of weighting the stability integral toward the expander region. To perform the MHD stability integral in eq. (6.20) over the expander region we use the pressures created by the kinetic stabilizer beam in eqs. (6.14) and (6.15). The result is 12272.4 Pa m^3, giving a net positive value of 3422 Pa m^3. Thus for this tandem mirror of total length at 349 m we verify Post's result [26] of MHD stability with a kinetic stabilizer.

Taking into account the paraxial limit, the adiabaticity condition, and the necessity of MHD stability, we develop scaling relations that permit identification of system parameters for a satisfactory operating regime

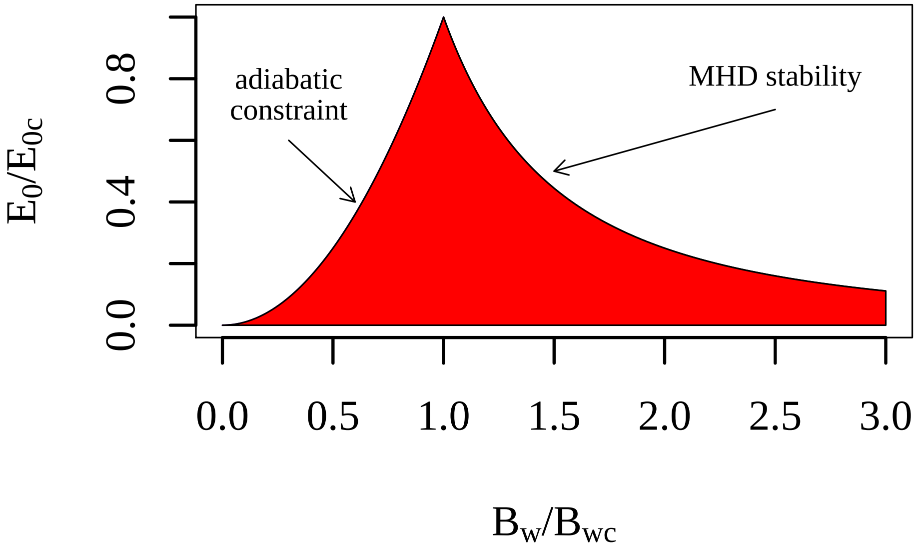

Figure 6.6: A successful operating regime for an axisymmetric mirror that is MHD stable as a consequence of kinetic stabilizers is indicated by the shaded region. We assume that the target is at or near the beginning of the favorable curvature region, and take into account the paraxial condition, the adiabaticity condition, and MHD stability. The critical energy $E_{0\mathrm{c}}$ and magnetic field at the wall B_{wc} are defined in eqs. (6.23) -(6.24).

$$
\begin{aligned}
&1.2 \cdot 10^{-3}\sqrt{E_0(\mathrm{keV})}\left(\frac{10}{L_{\mathrm{quad}}(\mathrm{m})}\right) < B_{\mathrm{w}}(\mathrm{T}) < \left(\frac{3.8 \cdot 10^{-4}}{\sqrt{E_0(\mathrm{keV})}}\right) \\
&\times \left(\frac{f_0}{3}\right)^2 2\beta \left(\frac{L_{\mathrm{c}}(\mathrm{m})}{50}\right)\left(\frac{2L_{\mathrm{plug}}}{L_{\mathrm{quad}}}\right)\left(\frac{10p_{\mathrm{c}}}{p_{\mathrm{plug}}}\right)\left(\frac{100\mathrm{keV}}{T_{\mathrm{e}}(\mathrm{keV}) + T_{\mathrm{i}}(\mathrm{keV})}\right)
\end{aligned}
\tag{6.22}
$$

Here L_{quad} is the length of the quadratic field-line radius section, where there is favorable curvature for stability. L_{plug} is the length of the plug and L_{c} is half the length of the central cell. β is the plasma parameter calculated in the central cell, and p_{c} is the plasma pressure in the central cell. Eq. (6.22) shows how system parameters can be adjusted to insure an operating window for MHD stability. This operating window is depicted in Figure 6.6. The critical values of energy $E_{0\mathrm{c}}$ and magnetic field at the wall $E_{0\mathrm{c}}$ occur when the upper and lower limits of eq. (6.22) converge. These values are

$$E_{0\mathrm{c}} = \frac{3.8}{120}\left(\frac{f_0}{3}\right)^3 4\beta\frac{L_{\mathrm{c}}L_{\mathrm{plug}}}{50}\left(\frac{10p_{\mathrm{c}}}{p_{\mathrm{plug}}}\right)\left(\frac{100\mathrm{keV}}{T_{\mathrm{e}}(\mathrm{keV})+T_{\mathrm{i}}(\mathrm{keV})}\right) \quad (6.23)$$

$$B_{\mathrm{wc}} = 3.14\cdot 10^{-5}\frac{\beta}{r_0^2 f_0}\left(\frac{f_0}{3}\right)^3\frac{L_{\mathrm{c}}L_{\mathrm{plug}}}{50}\left(\frac{10p_{\mathrm{c}}}{p_{\mathrm{plug}}}\right)\left(\frac{100\mathrm{keV}}{T_{\mathrm{e}}(\mathrm{keV})+T_{\mathrm{i}}(\mathrm{keV})}\right) \quad (6.24)$$

Typical values for $E_{0\mathrm{c}}$ and B_{wc} range between $0.25-0.5$ keV and $1-2\cdot 10^{-4}$ T respectively.

6.3 The Trapped Particle Mode

The condition for stabilization of the trapped particle mode based on charge separation [55] [56] is a condition on the electron temperature at the kinetic stabilizer target

$$T_{\mathrm{eks}} \geq \frac{1}{f_{\mathrm{tc}}}\left(\int_{z_{\mathrm{T}}}^{z_{\mathrm{wall}}} \mathrm{d}z(p_{\perp}+p_{||})r(z)^3\frac{d^2r(z)}{dz^2}\right) / \left(r_0^2 f_0\int_{z_{\mathrm{plug}}}^{z_{\mathrm{wall}}}\mathrm{d}z\frac{n}{B}\right) . \quad (6.25)$$

The critical electron temperature given in eq. (6.25) was derived for long-mean-free-path electrons because that has usually been the case for tandem mirrors. Future work to add collisional effects to this stability condition is warranted. In order to determine whether the trapped particle mode can be stabilized, we must determine what range of electron temperatures at the target of the kinetic stabilizer, T_{eks}, satisfy this condition. T_{eks} is highly dependent on the fraction f_{tc} of electrons that bounce back and forth between the plug and the stabilizer.

There are three types of electrons in the expander region: lost, trapped in the potential well around the kinetic stabilizer target, and trapped between the plug and the kinetic stabilizer target. Lost electrons are those electrons in the loss-hyperbole that exit the mirror axially in one bounce time. Electrons can be trapped in the area of the kinetic stabilizer because the kinetic stabilizer beam sets up a positive potential that confines low energy electrons electrostatically. We are most interested in the third type of electrons, those that reflect off of the kinetic stabilizer potential to bounce back up to the plug area; we call these electrons "connecting" electrons because they connect the plug to the kinetic stabilizer. Both the electrons trapped around the kinetic stabilizer potential and those that are connecting are trapped inside the expander region of the machine; we will refer to these electrons as "trapped". The total number of electrons per flux surface in the expander region is

$$N_{\text{tot}} \;=\; \int\limits_{z_{\text{w}}}^{z_{\text{m}}} \frac{\mathrm{d}z}{B} \int\limits_{-\varphi}^{\infty} \mathrm{d}E \ \mathrm{e}^{-E/T_{\text{eks}}} \int\limits_{0}^{(E+\varphi)/B} \frac{\mathrm{d}\mu B}{\sqrt{E+\varphi-\mu B}} \ . \tag{6.26}$$

The total number of trapped electrons per flux surface is

$$N_{\text{t}} \;=\; \int\limits_{z_{\text{w}}}^{z_{\text{m}}} \frac{\mathrm{d}z}{B} \int\limits_{-\min(\varphi,\varphi_{\text{p}})}^{E_{\max}} \mathrm{d}E \ \mathrm{e}^{-E/T_{\text{eks}}} \int\limits_{0}^{(E+\varphi)/B} \frac{\mathrm{d}\mu B}{\sqrt{E+\varphi-\mu B}} \ . \tag{6.27}$$

The limits for magnetic moment and energy both deserve detailed explanation. For any φ, the magnetic moment of of electrons must be less than $(E+\varphi)/B$.

Most of the connecting electrons have a magnetic moment $\mu \leq \mu_{\mathrm{m}} = \varphi_{\mathrm{p}}/(B_M - B_W)$.

The limits for E in eqs. (6.26) and (6.27) are explained in Figure 6.7. As we discussed earlier, φ_p is the potential energy of the plasma in the plug of the tandem mirror. Energy is defined

$$E = \frac{1}{2}v_{||}^2 - \varphi + \mu B \ . \tag{6.28}$$

Electrons that have magnetic moment μ greater than μ_{m} are not confined in the expander region. For particles trapped in the expander region, the turning points of their motion are at the maximum B of the plug and close to the wall. At these point $v_{||} = 0$ and so for trapped electrons $E_{\mathrm{max}} = \mu_{\mathrm{m}} B_{\mathrm{max}} - \varphi_{\mathrm{p}} = \mu_{\mathrm{m}} B_{\mathrm{w}}$. Minimum energy trapped electrons have $\mu = 0$, and so $E_{\mathrm{min}} = -\varphi$. The total fraction of trapped electrons is a simple ratio of particle counts

$$f_{\mathrm{t}} = \frac{N_{\mathrm{t}}}{N_{\mathrm{tot}}} \ . \tag{6.29}$$

After performing these integrations, our final formula for the fraction of trapped electrons is:

$$f_{\mathrm{t}} = \frac{\int\limits_{z_{\mathrm{w}}}^{z_{\mathrm{m}}} \frac{\mathrm{d}z}{B} \left(\exp\left(\varphi/T_{\mathrm{eks}}\right) \mathrm{erf}\left[\sqrt{\frac{\varphi}{T_{\mathrm{eks}}}}\right] - 2\sqrt{\frac{\varphi}{\pi T_{\mathrm{eks}}}} \right)}{\int\limits_{z_{\mathrm{w}}}^{z_{\mathrm{m}}} \frac{\mathrm{d}z}{B} \exp\left(\varphi/T_{\mathrm{eks}}\right)} \ . \tag{6.30}$$

The fraction of trapped electrons for $T_{\mathrm{eks}}/E_0 = 0.09$, $B_{\mathrm{W}} = 9.3 \cdot 10^{-4}$ T, and $B_{\mathrm{T}} = 15.34$ T is $f_{\mathrm{t}} = 0.886$ T or 89%. Clearly the bulk of electrons that escape from the plug region do remain trapped in the machine when a kinetic stabilizer beam is present. This observation verifies that our choice of a Maxwellian distribution of electrons is physically relevant even in the long-mean-free-path limit.

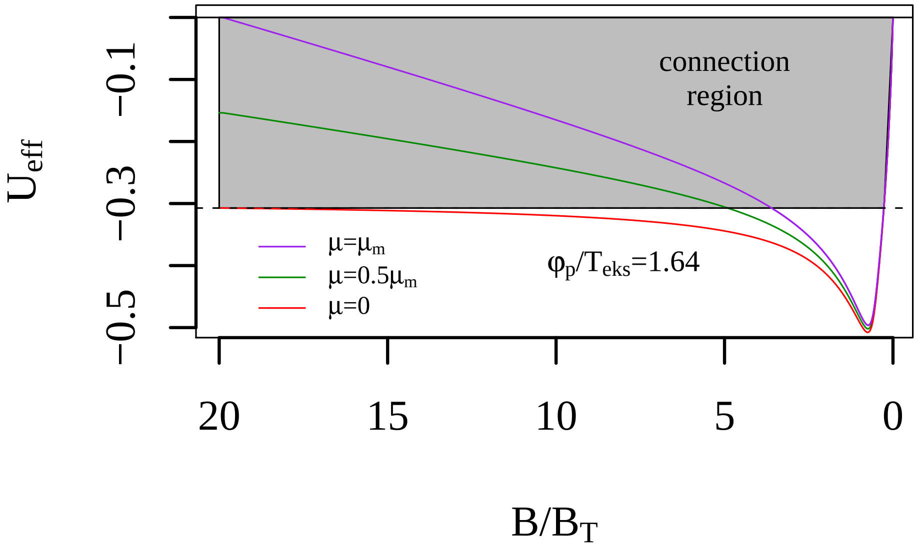

Figure 6.7: The effective potential for Maxwellian electrons in the whole expander region, the range $B/B_{\mathrm{T}} = 0.1$- 20 corresponds to $B_{\mathrm{w}} < B < B_{\mathrm{m}}$. In these graphs $\mu_{\mathrm{m}} = \varphi_{\mathrm{p}}/(B_{\mathrm{m}} - B_{\mathrm{w}})$.

The total number per flux surface of trapped and connecting electrons,

N_{tc}, can be expressed

$$\begin{aligned} N_{\mathrm{tc}} &= \int\limits_{z_{\mathrm{w}}}^{z_{\mathrm{c}}} \frac{\mathrm{d}z}{B} \int\limits_{-\varphi_{\mathrm{p}}}^{E_{\mathrm{max}}} \mathrm{d}E \; \mathrm{e}^{-E/T_{\mathrm{eks}}} \int\limits_{0}^{(E+\varphi_{\mathrm{p}})/B_{\mathrm{m}}} \frac{\mathrm{d}\mu B}{\sqrt{E+\varphi-\mu B}} \\ &+ \int\limits_{z_{\mathrm{c}}}^{z_{\mathrm{w}}} \frac{\mathrm{d}z}{B} \int\limits_{-\varphi}^{E_{\mathrm{c}}} \mathrm{d}E \; \mathrm{e}^{-E/T_{\mathrm{eks}}} \int\limits_{0}^{(E+\varphi)/B} \frac{\mathrm{d}\mu B}{\sqrt{E+\varphi-\mu B}} \\ &+ \int\limits_{z_{\mathrm{c}}}^{z_{\mathrm{w}}} \frac{\mathrm{d}z}{B} \int\limits_{E_{\mathrm{c}}}^{E_{\mathrm{max}}} \mathrm{d}E \; \mathrm{e}^{-E/T_{\mathrm{eks}}} \int\limits_{0}^{(E+\varphi_{\mathrm{p}})/B_{\mathrm{m}}} \frac{\mathrm{d}\mu B}{\sqrt{E+\varphi-\mu B}} \; . \end{aligned} \tag{6.31}$$

For an electron to bounce back and forth between the plug and the kinetic stabilizer, it cannot be trapped in the potential well surrounding the kinetic stabilizer target. The effective energy well U_{eff} for these electrons is

$$U_{\mathrm{eff}} = \mu(B - B_{\mathrm{w}}) - \varphi \; . \tag{6.32}$$

is shown in Figure 6.7. The minimum energy for connecting electrons is thus $E_{\mathrm{min}} = -\varphi_{\mathrm{p}} > -\varphi$; near the wall $-\varphi_{\mathrm{p}} < -\varphi$, and the limit is again $-\varphi$. In eq (6.31) we have split up the integral in order to make this switch in limits transparent. Here z_{m} is the location of the maximal magnetic field, *i.e.* the peak of the plug and z_{c} is the point where $\varphi(z_{\mathrm{c}}) = \varphi_{\mathrm{p}}$, the limit of φ at high magnetic field. The critical energy is $E_{\mathrm{c}} \equiv (\varphi B_{\mathrm{m}} - \varphi_{\mathrm{p}} B)/(B_{\mathrm{m}} - B)$. The total fraction of trapped and connecting electrons is the ratio of particle counts

$$f_{\mathrm{tc}} = \frac{N_{\mathrm{tc}}}{N_{\mathrm{tot}}} \; . \tag{6.33}$$

A calculation of this fraction at $T_{\mathrm{eks}}/E_0 = 0.09$, $B_{\mathrm{W}} = 9.3 \cdot 10^{-4}$ T, and $B_{\mathrm{T}} = 15.34$ T yields $f_{\mathrm{tc}} = 0.427$ or approximately 43%. Fractions of electrons are shown in Figure 6.8 for various target positions and in Figure 6.9 for various ε. Given the large percentage of trapped electrons when a kinetic stabilizer is present in the expander, a short-mean-free-path for electrons is realistic, and a Maxwellian distribution of electrons is accurate.

Table 6.1: Parameters for marginally MHD-stable KSTM design

Parameter	TPM Unstable	collisional	collisional, target near plug
β	0.5	0.5	0.5
power	100 MW	100 MW	100 MW
r_0	0.63 m	0.55 m	0.55 m
f_0	2.04 T	2.18 T	2.18 T
L_{c}	200 m	200 m	200 m
L_{plug}	2.05 m	2.05 m	2.05 m
L_{exp}	72.5 m	72.5 m	72.5 m
L_{quad}	55.61 m	55.61 m	55.61 m
$\lambda_{\mathrm{mfp,eks}}$	40.7 m	0.17 m	0.01 m
n_{c}	$6.5 \cdot 10^{19}$ m^{-3}	$7.4 \cdot 10^{19}$ m^{-3}	$7.4 \cdot 10^{19}$ m^{-3}
n_{T}	$3.37 \cdot 10^{17}$ m^{-3}	$1.1 \cdot 10^{20}$ m^{-3}	$2.2 \cdot 10^{21}$ m^{-3}
$p_{\mathrm{T}} = p_{\perp} + p_{\|\|}$	2.6 Pa	433.6 Pa	4354.5 Pa
ε	0.5	0.5	0.5
E_0	100 eV	100 eV	100 eV
φ_{T}/E_0	0.8	0.9	0.95
f_{tc}	2.1%	14.1%	16.4%
T_{eks}/E_0 obtained	0.32	0.11	0.084
T_{eks}/E_0 required	18	2	1.4
T_{e}	60 keV	60 keV	60 keV
T_{i}	20 keV	20 keV	20 keV
B_{w}	$1 \cdot 10^{-3}$ T	$8.2 \cdot 10^{-4}$ T	$8.2 \cdot 10^{-4}$ T
B_{T}	$5.3 \cdot 10^{-3}$ T	1.02 T	14.4 T
B_{m}	24.9 T	20.3 T	20.3 T
$B_{\mathrm{plug\ min}}$	14 T	11.4 T	11.4 T
R_{M}	1.8	1.8	1.8
ϕ_{c}	41.6 keV	41.6 keV	41.6 keV
instability drive	2.35	3.2	3.2

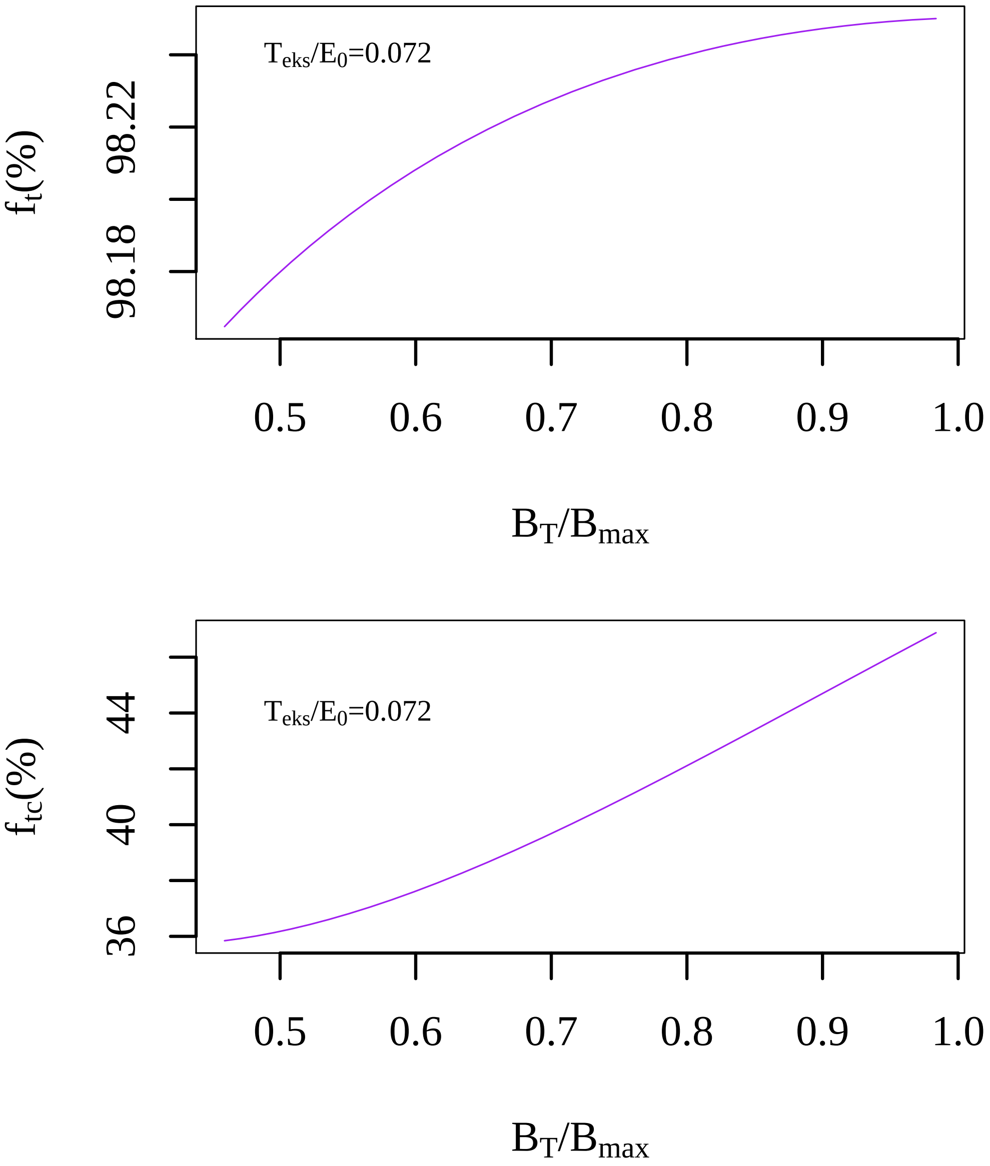

Figure 6.8: The fraction of electrons in the expander that are trapped (above), and that are both trapped and connect the kinetic stabilizer to the plug region (below) for a Maxwellian electron distribution at constant electron temperature $T_{\rm eks}/E_0 = 0.072$ *vs.* magnetic field at the target normalized to its maximum value.

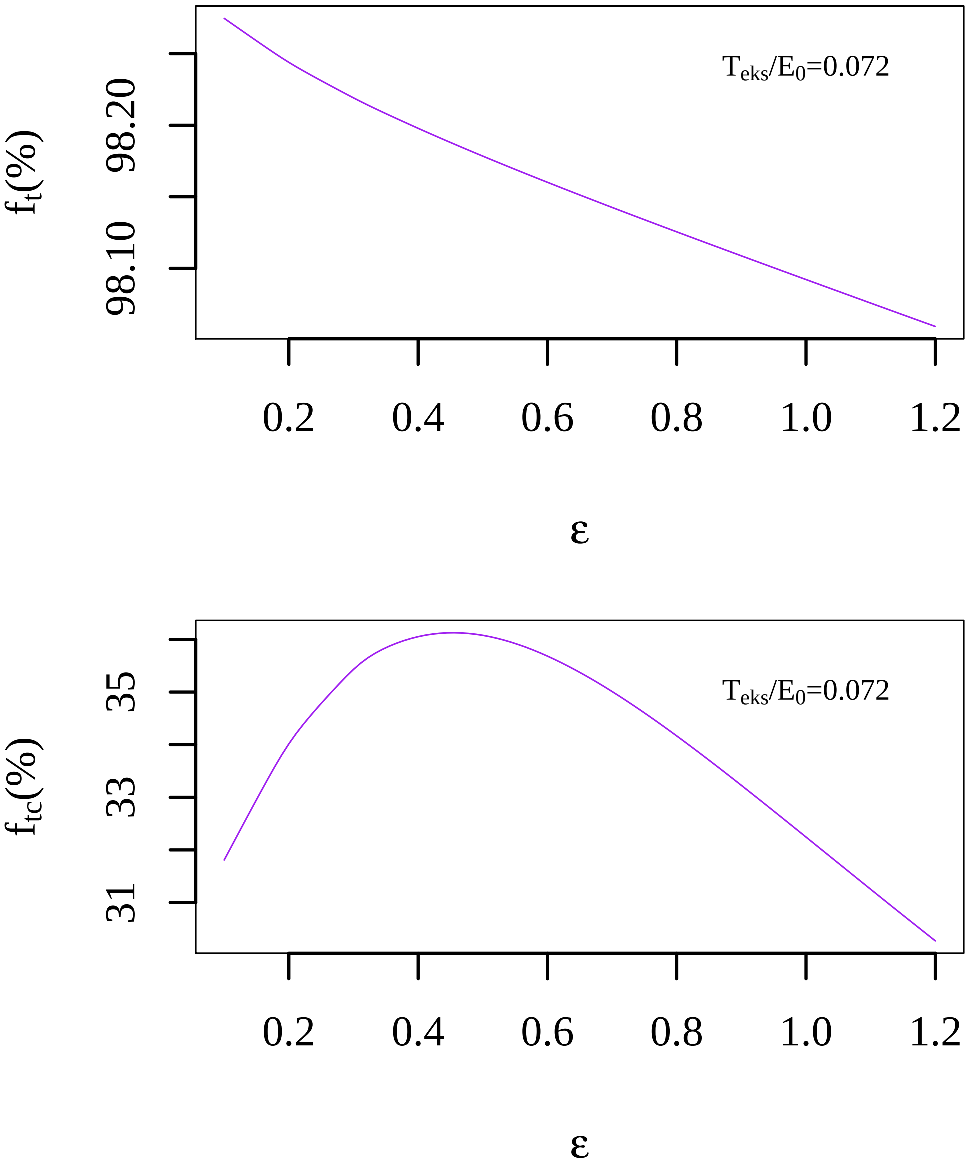

Figure 6.9: The fraction of electrons in the expander that are trapped (above), and that are both trapped and connect the kinetic stabilizer to the plug region (below) for a Maxwellian electron distribution *vs.* ε, the dimensionless parameter that controls the distribution of magnetic moments in the kinetic stabilizer beam.

6.4 Existence of a fast growing Trapped Particle Mode

As we mentioned previously, the stability criterion for trapped particle modes in eq. (6.25) is only valid in the case of long mean-free-path electrons. In order to determine whether short mean-free-path electrons occur with a kinetic stabilizer, we calculate the mean-free-path of electrons in the expander using [60]

$$\begin{aligned} \lambda_{\mathrm{mfp}} &= \frac{v_{\mathrm{th,e}}}{\nu_{\mathrm{e}}} && (6.34) \\ \nu_{\mathrm{e}}(\mathrm{sec}^{-1}) &\approx 2.9 \cdot 10^{-6} n(\mathrm{cm}^{-3}) \lambda T_{\mathrm{e}}^{-3/2}(\mathrm{eV}) && (6.35) \end{aligned}$$

where the Coulomb logarithm is estimated as $\lambda \approx 15$. For MHD stable machines, the mean-free-path of electrons at the target $\lambda_{\mathrm{mfp,eks}}$ depends on target choice. Table 6.1 contains mean-free-path values for three machine designs where the target position, and those variables dependent on the target position are varied, and the pressure in the plug is varied in order to maintain marginal MHD stability. All other parameters are held fixed: the fusion power of the central cell, the plasma parameter β, the length of the good curvature region L_{quad}, length of the plug L_{plug}, length of the expander L_{exp}, length of the central cell L_{c}, ε, E_0, the temperatures in the central cell T_{e} and T_{i}, and the magnitude of the ambipolar potential in the plug ϕ_{c}.

In the first column of Table 6.1 is a machine design for which the target is chosen as close to the wall as possible; MHD stability is still achieved with a sufficient ambipolar potential in the plug region. For this machine, $\lambda_{\mathrm{mfp,eks}} \sim L_{\mathrm{quad}}$, and so the electrons can be considered to have long mean-free-path, and the trapped particle stability condition in eq. (6.25) is relevant. The trapped particle mode is unstable; as a result of the low electron temperature around the target and small fraction of trapped and connecting electrons the growth rate of the trapped particle mode is comparable to the MHD growth rate.

If the target is moved further into the expander plasma, the temperature of electrons at the target position increases, as does the fraction of trapped and connecting electrons. The mean-free-path $\lambda_{\mathrm{mfp,eks}}$ is reduced substantially for targets that are deeper into the plasma and further from the wall. Indeed, as is illustrated by the second and third columns in Table 6.1 the plasma becomes collisional before the temperature of the electrons is high enough to satisfy eq. (6.25). The second column of Table 6.1 summarizes a design where the target is close to the beginning of the favorable curvature region; the third column of Table 6.1 summarizes a design where the target is extremely close to the plug maximum. The the electrons for these machine designs are collisional, and therefore the growth rate for a trapped particle mode may be substantially slower than the MHD growth rate. For the design with the target close to the plug maximum in the third column of Table 6.1, it is likely that the beam could not penetrate to the target region. The question of beam penetration will be addressed more fully in our future work.

Chapter 7

Kinetic Stabilization Discussion and Conclusions

In Chapter 6 we have discussed designs for a machine that is constrained by the power-balance equation; the fusion energy produced by the central cell must exceed the energy required to maintain a kinetic stabilizer in the expander. Our designs satisfy the paraxial condition and have a magnetic field that is adiabatic at the wall. We find that the adiabaticity condition confines the operating regime for a successful machine to relatively low kinetic stabilizer beam energy $E_0 \leq 300$ eV. Low beam energies boost the MHD stabilization effect, allowing MHD stability to be achieved when there is a high ambipolar potential in the plug region. This is a result of the power-balance constraint; the pressure in the expander from the kinetic stabilizer beam increases with decreasing beam energy E_0. A large ambipolar potential and a high pressure in the plug are desirable for maximal confinement; this makes it necessary to maintain a large density of ions in the plug region. MHD stability is possible with a large ambipolar potential in the plug if the kinetic stabilizer beam is targeted at, or before, the beginning of the favorable curvature region shown in Figure 6.2. We expect that MHD stability could be achieved for a higher plug pressure as well as for shorter design with an optimized expander magnetic field. The optimized magnetic field profile satisfies the paraxial constraint everywhere by a small margin; our current model satisfies the paraxial constraint everywhere but approaches a break-down of the paraxial approximation at the wall. This is a topic of our continuing research.

For many MHD-stable machine designs, there exists a trapped particle mode with a growth rate comparable to the MHD growth rate. An example of such a design is outlined in the first column of Table 6.1. For this example design and many others, the electrons around the kinetic stabilizer beam are Maxwellian. Placement of the target deeper into the plasma, and closer to the plug allows for a much larger percentage of out-flowing electrons to be trapped in the expander between the plug and the target; a large fraction of these trapped warm electrons bounce between the kinetic stabilizer and the plug. Thus a beam targeted in the expander close to the plugs can have a sufficient electron temperature and fraction of connecting electrons to satisfy the trapped particle stability criterion of Berk and Lane in eq. (6.25). But when the target is chosen close to the plug, the mean-free-path of the electrons at the target is short, and the plasma is collisional; this is clearly demonstrated by progression of target positions taken in Table 6.1. The present stability criterion is not applicable to collisional plasmas.

The recognition that the electrons around the kinetic stabilizer beam target can form a collisional plasma is a significant insight. The stability condition for trapped particle modes in eq. (6.25) should be re-examined and extended to include collisional effects. This is our next step. We conjecture that in a collisional plasma created by the kinetic stabilizer beam, the growth rate of a trapped particle mode in the central cell of a tandem mirror would be significantly slower than the MHD growth rate. If this were the case, then the trapped particle instability would be less virulent than the criterion indicates. If significant, the trapped particle mode may be controlled by feedback stabilization. A full examination of collisional effects on the trapped particle mode will be undertaken in our future work.

There are a number of further issues that warrant further study. The effect of collisions on the distance that a beam can reach into an expander plasma remains a question to be addressed. The placement of the target near the ambipolar potential of the plug is also potentially problematic; there is a possibility that cold electrons could reach the plug region and affect the hot, core electrons. Ion current requirements for a low-energy kinetic stabilizer beam could also prove to be a technical issue; ion current approaching 1 MA is necessary to create an extremely low-energy kinetic stabilizer beam, but this could be reduced with an optimized magnetic field. These issues need to be addressed in future work.

Bibliography

[1] Simonen, T. *The Status of Mirror Research.* Fusion Power Associates Meeging 12/4/2008, (2008).

[2] T. Cho et al. Observation and Control of Transverse Energy-Transport Barrier due to the Formation of an Energetic-Electron Layer with Sheared E cross B Flow. *Phys. Rev. Lett.* **97**, 055001 (2006).

[3] Ryutov, D. Open-Ended Traps. *Sov. Phys. Uspekhi* **31**(4), 300–327 (1988).

[4] Chirikov, B. V. A Universal Instability of Many-Dimensional Oscillator Systems. *Phys. Rep.* **52**(5), 263 – 379 (1979).

[5] T. K. Fowler and B.G. Logan. The Tandem Mirror Reactor. *Comments Plas. Phys. Con. Fus.* **2**(6), 167–172 (1977).

[6] Dimov, G. I. The Ambipolar Trap. *Sov. Phys. Uspekhi* **48**(11), 1129–1149 (2005).

[7] Simonen, T. Experimental Progress in Magnetic-Mirror Fusion Research. *Proc. IEEE* **69**(8), 935–957 (1981).

[8] Hazeltine, R. D. and Meiss, J. D. *Plasma Confinement.* Courier Dover Publications, (2003).

[9] Anikeev AV, Bagryansky PA, Deichuli PP, Ivanov AA, Karpushov AN, Maximov VV, Podminogin AA, Stupishin NV, Tsidulko YA. Observation of Magnetohydrodynamic Stability Limit in a Cusp-Anchored Gas-Dynamic Trap. *Phys. Plas.* **4**(2), 347 (1997).

[10] T. Cho et al. Observation of the Effects of Rdially Sheared Electric Fields on the Suppression of Turbulent Vortex Structures and the Associated Transverse Loss in GAMMA-10. *Phys. Rev. Lett.* **94**, 085002 (2005).

[11] Yasaka, Y., Yamamoto, T., Kurumatani, Y., Takeno, H., Nakashima, Y., Cho, T., Tomita, Y., and Ishikawa, M. Experiment on Direct Energy Conversion from Tandem Mirror Plasmas by Using a Slanted Cusp Magnetic Field. *Nuc. Fus.* **48**(3), 035015 (6pp) (2008).

[12] Bagryansky, P. and Ivanov, A. Gas Dynamic Trap As High Power 14 MeV Neutron Source. *Fusion Eng. Design* **70**(1), 13–33 (2004).

[13] Taylor, J. B. Some stable plasma equilibria in combined mirror-cusp fields. *Phys. Fluids* **6**(11), 1529–1536 (1963).

[14] Simonen, T. C. High Pressure Plasma Stability with Favorable Magnetic Field Line Curvature. *Plasma Phys. Rep.* **23**(9), 713 (1997).

[15] R. F. Post, TK Fowler, R. Bulmer, J. Byers, D. Hua, L. Tung. Axisymmetric Tandem Mirrors: Stabilization and Confinement Studies. *Fusion Sci. Tech.* **47**, 49–58 (2005).

[16] Post, R. Combining the “Kinetic Tandem” and the “Kinetic Stabilizer” concepts. *J. Fus. Energy* **26**(1-2), 149–153 (2006).

[17] T. Cho, J. Kohagura, M. Hirata, et al. *Nuc. Fus.* **45 (12)** (2005).

[18] I. Katanuma. Private correspondence, April 12, (2007).

[19] I. Katanuma. Private correspondence, Feb 26, (2009).

[20] Tamano, T. Tandem mirror experiments in GAMMA-10. *Phys. Plas.* **2**(6), 2321–2327 (1995).

[21] Ivanov, A. In Physics of Alternative Magnetic Confinement Schemes, Ortolani, S. and Sindoni, E., editors, 443–458. Societa Italiana di Fisica, (1991).

[22] Ryutov, D. Axisymmetric MHD-Stable Mirrors. In Physics of Alternative Magnetic Confinement Schemes, Ortolani, S. and Sindoni, E., editors, volume 2, 791–816. Societa Italiana di Fisica, (1987).

[23] Post, R. The Kinetic Stabilizer; A Route to Simpler Tandem-Mirror Systems? In Current Trends in International Fusion Research: Proceedings of the Fourth Symposium, Charles D Orth, E. P., editor, 291. NRC Research Press, (2007).

[24] Post, R. and Ryutov, D. Attractive Characteristics of Mirrors, (1994).

[25] Lane, B., Post, R., and Kesner, J. Stabilization Of MHD Modes in an Axisymmetric Plasma Column Through the Use of a Magnetic Divertor. *Nuc. Fus.* **27**(2), 277–286 (1987).

[26] Post, R. The Kinetic Stabilizer Axisymmetric Tandem Mirror: A Review of Approaches to Its Implementation. *Fusion Sci. Tech.* **51**(2), 112–117 (2007).

[27] J. Pratt and W. Horton. Global Energy Confinement Scaling Predictions for the Kinetically Stabilized Tandem Mirror. *Phys. Plas.* **13**, 042513 (2006).

[28] Asp, E., Kim, J.-H., Horton, W., Porte, L., Alberti, S., Karpushov, A., Martin, Y., Sauter, O., Turri, G., and the TCV TEAM. Electron Thermal Transport Analysis in Tokamak Configuration Variable. *Phys. Plas.* **15**(8), 082317 (2008).

[29] B.P. LeBlanc, R.E. Bell, S.M. Kaye, et al. Confinement Studies Of Auxiliary Heated NSTX Plasmas. *Nuc. Fus.* **44**(4) (2004).

[30] T. Cho. *Private correspondence, Dec 24.* (2006).

[31] Kaye, S. and the ITER Confinement Database Working Group. ITER L-Mode Confinement Database. *Nuc. Fus.* **37**, 1303 (1997).

[32] Becker, G. Scaling Law for Effective Heat Diffusivity in ELMY H Mode Plasmas. *Nuc. Fus.* **44**(11) (2004).

[33] Rome, J. A. Stellarator News May, (2004).

[34] Equilibrium and Stability of Collisionless Systems in the Paraxial Limit. William A. Newcomb. *J. Plas. Phys.* **26**(3), 529–584 (1981).

[35] Pearlstein, L. D., Kaiser, T. B., and Newcomb, W. A. Analytic Equilibria with Quadrupole Symmetry in the Paraxial Limit. *Phys. Fluids* **24**(7), 1326–1335 (1981).

[36] Kaiser, T. B. and Pearlstein, L. D. Ballooning Modes in Quadrupole Tandem Mirrors. *Phys. Fluids* **26**(10), 3053–3065 (1983).

[37] Rosenbluth, M.N., Krall, N.A., Rostoker, N. Finite Larmor Radius Stabilization of "Weakly" Unstable Confined Plasmas. *Nucl. Fus. Supp.* **2**(1), 143–50 (1962).

[38] Kotelnikov, I. and Romé, M. Equilibrium Of Non-Neutral Plasmas in a Malmberg–Penning Trap With A Weakly Tilted Magnetic Field. *Phys. Plas.* **15**(7), 072118 (2008).

[39] Hopper, E. J. Octupole Anchor for Tandem Mirrors., (1984).

[40] McNamara, B. and Pearlstein., L. D. Spectral Computation of Tandem mirror equilibria with Finite Larmor Radius Effects. *Space Sci. Rev.* **42**(3-4), 541–551 (2004).

[41] Furth, H. P., Killeen, J., and Rosenbluth, M. N. Finite-Resistivity Instabilities of a Sheet Pinch. *Phys. Fluids* **6**(4), 459–484 (1963).

[42] Post, R. F. The Physics of Mirror Systems. *Phys. Scripta* **T2B**, 336–346 (1982).

[43] I. Katanuma, Y. Tatematsu, K. Ishii, T. Tamano and K. Yatsu. Ideal Ballooning Modes in the GAMMA-10 Tandem Mirror. *J Phys. Soc. Jpn* **69**, 3244–3252 (2000).

[44] William A. Newcomb. Gyroscopic-Quasielastic Fluid Systems. *Ann. Phys.* **81**, 231 (1973).

[45] Berk, H. L. and Kaiser, T. B. Interaction Of The Precessional Wave With Free-Boundary Alfvén Surface Waves In Tandem Mirrors. *Phys. Fluids* **28**(1), 345–351 (1985).

[46] Shiotani, K. and et al, I. K. Calculation of Ballooning Mode Stability Boundary in the GAMMA-10 Tandem Mirror. *Jpn. J. Appl. Phys.* **40**, L776–L778 (2001).

[47] Abramowitz, M. and Stegun, I. A. *Handbook of Mathematical Functions with Formulas, Graphs, and Mathematical Tables.* Dover, New York, ninth dover printing, tenth GPO printing, 1970 edition, (1964).

[48] Post, R. Private Communication Oct 9, (2008).

[49] Rosenbluth, M. and Longmire, C. Stability of Plasmas Confined by Magnetic Fields. *Ann. Phys.* **1**, 120 (1957).

[50] Heidbrink, W. W., Strait, E. J., Chu, M. S., and Turnbull, A. D. Observation of Beta-Induced Alfvén Eigenmodes in the DIII-D Tokamak. *Phys. Rev. Lett.* **71**(6), 855–858 (1993).

[51] Zhang, Y., Heidbrink, W. W., Boehmer, H., McWilliams, R., Chen, G., Breizman, B. N., Vincena, S., Carter, T., Leneman, D., Gekelman, W., Pribyl, P., and Brugman, B. Spectral Gap Of Shear Alfvén Waves In A Periodic Array Of Magnetic Mirrors. *Phys. Plas.* **15**(1) (2008).

[52] Carter, T. Private Communication March 4, (2008).

[53] C.C. Mitchell, J.E. Maggs, S.T. Vincena and W. N. Gekelman. A Laboratory Investigation Of Alfvén Wave Refraction In A Parallel Beta Gradient. *J. Geophy. Res.* **107(A12)**, 1469 (2002).

[54] Vincena, S., Gekelman, W., and Maggs, J. Shear Alfvén Wave Perpendicular Propagation from the Kinetic to the Inertial Regime. *Phys. Rev. Lett.* **93**(10), 105003 (2004).

[55] Berk, H. L., Rosenbluth, M. N., Wong, H. V., and Baldwin, D. E. *Sov. J. Plasma Phys* **9**, 108 (1983).

[56] Berk, H. L. and Lane, B. G. Variational Quadratic Form for Low-Frequency Electromagnetic Perturbations. II. Application to Tandem Mirrors. *Phys. Fluids* **29**(11), 3749–3759 (1986).

[57] Kesner, J. and Lane, B. Effect of Equilibrium Radial Electric Field on Trapped-Particle Stability in Tandem Mirrors. *Phys. Fluids* **28**(2), 634–643 (1985).

[58] Hazeltine, R. D. and Waelbroeck, F. L. *The Framework of Plasma Physics.* Westview Press, (2004).

[59] Scarmozzino, R., Sen, A. K., and Navratil, G. A. Production and Identification of a Collisionless, Curvature-Driven, Trapped-Particle Instability. *Phys. Rev. Lett.* **57**(14), 1729–1732, Oct (1986).

[60] Huba, J. NRL Plasma Formulary, (2006).

Vita

Pratt recieved her Bachelor of Sciences degree in Mathematics from Harvey Mudd College in 2001, with an undergraduate thesis that applied the EDQNM closure to the MHD equations. During this period, she worked as a student with Leaf Turner at the Los Alamos National Laboratory in T-3 and T-15. She then attended the Program for Applied and Computational Mathematics at Princeton University, and recieved a Master of Arts in 2004. While at Princeton Pratt worked with John Krommes on research toward adapting a mapping closure to the Hasegawa-Wakatani equations. Pratt completed her PhD in theoretical plasma physics at the Institute for Fusion Studies at the University of Austin.

Permanent address: 3206 King St #204
Austin, Texas 78705

This dissertation was typeset with LaTeX[†] by the author.

[†] LaTeX is a document preparation system developed by Leslie Lamport as a special version of Donald Knuth's TeX Program.